HAL
open science

Higgs Recoil Mass and Cross-Section Analysis at ILC AND Calibration of the CALICE SiW ECAL Prototype

H. Li

To cite this version:

H. Li. Higgs Recoil Mass and Cross-Section Analysis at ILC AND Calibration of the CALICE SiW ECAL Prototype. High Energy Physics - Experiment [hep-ex]. Université Paris Sud - Paris XI, 2009. English. NNT : . tel-00430432

HAL Id: tel-00430432

https://theses.hal.science/tel-00430432v1

Submitted on 6 Nov 2009

HAL is a multi-disciplinary open access archive for the deposit and dissemination of scientific research documents, whether they are published or not. The documents may come from teaching and research institutions in France or abroad, or from public or private research centers.

L'archive ouverte pluridisciplinaire **HAL**, est destinée au dépôt et à la diffusion de documents scientifiques de niveau recherche, publiés ou non, émanant des établissements d'enseignement et de recherche français ou étrangers, des laboratoires publics ou privés.

Université de Paris-Sud
Centre d'Orsay

LAL 09-118
Octobre 2009

Higgs Recoil Mass and Cross-Section Analysis at ILC
AND
Calibration of the CALICE SiW ECAL Prototype

par

Hengne LI

M.	A.	Djouadi	Rapporteur
Mme	J.	List	
M.	R.	Pöschl	Directeur de la thèse
M.	M.A.	Thomson	Rapporteur
M.	G.	Wormser	Président
M.	D.	Zerwas	

To my wife Xiaoying and my daughter Emma.

Abstract

The major topic of this dissertation is the study of the Higgs recoil mass and the cross section measurements using the Higgs-strahlung process with $Z \rightarrow \mu^+\mu^-$ and e^+e^-, based on the detailed ILD detector simulation. The study assumes a Higgs mass of 120 GeV at center of mass energy 250 GeV with an integrated luminosity of 250 fb^{-1}. The resulting precision achieves 28 MeV on the Higgs mass measurement and 2.0% on the cross section measurement by combining the two Z decay channels. The study proves that the background can be largely reduced and the results exhibit sensitivity to the configuration of the accelerator. The analysis and its results are included in the *ILD Letter of Intent*. The second topic of this dissertation is the MIP calibration of the SiW ECAL prototype developed by the CALICE collaboration. The calibration constants are extracted for the beam test at FNAL in 2008, and they are found to be stable by comparing with that of 2006 CERN.

Key words: ILC
ILD
CALICE
SiW ECAL
MIP Calibration
Higgs
Higgs-strahlung
Higgs Recoil Mass
Cross Section

Résumé

Le sujet principal de cette thèse porte sur les mesures de la masse de recul du boson de Higgs et de sa section efficace en utilisant la réaction de Higgs-strahlung avec $Z \rightarrow \mu^+\mu^-$ et e^+e^-, basées sur la simulation détaillée du détecteur ILD. L'étude a été conduite pour un Higgs de 120 GeV de masse, à une énergie de 250 GeV dans le centre de masse pour une luminosité intégrée de 250 fb^{-1}. La précision obtenue est de 28 MeV sur la mesure de la masse du Higgs et 2.0% sur celle de la section efficace en combinant les canaux de désintégration. Cette étude prouve que le bruit de fond peut être largement réduit et que les résultats sont sensibles á la configuration de l'accélérateur. L'analyse et ses résultats sont inclus dans le *ILD Letter of Intent*. Le second sujet de la thèse est la calibration en MIPs du prototype de ECAL Silicium - Tungstène développé par la collaboration CALICE. Les constantes de calibration sont extraites des données des tests en faisceau effectués au FNAL en 2008 et sont stables par rapport aux données prises au CERN en 2006.

Mots Clés: ILC
ILD
CALICE
SiW ECAL
MIP Calibration
Higgs
Higgs-strahlung
Higgs Recoil Mass
Cross Section

Contents

1 Introduction **1**

2 Physics of Higgs Boson **3**

2.1 The Standard Model 4

2.2 The Higgs Mechanism and Higgs Boson 5

2.3 Constraints on the Higgs Mass 8

2.4 Standard Model Higgs Decay 9

2.5 The Higgs-strahlung Process 10

2.5.1 Production Cross-Section 11

2.5.2 Angular Distribution 12

2.5.3 Kinematics Related 13

2.6 Precision Measurements of the Higgs Mass and the ZH Cross Section . . 14

2.6.1 Significances 14

2.6.2 Strategies 15

3 The International Linear Collider **18**

3.1 Accelerator 19

3.2 International Large Detector concept 23

3.2.1 Tracking Performance 25

3.2.2 Material Budget, Electron Tracking 27

4 CALICE SiW ECAL Prototype **32**

4.1 Design 33

4.2 Data Acquisition 35

4.3 Pedestal and Noise 36

4.4 Performance 37

4.4.1 Linearity and Energy Resolution 37
4.4.2 Spatial and Angular Resolutions 40
4.4.3 Shower Development 42

5 MIP Calibration of the SiW ECAL Prototype 44
5.1 Data Samples 45
5.2 Pedestal Analysis 46
5.3 Muon Selection 47
5.4 Fitting 47
5.5 Corrections for Dead Pads and Fitting Failures 49
5.6 Systematic Errors 51
5.6.1 The Residual Pedestals 51
5.6.2 Different Fitting Ranges 51
5.6.3 Timing Offsets between Different Triggers 52
5.7 Uniformity and Stability 54
5.8 Conclusion 56

6 Higgs Recoil Mass and Higgs-strahlung Cross Section Measurements 57
6.1 Monte Carlo Production 58
6.2 Lepton Identification 60
6.3 Track Selection 62
6.4 Background Rejection 63
6.4.1 Variables for Background Rejection 64
6.4.2 Cut-Based Rejection 79
6.4.3 Likelihood Further Rejection 81
6.5 Fit Methods 83
6.5.1 GPET Function 85
6.5.2 Kernel Estimation 88
6.5.3 Physics Motivated Function 91
6.5.4 Comparison of the Three Methods 94
6.6 Results 94
6.7 Summary and Discussion 96
6.7.1 Accelerator Effects versus Detector Effects on the Results 96
6.7.2 Recovery of the Bremsstrahlung Photons 99

6.7.3 Discussions of the Systematic Error 102

7 Summary and Outlook **106**

A Figures for Likelihood Further Rejection **109**

B Tables of Background Rejection **113**

C The Development Physics Motivated Function for Higgs Recoil Mass Distribution **118**

C.1 Beamstrahlung Photon Distribution for Both Beams 118

C.2 ISR 120

C.3 Gaussian Spread 122

C.4 Projection to Recoil Mass Distribution 122

D Fit Plots **125**

Bibliography **138**

Acknowledgements **141**

List of Figures **142**

List of Tables **148**

Chapter 1

Introduction

In the past decades, experiments at the high energy frontier and their theoretical interpretation have resulted into the Standard Model of particle physics. In the framework of Standard Model, there are two types of particles: fermions and bosons. The fermions are the elementary constituents of matter, while the bosons are the mediators of the interactions between the matter particles.

The Standard Model, however, includes a third component beyond particles and their interactions, the Higgs mechanism that gives mass to the particles, which predicts the existence of a spinless particle, the Higgs boson. The Higgs boson is the only particle of the Standard Model which has not yet been experimentally detected. Therefore, the search and the study of the Higgs boson is one of the main missions of present and future high energy colliders.

Precision measurements of the properties of Higgs are required to give directions for new physics. For example, a precise knowledge of the Higgs mass may tell us at which scale the Standard Model is no longer valid and new physics could emerge. Moreover, beyond the Standard Model, different theoretical scenarios proposed certain modifications of the Higgs couplings with bosons, which can be discriminated by precision measurements of the cross sections of Higgs production.

With the possible discovery of the Higgs boson at the Large Hadron Collider[23] (LHC), the International Linear Collider[22] (ILC), a proposed electron-positron linear collider, will provide the high precision measurements of its properties.

Experimental conditions at the ILC provide an ideal environment for the precision studies of Higgs production due to the unparalleled cleanliness and well-defined initial conditions. The Higgs-strahlung ($e^+e^- \rightarrow Z^* \rightarrow ZH$) process as a major Higgs production mechanism at the ILC, can be used to precisely measure the Higgs mass independent of its decay mode, using the mass recoiling to the Z boson, with $Z \rightarrow \mu^+\mu^-$ or e^+e^-. At the same time, the Higgs-strahlung cross section and therefore the coupling strength at HZZ vertex can be precisely determined.

As the main topic of this dissertation, the strategies for the Higgs recoil mass and the Higgs-strahlung cross section precision measurements are developed. The Higgs-strahlung process is the major benchmark reaction proposed in the *Letter of Intent*

Studies for ILC Detectors[38]. The study is based on the full simulation of the International Large Detector[26] (ILD) concept, which is one of the two detector concepts at ILC that were recently approved by the *International Detector Advisory Group*[25] (IDAG). In this study, the Higgs mass is assumed to be 120 GeV, and the center of mass energy is 250 GeV, with an integrated luminosity of 250 fb^{-1}. The results are included in the *ILD Letter of Intent*[29].

In the current ILD concept baseline design, the choice of the electromagnetic calorimeter (ECAL) is a high granularity sampling calorimeter with tungsten as absorber and silicon as sensitive material (SiW ECAL)[32]. A physics prototype of the SiW ECAL is developed by the CALICE collaboration[30], and tested on beam lines at DESY, CERN and FNAL. The second topic of this dissertation is the calibration of the SiW ECAL prototype for the beam test at FNAL in 2008.

The dissertation is organized as follow. After this introduction, Chapter 2 gives a review the physics of Higgs boson. Chapter 3 briefly introduces the ILC and the ILD, including their baseline designs and performances, which are focused on the issues may related to the topics of this dissertation. The SiW ECAL prototype is introduced in Chapter 4, with a summary of its performance in the beam test in 2006 at DESY and CERN.

The calibration of the SiW ECAL for the FNAL beam test in 2008, is detailed in Chapter 5. There, the procedure of the calibration is explained, the systematic errors are discussed, the stability and uniformity of the resulting calibration constants are checked.

Chapter 6 describes the study of the Higgs recoil mass and the Higgs-strahlung cross section measurements. In this chapter, the variables for the background rejection are studied in depth, followed by two steps of background suppression: the cut-based rejection and the Likelihood further rejection. Thereafter, three fit methods to extract the Higgs mass and the cross section are studied, they are either newly developed or updated from previous contributions. In the end, after presenting the results, a possible improvement on the $ZH \rightarrow eeX$ channel by including the Bremsstrahlung photons is examined, and the potential systematic errors and solutions are discussed. Finally, a summary and outlook is presented as the last chapter.

Chapter 2

Physics of Higgs Boson

In the past half-century, the Standard Model (SM) theory of particle physics was build up. It is a gauge theory that describes the matter and fundamental interactions (except gravity) with the gauge group $\mathrm{SU_C}(3) \times \mathrm{SU_L}(2) \times \mathrm{U_Y}(1)$. This theory is proved by high-precision experimental measurements to provide the correct and effective description of the strong and electroweak interactions.

The *spontaneous electroweak symmetry breaking* (EWSB) mechanism is a cornerstone of the SM. It was proposed to generate the weak vector boson masses in a way that it is minimal and respects the requirements of renormalizability and unitarity. The application of the EWSB in the context of SM is referred as the *Higgs mechanism*. The Higgs mechanism states that, to "give" the masses of weak vector bosons, an SU(2) doublet of complex scalar fields can be introduced. Its neutral component develops a non-zero vacuum expectation value. As a consequence, the electroweak $\mathrm{SU_L}(2) \times \mathrm{U_Y}(1)$ symmetry is spontaneously broken to the electromagnetic $\mathrm{U_Q}(1)$ symmetry. Three of the four degrees of freedom of the doublet scalar field are absorbed by the $W^{\pm}$ and Z weak vector bosons to form their longitudinal polarizations and to acquire masses. The remaining degree of freedom corresponds to a scalar particle, the *Higgs boson*. Similarly, the fermion masses are generated through a Yukawa interaction with the same scalar field. However, the Higgs boson has not been observed and only constraints on its mass have been inferred from high-precision data.

The discovery of Higgs boson is then unanimously considered to be of profound importance. The search and study of Higgs boson is one of the main missions of present and future high energy colliders.

This chapter outlines the physics of Higgs boson, the theoretical background of the precision measurements for the Higgs mass and the Higgs-strahlung ($\mathrm{e^+e^-} \to Z^* \to ZH$) cross section, which are represented in details in Chapter 6. After an overview of the SM, the Higgs mechanism and the consequential Higgs boson are introduced. The significances and strategies of the precision measurements of the Higgs mass and the Higgs-strahlung cross section are discussed, followed by a description of the Higgs-strahlung process, which is a major Higgs production channel at ILC. Unless further indicated, the references of this chapter are a most recent review[1] of Higgs physics and

some popular textbooks[2][3][4]. The experimental values of the physical parameters that used in this chapter are referred to [5].

2.1 The Standard Model

The Standard Model (SM) states that the material world is made up of the elementary matter particles having spin 1/2, the fermions, and explains the fundamental interactions as resulting from matter particles exchanging force mediating particles having spin 1, the bosons. The fermions consist of three generations of leptons and quarks; the bosons consist of photon for electromagnetic interaction, $W^{\pm}$ and Z for weak interactions, and 8 gluons for strong interactions.

Each type of particle in the SM is described in terms of a mathematical field via the quantum field theory. The matter fields, describing the spin-1/2 fermions, are classified as three generations fields of left-handed and right-handed chiral quarks and leptons, $f_{L,R} = \frac{1}{2}(1 \mp \gamma_5)f$. The left-handed fermions are in weak isodoublets ($I_f^{3L} = \pm 1/2$), while the right-handed fermions are in weak isosinglets ($I_f^{3R} = 0$). They can be summarized as:

$$I_f^{3L,3R} = \pm\frac{1}{2}, 0 : \begin{array}{llll} L_1 = \begin{pmatrix} \nu_e \\ e^- \end{pmatrix}_L, & e_{R_1} = e_R^-; & Q_1 = \begin{pmatrix} u \\ d \end{pmatrix}_L, & u_{R_1} = u_R, \quad d_{R_1} = d_R \\ L_2 = \begin{pmatrix} \nu_\mu \\ \mu^- \end{pmatrix}_L, & e_{R_2} = \mu_R^-; & Q_2 = \begin{pmatrix} c \\ s \end{pmatrix}_L, & u_{R_2} = c_R, \quad d_{R_2} = s_R \\ L_3 = \begin{pmatrix} \nu_\tau \\ \tau^- \end{pmatrix}_L, & e_{R_3} = \tau_R^-; & Q_3 = \begin{pmatrix} t \\ b \end{pmatrix}_L, & u_{R_3} = t_R, \quad d_{R_3} = b_R \end{array} \tag{2.1}$$

The interaction fields, describing the spin-1 bosons, are the B_μ, $W_\mu^{1,2,3}$ and $G_\mu^{1,...,8}$. The field B_μ corresponds to the generator Y (hypercharge) of the $\mathrm{U(1)_Y}$ group, and the three fields $W_\mu^{1,2,3}$ correspond to the generators T^a (with $a = 1, 2, 3$) of the $\mathrm{SU(2)_L}$ group. They are in the electroweak interaction sector. The octet of gluon fields $G_\mu^{1,...,8}$ corresponds to the eight generators T^b (with $b = 1, ..., 8$) of the $\mathrm{SU(3)_C}$ group are in the strong interaction sector.

The strengths of the fields are given by

$$\begin{aligned} G_{\mu\nu}^a &= \partial_\mu G_\nu^a - \partial_\nu G_\mu^a + g_s\, f^{abc} G_\mu^b G_\nu^c \ , \\ W_{\mu\nu}^a &= \partial_\mu W_\nu^a - \partial_\nu W_\mu^a + g_2\, \epsilon^{abc} W_\mu^b W_\nu^c \ , \\ B_{\mu\nu} &= \partial_\mu B_\nu - \partial_\nu B_\mu \ , \end{aligned} \tag{2.2}$$

where g_s, g_2 and g_1 are, respectively, the coupling constants of $\mathrm{SU(3)_C}$, $\mathrm{SU(2)_L}$ and $\mathrm{U(1)_Y}$; the ϵ^{abc} of $\mathrm{SU(2)_L}$ and f^{abc} of $\mathrm{SU(3)_C}$ are both refer to the antisymmetric tensor.

The SM Lagrangian without mass terms for fermions and gauge bosons is then given by

$$\mathcal{L}_{\rm SM} = \mathcal{L}_{\rm F} + \mathcal{L}_{\rm B} \ , \tag{2.3}$$

where, the $\mathcal{L}_{\rm B}$ represents the kinetic energies of gauge bosons, gluons, $W^{\pm}$, Z^0 and photon; and the $\mathcal{L}_{\rm F}$ describes the kinetic energies of fermions, leptons and quarks, and their interactions with gauge bosons; they are given by

$$\mathcal{L}_{\rm B} = -\frac{1}{4}G^a_{\mu\nu}G^{\mu\nu}_a - \frac{1}{4}W^a_{\mu\nu}W^{\mu\nu}_a - \frac{1}{4}B_{\mu\nu}B^{\mu\nu} \ , \tag{2.4}$$

$$\begin{aligned}\mathcal{L}_{\rm F} &= \bar{L}_i\, iD_\mu\gamma^\mu\, L_i + \bar{e}_{Ri}\, iD_\mu\gamma^\mu\, e_{R_i} + \bar{Q}_i\, iD_\mu\gamma^\mu\, Q_i \\ &\quad + \bar{u}_{Ri}\, iD_\mu\gamma^\mu\, u_{R_i} + \bar{d}_{Ri}\, iD_\mu\gamma^\mu\, d_{R_i} \ .\end{aligned} \tag{2.5}$$

In the above equations, the D_μ is the covariant derivative, through which the matter fields ψ are minimally coupled to the gauge fields. In case of quarks, the D_μ is given by

$$D_\mu\psi = \left(\partial_\mu - ig_sT_aG^a_\mu - ig_2T_aW^a_\mu - ig_1\frac{Y_q}{2}B_\mu\right)\psi \ . \tag{2.6}$$

This massless Lagrangian is invariant under $\mathrm{SU(3)_C} \times \mathrm{SU(2)_L} \times \mathrm{U(1)_Y}$ gauge transformations for both fermion and gauge fields. It is suitable to describe photon and gluons since they are massless. However, if the mass terms of the fermions and weak bosons are added to account for their non-zero masses, this Lagrangian is no more invariant under the exact unbroken gauge transformations.

The solution is the electroweak spontaneous symmetry breaking or the Higgs mechanism for short.

2.2 The Higgs Mechanism and Higgs Boson

The Higgs mechanism states that, in order to generate the masses for the three gauge bosons $\mathrm{W}^{\pm}$ and Z while keeping the photon massless, one need a scalar field with at least three degrees of freedom. The simplest choice of the scalar field Φ is a complex SU(2) doublet

$$\Phi = \begin{pmatrix} \phi^+ \\ \phi^0 \end{pmatrix} \tag{2.7}$$

The Lagrangian of the scalar field and its potential are

$$\mathcal{L}_S = (D^\mu\Phi)^\dagger(D_\mu\Phi) - V(\Phi) \ , \ V(\Phi) = \mu^2\Phi^\dagger\Phi + \lambda(\Phi^\dagger\Phi)^2 \ . \tag{2.8}$$

In the potential $V(\Phi)$, the self-coupling λ is positive, which makes the potential bounded from below. The minima of the potential are

$$\begin{aligned} if\ \mu^2 > 0: \quad \langle\Phi\rangle_0 &= \begin{pmatrix} 0 \\ 0 \end{pmatrix}, \\ if\ \mu^2 < 0: \quad \langle\Phi\rangle_0 &= \frac{1}{\sqrt{2}} \begin{pmatrix} 0 \\ v \end{pmatrix}, \quad with\ v = \left(-\frac{\mu^2}{\lambda}\right)^{1/2}. \end{aligned} \tag{2.9}$$

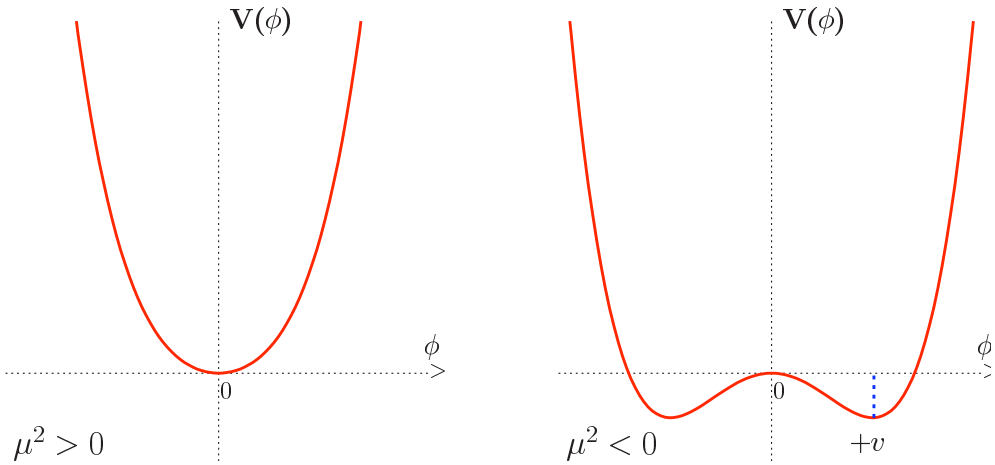

Figure 2.1: The potential V of the scalar field Φ in the cases of $\mu^2 > 0$ (left) and $\mu^2 < 0$ (right)[1].

For $\mu^2 > 0$, the potential has an unique minimum at zero, and the exact symmetry of the Lagrangian is preserved, which is then simply the Lagrangian of a spin-zero particle with mass μ.

For $\mu^2 < 0$, the potential has a non-zero vacuum expectation value v, hence the symmetry $SU(2)_L \times U(1)_Y$ is spontaneously broken to $U(1)_Q$ symmetry. By introducing a field H and perform a U(1) gauge transformation, the field Φ can be parameterized as

$$\Phi = \frac{1}{\sqrt{2}} \begin{pmatrix} 0 \\ v + H \end{pmatrix}. \tag{2.10}$$

With this treatment, the potential minimum at vacuum expectation value $\langle\Phi\rangle_0 = 1/\sqrt{2} \cdot (0, v)^T$ corresponds to the H field at $\langle H\rangle_0 = 0$.

The field H is thus called the *Higgs field*, corresponds to a new scalar boson with spin-0 named *Higgs boson*. The Higgs field represents the quantum fluctuations about the potential minimum, and the perturbative calculations around the potential minimum can be possible.

Expanding of the term $|D_\mu\Phi|^2$ using the Φ parameterized in Equation 2.10 leads to

$$|D_\mu \Phi|^2 = \frac{1}{2}(\partial_\mu H)^2 + \frac{1}{8}g_2^2(v+H)^2|W_\mu^1 + iW_\mu^2|^2 + \frac{1}{8}(v+H)^2|g_2 W_\mu^3 - g_1 B_\mu|^2 \quad (2.11)$$

where the first term in the right hand side describes the Higgs kinetic energy. Then, it is possible to define new fields $W_\mu^\pm$, Z_μ and A_μ orthogonal to Z_μ,

$$W^\pm = \frac{1}{\sqrt{2}}(W_\mu^1 \mp iW_\mu^2) \ , \ Z_\mu = \frac{g_2 W_\mu^3 - g_1 B_\mu}{\sqrt{g_2^2 + g_1^2}} \ , \ A_\mu = \frac{g_2 W_\mu^3 + g_1 B_\mu}{\sqrt{g_2^2 + g_1^2}} \quad (2.12)$$

Thereafter, the mass terms that in quadratic form of fields $W^\pm, Z, A$, can be written as

$$M_W = \frac{1}{2}vg_2 \ , \ M_Z = \frac{1}{2}v\sqrt{g_2^2 + g_1^2} \ , \ M_A = 0. \quad (2.13)$$

Thus, the $W^\pm$ and Z obtain their masses by spontaneously breaking the symmetry $SU(2)_L \times U(1)_Y \rightarrow U(1)_Q$. They are experimentally measured to be

$$M_W = 80.398 \pm 0.025 \text{ GeV} \ , \ M_Z = 91.1876 \pm 0.0021 \text{ GeV} \ . \quad (2.14)$$

Then, Equation 2.11 becomes

$$\begin{aligned} |D_\mu \Phi|^2 &= \frac{1}{2}(\partial_\mu H)^2 \\ &+ M_W^2 W_\mu^+ W^{-\mu} + \frac{1}{2}M_Z^2 Z_\mu Z^\mu \\ &+ 2\frac{M_W^2}{v} H W_\mu^+ W^{-\mu} + \frac{M_Z^2}{v} H Z_\mu Z^\mu \\ &\quad + \frac{M_W^2}{v^2} H^2 W_\mu^+ W^{-\mu} + \frac{1}{2}\frac{M_Z^2}{v^2} H^2 Z_\mu Z^\mu \ , \end{aligned} \quad (2.15)$$

where the last four terms in the right hand side describe the interactions of the gauge bosons $W^\pm$ and Z with the Higgs boson. Their couplings are

$$g_{HVV} = -2i\frac{M_V^2}{v} \qquad g_{HHVV} = -2i\frac{M_V^2}{v^2} \ , \quad (2.16)$$

where V in subscripts refers to either $W^\pm$ or Z.

To study the Higgs boson itself, the potential $V(\Phi)$ has to be expanded using the Φ given in Equation 2.10. The Lagrangian of the potential can be expressed as

$$\mathcal{L}_V = -V(\Phi) = -\lambda v^2 H^2 - \lambda v H^3 - \frac{\lambda}{4}H^4 + const., \quad (2.17)$$

where the first term in the right hand side gives the mass of the Higgs boson

$$M_H^2 = 2\lambda v^2 = -2\mu^2 \ , \tag{2.18}$$

and the second and third terms describe the Higgs self-interactions, with their self-couplings

$$g_{H^3} = (3!)i\lambda v = 3i\frac{M_H^2}{v} \qquad g_{H^4} = (4!)i\frac{\lambda}{4} = 3i\frac{M_H^2}{v^2} \ . \tag{2.19}$$

Similarly, the fermion masses can also be generated using the same scalar field Φ using the Yokava Lagrangian. For instance, in the case of electron, the Lagrangian is

$$\mathcal{L}_e = -\frac{1}{\sqrt{2}}\,\lambda_e\, v\, \bar{e}_L e_R \ - \frac{1}{\sqrt{2}}\,\lambda_e\, H\, \bar{e}_L e_R \ + \cdots \ , \tag{2.20}$$

where the first term in the right hand side is the mass term, with associated electron mass

$$m_e = \frac{\lambda_e v}{\sqrt{2}} \ , \tag{2.21}$$

and the second term describes the interaction between electron and Higgs, with coupling

$$g_{Hee} = i\frac{\lambda_e}{\sqrt{2}} = i\frac{m_e}{v} \ . \tag{2.22}$$

In conclusion, the existence of one isodoublet scalar field is required to generate the masses for the gauge bosons and fermions. As a result, one of the four degrees of freedom of the original isodoublet field is left over, which is corresponding to a physical scalar particle, the Higgs boson.

2.3 Constraints on the Higgs Mass

Today, the SM theory is strongly supported by the experiments, however, the Higgs boson has not been observed. However, there are constraints on this fundamental parameter both experimental and theoretical.

From direct searches of the Higgs boson, the lower limit is $M_H \gtrsim 114$ GeV at 95% confidence level given by LEP2[7]. The recent combined CDF and DØ results[8] excludes the mass range between 160 and 170 GeV at 95% confidence level.

Taking into account all the measurements from electroweak high precision data in a combined fit, one can determine the constraint on the Higgs mass which is summarized in Figure 2.2(left) showing the $\Delta\chi^2$ as a function of $\mathrm{M_H}$.

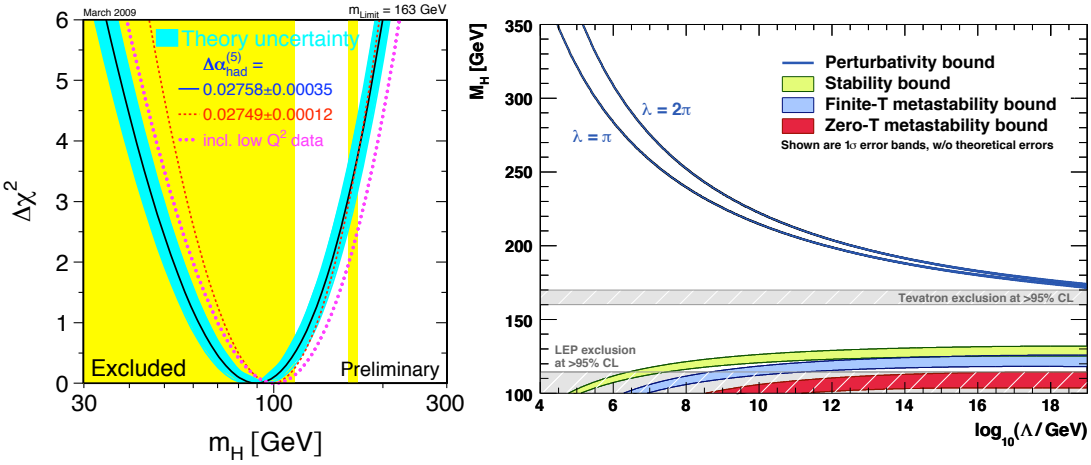

Figure 2.2: Left: The $\Delta\chi^2$ of the fit to the electroweak precision data as a function of M_H, with excluded ranges by direct searches[9]. Right: Theoretical upper and lower bounds on M_H from the assumption that Standard Model is valid up to the cut-off scale Λ[10].

The preferred value for the Higgs mass, corresponding to the minimum of the curve, is at 90 GeV, with an uncertainty of (+36, -27) GeV, which is corresponding to an upper limit of 163 GeV with 95% confident level[9]. This upper limit increases to 191 GeV when including the LEP2 direct search lower limit of 114 GeV[9].

From the theoretical side, constraints can be derived from assumptions on the energy range in which the Standard Model is valid before perturbation theory breaks down and new phenomena may emerge. These constraints include that from the unitarity in scattering amplitudes, the perturbativity of the Higgs self-coupling, the stability of the electroweak vacuum and the fine tuning. Figure 2.2(right) shows the accepted M_H range as a function of the scale Λ. The allowed M_H region is between the upper bands and lower bands; outside this region, either the perturbativity (upper bands) or the stabilities (lower bands) of the SM are not valid. The width of these bands indicates their errors.

2.4 Standard Model Higgs Decay

In the SM, once the Higgs mass is fixed, the Higgs boson branching ratios are completely determined, together with its total decay width. Figure 2.3 shows the branching ratios and total decay width as a function of the Higgs mass.

For Higgs with mass from 114 to 140 GeV, the Higgs dominantly decays to fermion pairs, in particular to $b\bar{b}$ since the couplings of Higgs with fermions are proportional to the fermion masses. The partial width of Standard Model higgs decay into a fermion pair is given by

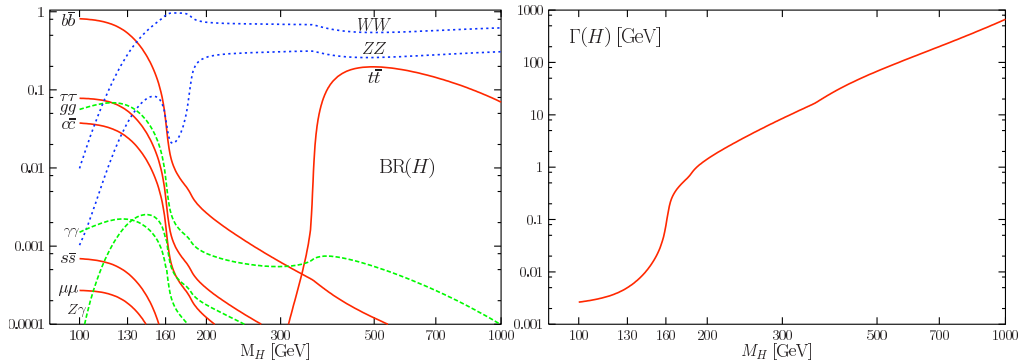

Figure 2.3: The branching ratios (left) and the total decay width (right) of SM Higgs boson as a function of its mass[1].

$$\Gamma(H \to f\bar{f}) = \frac{g_{Hff}^2}{4\pi}\frac{N_C}{2}M_H\left(1 - \frac{4m_f^2}{M_H^2}\right)^{3/2}, \tag{2.23}$$

where $N_C = 1$ for color-singlet leptons, and $N_C = 3$ for color-triplets quarks.

Above 140 GeV, the Higgs decay into WW pair starts to supersede the decay into $b\bar{b}$, and above the ZZ threshold, the Higgs decays dominantly into the WW or ZZ, with their partial widths

$$\Gamma(H \to VV) = \frac{g_{HVV}^2}{4\pi}\frac{2\delta_V}{8M_H}\left(1 - \frac{M_H^2}{3M_V^2} + \frac{M_H^4}{12M_V^4}\right)\left(1 - \frac{4M_V^2}{M_H^2}\right)^{1/2}, \tag{2.24}$$

where V stands for W or Z; $\delta_W = 2$ and $\delta_Z = 1$.

2.5 The Higgs-strahlung Process

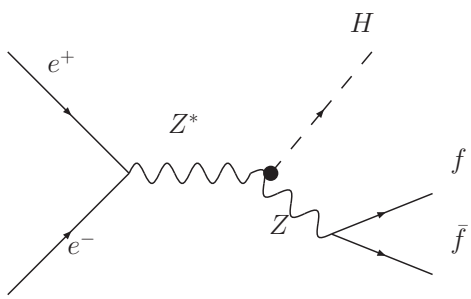

Figure 2.4: Feynman diagram of Higgs-strahlung process.

At future International Linear Collider (ILC), the main production mechanisms of Higgs are the Higgs-strahlung process and the WW fusion mechanism. This dissertation focuses on the Higgs-strahlung process

$$\mathrm{e}^+\mathrm{e}^- \to ZH \to f\bar{f}H \quad , \tag{2.25}$$

which is illustrated in Figure 2.4.

Based on the Higgs-strahlung process, one can precisely measure the Higgs mass and the coupling g_{HZZ} at the HZZ vertex either by direct measurement of the Higgs decay or the recoil of the Z decay.

2.5.1 Production Cross-Section

The integrated cross section of the Higgs-strahlung is given by

$$\sigma(\mathrm{e}^+\mathrm{e}^- \to ZH) = \frac{G_\mu^2 M_Z^4}{96\pi s}(\hat{v}_e^2 + \hat{a}_e^2)\lambda^{1/2}\frac{\lambda + 12M_Z^2/s}{(1 - M_Z^2/s)^2} \ , \tag{2.26}$$

where, $G_\mu = 1.16637(1) \times 10^{-5}$ GeV^{-2} is the fermi coupling constant, $\hat{a}_e = -1$ and $\hat{v}_e = -1 + 4s_W^2$ with $s_W^2 = 0.23149(13)$ being the electroweak mixing angle, and λ is the two-particle phase-space function given by

$$\lambda = (1 - M_H^2/s - M_Z^2/s)^2 - 4M_H^2 M_Z^2/s^2 \ . \tag{2.27}$$

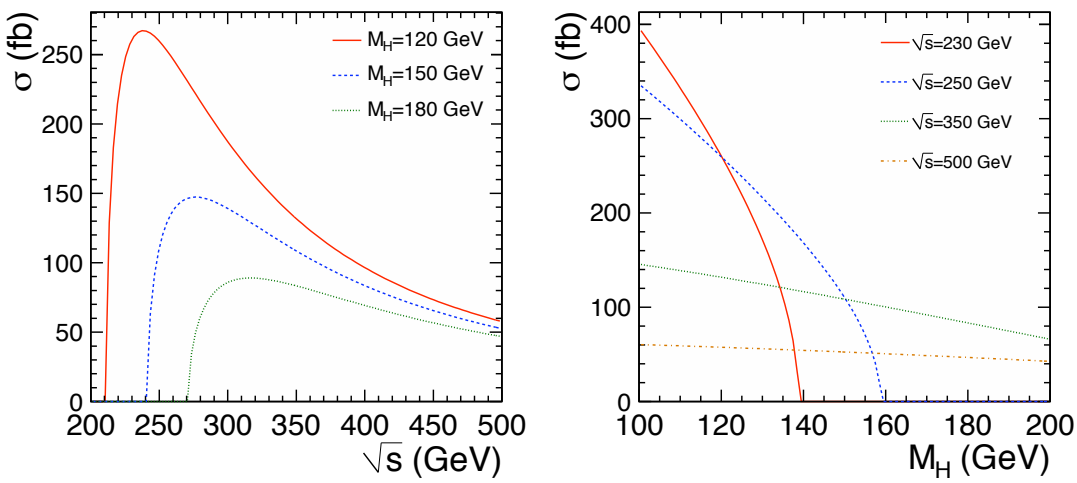

Figure 2.5: Cross-setion (σ) of Higgs-strahlung process, as a function of center of mass energy ($\sqrt{s}$) (left) and as a function of Higgs mass (M_H) (right).

The production cross sections are shown in Figure 2.5. The left figure shows the cross section as a function of center of mass energy ($\sqrt{s}$) for M_H = 120, 150 and 180 GeV. The cross section increases sharply at threshold to a maximum at $\sqrt{s} \sim M_Z + \sqrt{2}M_H$, hereafter, it decreases as $\sim 1/s$. The right figure shows the cross section as a function of Higgs mass (M_H) for center of mass energies $\sqrt{s}$ = 230, 250, 350 and 500 GeV. The cross section decreases as the possible Higgs mass increases, and for moderate Higgs masses, the cross section is larger for smaller center of mass energies. Both the figures show that to gain highest cross section, one should choose the center of mass energy slightly above the mass threshold.

2.5.2 Angular Distribution

The angular distribution of the Z/H bosons in the Higgs-strahlung process is sensitive to the spin of the Higgs particle. For the Standard Model spin-0 Higgs, the explicit form of the angular distribution with θ being the scattering angle is given by

$$\frac{d\sigma(e^+e^- \to ZH)}{dcos\theta} \sim \lambda^2 sin^2\theta + 8M_Z^2/s \ , \tag{2.28}$$

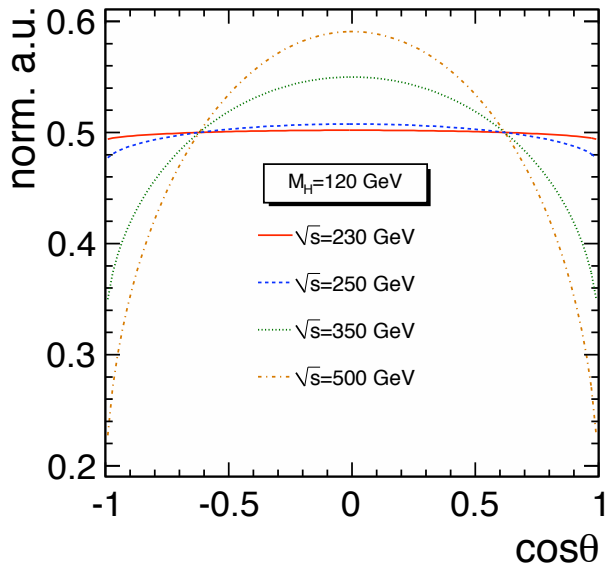

Figure 2.6: Angular distribution of Higgs-strahlung as a function of $cos\theta$ for M_H = 120 GeV.

Figure 2.6 shows the angular distribution of Higgs-strahlung as a function of $cos\theta$ for Higgs mass M_H = 120 GeV with center of mass energies $\sqrt{s}$ = 230, 250, 350 and 500 GeV. The (mostly) central patten of the angular distribution provides opportunities to distinguish the Higgs-strahlung process from major backgrounds experimentally (see Chapter 6).

2.5.3 Kinematics Related

For later on references, some useful kinematics related to the Higgs-strahlung process are given in advance.

The energy and momentum of Higgs and Z in the laboratory frame are given by

$$E_H = \frac{s - M_Z^2 + M_H^2}{2\sqrt{\mathrm{s}}} \ , \tag{2.29}$$

$$E_Z = \frac{s - M_H^2 + M_Z^2}{2\sqrt{\mathrm{s}}} \ , \tag{2.30}$$

$$|\mathbf{P}_H| = |\mathbf{P}_Z| = \frac{\sqrt{[s - (M_H + M_Z)^2] \cdot [s - (M_H - M_Z)^2]}}{2\sqrt{\mathrm{s}}} \ . \tag{2.31}$$

Assuming the center of mass energy $\sqrt{\mathrm{s}} = 250\mathrm{GeV}$, with $\mathrm{M_Z} = 91.2\mathrm{GeV}$ and $\mathrm{M_H} = 120\mathrm{GeV}$, the expectation values of the E_H, E_Z, $|\mathbf{P}_H|$ and $|\mathbf{P}_Z|$ are

$$\begin{aligned} E_H &\simeq 137 \text{ GeV} \ , \\ E_Z &\simeq 113 \text{ GeV} \ , \\ |\mathbf{P}_H| \simeq |\mathbf{P}_Z| &\simeq 66 \text{ GeV} \ . \end{aligned} \tag{2.32}$$

For Z decays to a pair of leptons, i.e., $\mu^+\mu^-$ or $\mathrm{e^+e^-}$, in the high energy limit ($|\mathbf{P}| >> m$), the energy and momentum of Higgs and Z can be expressed by the momenta of the pair of leptons as

$$\begin{aligned} E_Z = \quad E_{dl} &= |\mathbf{P}_1| + |\mathbf{P}_2| \ , \\ \mathbf{P}_Z = \quad \mathbf{P}_{dl} &= \mathbf{P}_1 + \mathbf{P}_2 \ , \end{aligned} \tag{2.33}$$

Hence, the $\mathrm{M_Z}$ and $\mathrm{M_H}$ can be expressed as

$$\begin{aligned} M_Z^2 = \quad M_{dl}^2 &= E_Z^2 - \mathbf{P}_Z^2 \ , \\ M_H^2 = \quad M_{recoil}^2 &= s + M_Z^2 - 2E_Z\sqrt{s} \ , \end{aligned} \tag{2.34}$$

where the E_Z and $\mathbf{P}_Z$ are given by Equation 2.33.

Essentially, the $\mathrm{M_H}$ in Equation 2.34 gives the so-called *Higgs Recoil Mass*, while $\mathrm{M_Z}$ is the *Z Invariant Mass*.

Concerning the pair of leptons decayed from the Z, their possible momentum range can be derived. The momentum minimum ($\mathbf{P}_{1,2}^{min}$) and maximum ($\mathbf{P}_{1,2}^{max}$) of the pair of leptons are thus given by:

$$
\begin{aligned}
|\mathbf{P}_{1,2}^{min}| &= \frac{M_Z}{2} \cdot \sqrt{\frac{E_Z - |\mathbf{P}_Z|}{E_Z + |\mathbf{P}_Z|}} \simeq 23 \text{ GeV}, \\
|\mathbf{P}_{1,2}^{max}| &= \frac{M_Z}{2} \cdot \sqrt{\frac{E_Z + |\mathbf{P}_Z|}{E_Z - |\mathbf{P}_Z|}} \simeq 89 \text{ GeV}.
\end{aligned} \tag{2.35}
$$

2.6 Precision Measurements of the Higgs Mass and the ZH Cross Section

2.6.1 Significances

Previously, it is introduced that the Higgs mass is the only unknown parameter in the SM. The masses of fermions and weak bosons are related to the Higgs mass, and the Higgs couplings to the fermions and weak bosons are determined by the Higgs mass. These are the major significances for the precision measurement of the Higgs mass.

Moreover, precision measurement of the Higgs mass may provide directions for new physics. In Figure 2.2(right), the theoretical constraints on the Higgs mass are given. Therefore, a precision knowledge of the Higgs mass may tell us to what scale the Standard Model is no more valid and new physics could emerge. For instance, if a Higgs with mass of 120 GeV is precisely measured, we may infer that with the scale $\Lambda \gtrsim 10^7$ GeV, the Standard Model is no more valid in stability.

In addition, the work detailed in this dissertation is performed assuming a light Higgs boson with $\mathrm{M_H} = 120$ GeV. In case the Higgs is heavy, the Higgs-strahlung cross section is smaller (Figure 2.5), thus the precision would be worse. This requests the strategies developed must be ultra precise for light Higgs, so as to achieve a reasonable precision even if the Higgs would be heavy.

In the SM, the Higgs-strahlung cross section is determined by the coupling g_{HZZ}. However, beyond the SM, different theoretical scenarios proposed some modifications of the Higgs couplings with gauge bosons, which may be represented by the Higgs-strahlung cross section.

For instance, in the Minimal Supersymmetric extension of the Standard Model (MSSM), radiative corrections to the Higgs-strahlung process may lead to a difference up to 15% on the cross sections[12]. In the constrained Next-to-minimal Supersymmetric extension of the Standard Model (cNMSSM), a possible explanation of the excess of events of a 2.3σ corresponding to a Higgs mass around 98 GeV at LEP[13][7], introduces a reduced coupling of a candidate Higgs boson to the Standard Model gauge bosons, $C_h^V = g_{hZZ}/g_{h^{SM}ZZ} \approx \mathcal{O}(\sqrt{0.1})$[14]. In the Strongly-Interacting Light Higgs (SILH) model, the electroweak symmetry breaking is proposed to be triggered by a light composite Higgs, and the Higgs couplings are modified accordingly[15].

Thus, to discriminate among these theories, a precision measurement of the Higgs-strahlung cross section is desired.

2.6.2 Strategies

The Higgs mass could be measured in both hadron colliders and lepton colliders. However, lepton colliders especially the e^+e^- machine such as the ILC could achieve the most clean signals which the hadron colliders could not achieve.

At ILC, from the Higgs-strahlung process, the Higgs mass could be measured by the direct Higgs decay and the recoiling to the Z. In the later case, especially with $Z \to l^+l^-$, the measure of the Higgs mass can be independent of the Higgs decay model. The Higgs recoil mass is, thus, given by Equation 2.34. Together with Equation 2.33, the only two variables of the Higgs recoil mass are the momenta of the pair of leptons from the Z decay, which can be directly measured from their tracks in the detector.

Moreover, although the branch ratio of the $Z \to l^+l^-$, with l refers to e or μ, is only about 3.4%, which is about 20 times smaller than that of the $Z \to q\bar{q}$, the high precision momentum resolution of lepton tracking could overcome the short in statistics to gain even higher precision on the Higgs mass measurement.

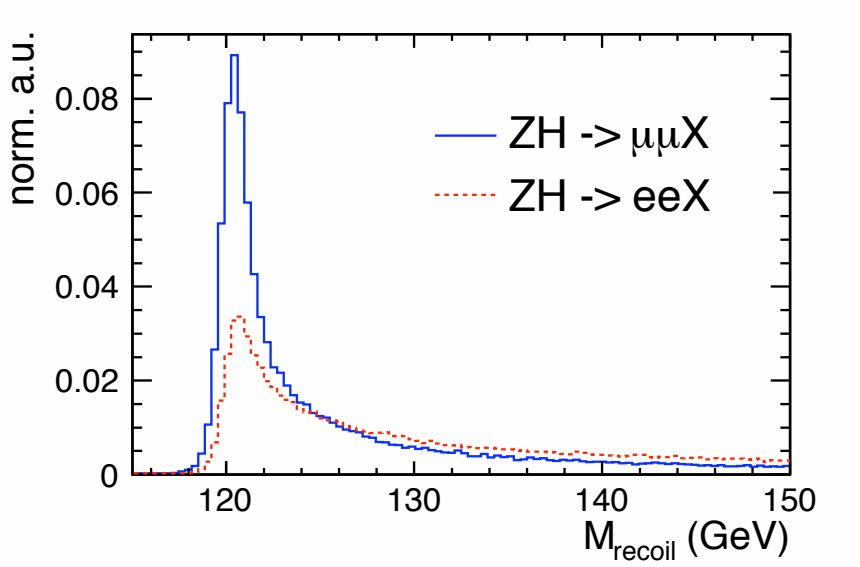

Figure 2.7: Normalized Higgs recoil mass distributions of $M_H = 120$ GeV at $\sqrt{s} = 250$ GeV with $Z \to \mu^+\mu^-$ and e^+e^-.

Due to the reasons stated above, this dissertation employs the recoil mass strategy based on the Higgs-strahlung process with the $Z \to \mu^+\mu^-$ and e^+e^- for the measuring of Higgs mass with high precision. The cross section of the Higgs-strahlung process can be precisely measured at the same time to examine the coupling between Higgs and Z, given by

$$g^2_{HZZ} \propto \sigma = \frac{N_S}{\epsilon\mathcal{L}} \ , \tag{2.36}$$

where N_S is the number of events of Higgs-strahlung signal, ϵ is the total efficiency of signal reconstruction, and $\mathcal{L}$ is the luminosity.

Figure 2.7 gives the typical Higgs recoil mass distributions of $\mathrm{M_H} = 120$ GeV at $\sqrt{\mathrm{s}} = 250$ GeV with $Z \to \mu^+\mu^-$ and $\mathrm{e^+e^-}$. The distribution has a maximum around 120 GeV and a long tail to the higher value. The maximum accounts for the Higgs mass, and the number of events (N_S) entering the distribution gives the cross section through Equation 2.36. To extract these two parameters from the distribution, the fitting methods are applied, which are detailed in Section 6.5.

Besides the statistical error introduced by the un-suppressable background, the precision of the Higgs recoil mass measurement can be affected by both the *smearing effects* and the *radiative effects*. The *smearing effects* consist mainly of the beam energy spread and the uncertainty of the detector response. The decay width is also a smearing effect, however, it is negligible for small Higgs mass, e.g. $\Gamma_H = 3.65$ MeV for $\mathrm{M_H} = 120$ GeV. The *radiative effects* include the Beamstrahlung, Initial State Radiation (ISR), Final State Radiation (FSR) and Bremsstrahlung (in case of $Z \to \mathrm{e^+e^-}$). The Higgs recoil mass distribution, $F_S(x)$, can thus be considered as a convolution of all these effects:

$$\begin{aligned} F_S(x) &= G_{beam-spread}(x) \otimes R_{beamstrahlung}(x) \Big[\otimes B_{decay-width}(x) \Big] \otimes R_{ISR}(x) \\ &\quad \otimes R_{FSR}(x) \Big[\otimes R_{bremsstrahlung}(x) \Big] \otimes G_{detector-response}(x) \ . \end{aligned} \tag{2.37}$$

The smearing effects are responsible for the width of the mass maximum in Figure 2.7. Thus, larger smearing effects result in larger error on the Higgs mass measurement. The beam energy spread is introduced by the accelerator, and the uncertainty of the detector response in the context is mainly the tracking momentum resolution.

The radiative effects are responsible for the tail as visible in Figure 2.7. They migrate effective statistics from the maximum to the tail, hence reduce the accuracy on the Higgs mass measurement. Since the $ZH \to eeX$ channel has one more radiative effect, the Bremsstrahlung, it has lower maximum while larger tail than that of the $\mu\mu X$ channel. The ISR and FSR are physical effects which are not suppressible, however, the Beamstrahlung could be further reduced by improvement of the accelerator technology, and the Bremsstrahlung of electrons could be minimized by reducing the tracking material of the detector.

Furthermore, referred to a recent strategy study[11] for the Higgs mass and cross section measurements, the optimal center of mass energy should be the one just above the ZH mass threshold.

First of all, as shown in Figure 2.5(left), the cross section maximum of the Higgs-strahlung process is just above the threshold, e.g. 230 to 250 GeV for $\mathrm{M_H} = 120$ GeV. A large cross section is required for the precision measurement.

Secondly, the recoil mass method requires precision measurement of the momenta of the pair of leptons from the Z decay. The momenta of the pair of leptons are

reconstructed using their tracks, with the momentum resolution proportional to the square of the momentum, which can be parameterized as

$$\Delta P = aP^2 \oplus bP \ , \tag{2.38}$$

where a and b are the two parameters characterizing the detector tracking performance.

This indicates smaller momenta of the pair of leptons stand for higher precision on their momenta measurement, hence higher precision on the Higgs mass measurement. While the minimum of the momenta of the pair of leptons requires the Z decaying at rest, i.e. the ZH mass threshold.

A balance of these two issues, i.e. gaining high precision in momentum measurement without lost of statistics, gives the optimal center of mass energy should be the one nearer to the mass threshold, where the Z is less boosted.

Results from previous simulation studies[16, 17, 18, 19, 20, 21] on this topic confirmed the strategies discussed in this section. For instance, Higgs recoil mass measurement using $Z \to l^+l^-$ gives better results than that using $Z \to q\bar{q}$, while, with $\mathrm{M_H} = 120$ GeV, results at $\sqrt{\mathrm{s}} = 230$ and 250 GeV are better than that at $\sqrt{\mathrm{s}} = 350$, and 500 GeV .

Chapter 3

The International Linear Collider

The International Linear Collider[22][24] (ILC) is a proposed electron-positron collider, which will complement the Large Hadron Collider[23] (LHC), to give physicists a new cosmic doorway to explore energy regimes beyond the reach of today's accelerators. With LHC discoveries pointing the way, the ILC, a true precision machine, will provide the missing precisions.

Consisting of two linear accelerators that face each other, the ILC will hurl some 10 billion electrons and positrons toward each other at nearly the speed of light. Superconducting accelerator cavities operating at temperatures near absolute zero give the particles more and more energy until they smash in a blazing crossfire at the center of the machine. Stretching approximately 35 kilometers in length, the beams collide 14,000 times every second at extremely high energies. Each spectacular collision creates an array of new particles that could answer some of the most fundamental questions. The current baseline design allows for an upgrade to a 50 km, 1 TeV machine during the second stage of the project.

Experimental conditions at the ILC provide an ideal environment for the precision study of particle production and decay, and offer the unparalleled cleanliness and well-defined initial conditions conducive to recognizing new phenomena. The electron-positron collisions afford full control of the initial state helicity by appropriately selecting electron and positron polarizations, providing an unique and powerful tool for measuring asymmetries, boosting desired signals, and reducing unwanted backgrounds.

Therefore, the detectors at ILC need not contend with extreme data rates or high radiation fields. However, they need to achieve unprecedented precision to reach the performance required by the physics. The physics does pose significant challenges for detector performance, and pushes the limits of jet energy resolution, tracker momentum resolution and vertex impact parameter resolution.

The ILC is designed to host two detectors at the interaction region. One of the two detector concepts that recently approved by the International Detector Advisory Group[25] (IDAG) is the International Large Detector[26] (ILD). At which, the studies performed in this dissertation are based.

This chapter gives an introduction of the ILC accelerator design and the ILD detec-

tor concept. The descriptions and discussions will focus on the issues that may related to the major topic of this dissertation, the Higgs recoil mass analysis. Section 3.1 gives a brief review of the accelerator design for ILC, with the major beam parameters. Section 3.2 represents the ILD detector concept, including its performance studies based on full simulation.

3.1 Accelerator

The ILC is a 200-500 GeV center of mass energy ($\sqrt{s}$) high-luminosity linear electron-positron collider, based on 1.3 GHz superconducting radio-frequency (SCRF) accelerating cavities.

The overall system design[24] has been chosen to realize the physics requirements. Figure 3.1 shows a schematic view of the overall layout of the ILC, indicating the location of the major sub-systems:

- A polarized electron source based on a photocathode DC gun;
- An undulator-based positron source, driven by a 150 GeV main electron beam;
- 5 GeV electron and positron damping rings (DR) with a circumference of 6.7 km, housed in a common tunnel at the center of the ILC complex;
- Beam transport from the damping rings to the main linacs, followed by a two-stage bunch compressor system prior to the injection into the main linac;
- Two 11 km long main linacs, using 1.3 GHz SCRF cavities, operating at an average gradient of 31.5 MV/m, with a pulse length of 1.6 ms;
- A 4.5 km long beam delivery system, which brings the two beams into collision with a 14 mrad crossing angle, at a single interaction point which can be shared by two detectors.

The total footprint is ∼31 km. The electron source, the damping rings, and the positron auxiliary (keep-alive) source are centrally located around the interaction region (IR). The plane of the damping rings is elevated by ∼10 m above that of the BDS to avoid interference.

These global beam parameters to reach a maximum luminosity of $2 \times 10^{34}\mathrm{cm}^{-2}\mathrm{s}^{-1}$ at $\sqrt{s}$ = 500 GeV are summarized in Table 3.1. The table lists a set of nominal parameters and three other sets that define a parameter plane. The collider has been designed to the nominal parameter set which was optimized considering aspects of the whole accelerator system.

As mentioned in Section 2.6.2, the precision measurement of Higgs recoil mass and Higgs-strahlung cross section is sensitive to the two beam effects: Beamstrahlung and beam energy spread. Their influences on the results will be discussed in Chapter 6.

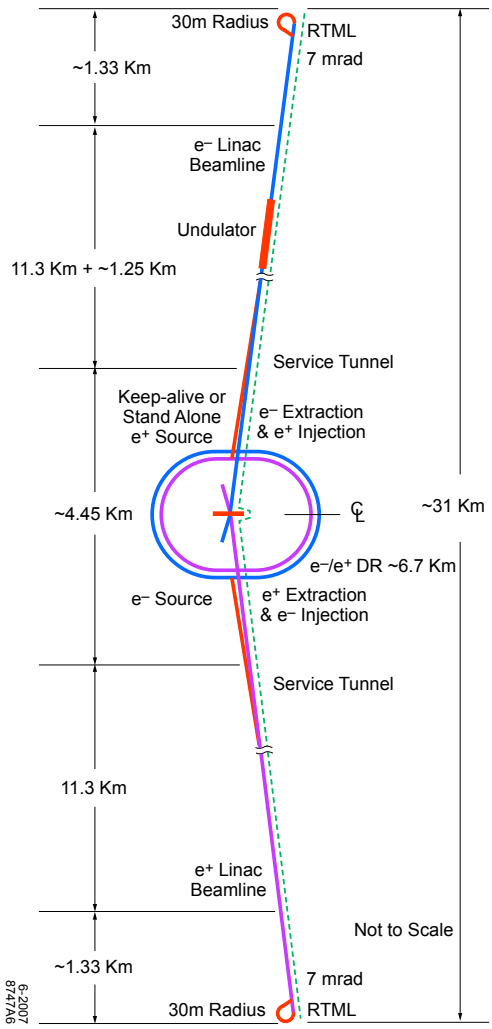

Figure 3.1: Schematic layout of the ILC complex for 500 GeV center of mass energy[24].

Parameter	Value	Units
Center of mass energy $\sqrt{s}$	500	GeV
Peak luminosity	2×10^{34}	$cm^{-2}s^{-1}$
Availability	75	%
Repetition rate	5	Hz
Duty cycle	0.5	%
Main Linacs		
Average accelerating gradient in cavities	31.5	MV/m
Length of each Main Linac	11	km
Beam pulse length	1	ms
Average beam current in pulse	9.0	mA
Damping Rings		
Beam energy	5	GeV
Circumference	6.7	km
Length of Beam Delivery section (2 beams)	4.5	km
Total site length	31	km
Total site power consumption	230	MW
Total installed power	~300	MW

Table 3.1: Global accelerator parameters for 500 GeV center of mass energy[24].

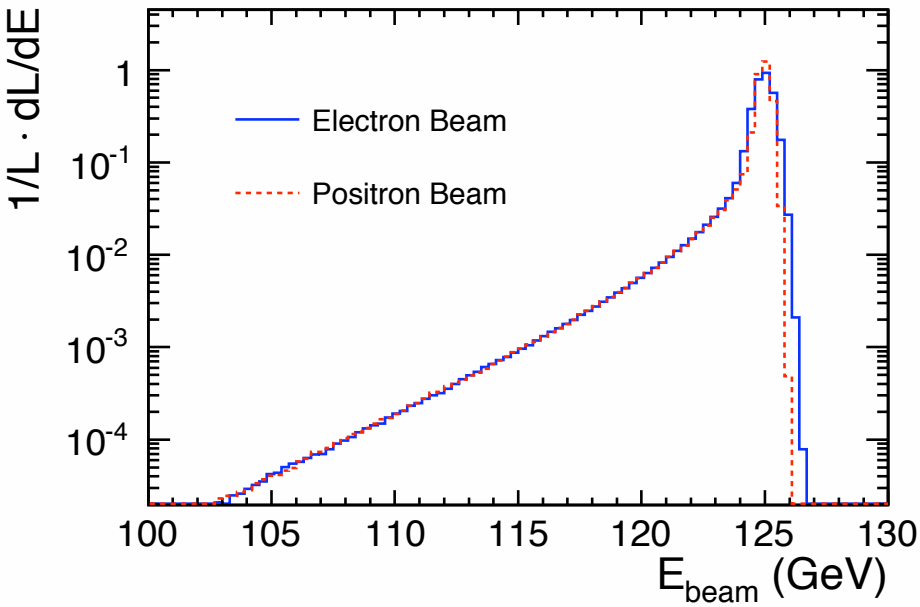

Figure 3.2: Differential beam energy spectra at IP simulated using GUINEA-PIG with IP parameters of Nom.250.

Parameter	Symbol/Units	Calib.90	Nom.200	Nom.250	Nom.350	Nominal	Upgr.1TeV
Center of mass energy	$\sqrt{s}$ (GeV)	90	200	250	350	500	1000
Number of particles per bunch	N (10^{10})	2	2	2	2	2	2
Number of bunches per pulse	n_b	2625	2625	2625	2625	2625	2625
Bunch interval in the Main Linac	t_b	369.2	369.2	369.2	369.2	369.2	369.2
Average beam current in pulse	I_{ave} (mA)	8.7	8.7	8.7	8.7	8.7	8.7
Repetition rate	f_{rep} (Hz)	2.5	5	5	5	5	5
Electron polarization	(%)	N/A	80	80	80	80	80
Positron polarization[1]	(%)	N/A	30	30	30	30	30
Electron energy spread	(%)	0.70	0.35	0.28	0.20	0.14	0.14
Positron energy spread	(%)	0.50	0.25	0.18	0.10	0.07	0.07
Beta function at IP	β_x^* (mm)	75	26	22	20	20	30
Beta function at IP	β_y^* (mm)	2.0	0.6	0.5	0.4	0.4	0.3
R.M.S. beam size at IP	σ_x^* (nm)	3300	1200	950	760	640	550
R.M.S. beam size at IP	σ_y^* (nm)	35	13	10	7.4	5.7	3.3
R.M.S. bunch length	σ_z (μm)	300	300	300	300	300	300
Normalized emittance at IP	$\gamma\epsilon_x^*$ (mm·mrad)	13	10	10	10	10	10
Normalized emittance at IP	$\gamma\epsilon_y^*$ (mm·mrad)	0.054	0.056	0.053	0.047	0.040	0.036
Disruption parameter	D_x	0.03	0.13	0.15	0.17	0.17	0.11
Disruption parameter	D_y	3.3	11.4	14.0	17.5	19.1	18.9
Beamstrahlung parameter	Υ_{ave}	0.002	0.010	0.016	0.027	0.047	0.109
Beamstrahlung parameter	$\kappa = 2/(3\Upsilon_{ave})$	333.3	66.67	41.67	24.69	14.18	6.12
Energy loss by Beamstrahlung	δ_{BS}	0.0002	0.003	0.006	0.012	0.023	0.050
Number of Beamstrahlung photons	n_γ	0.26	0.74	0.89	1.09	1.29	1.43
Luminosity enhancement factor	H_D	1.9	1.8	1.7	1.7	1.7	1.5
Geometric luminosity	$\mathcal{L}_{geo}$ (10^{34}cm^{-2}s^{-1})	0.018	0.28	0.42	0.74	1.1	1.8
Luminosity	$\mathcal{L}$ (10^{34}cm^{-2}s^{-1})	0.033	0.47	0.71	1.2	1.9	2.8

[1] Although the baseline design only requires un-polarized positrons, the positron beam produced by the baseline source has a polarization of ∼30%, and beamline space has been reserved for an eventual upgrade to ∼60% polarization.

Table 3.2: Beam parameters at interaction point (IP)[24].

The Beamstrahlung is a process of energy loss by the incoming electrons deflected by the electromagnetic field of the electron (positron) bunch moving in the opposite direction. The beam energy spread is the energy dispersion of the incoming beams. They are determined by the beam parameters at the interaction point (IP), which is given in Table 3.2.

As mentioned before, the center of mass energy of the Higgs recoil mass measurement processed in this dissertation is 250 GeV, therefore the beam IP parameters of "Nom.250" are chosen. The beam energy distributions for both electron beam and positron beam shown in Figure 3.2 for 250 GeV center of mass energy, is simulated using GUINEA-PIG[37].

3.2 International Large Detector concept

The proposed ILD concept is designed as a multi-purpose detector, which provides excellent precision in spatial and energy measurement over a large solid angle, as required by physics studies. The ILD detector concept is shown graphically in Figure 3.3. It has the following components, with the main parameters summarized in Table 3.3.

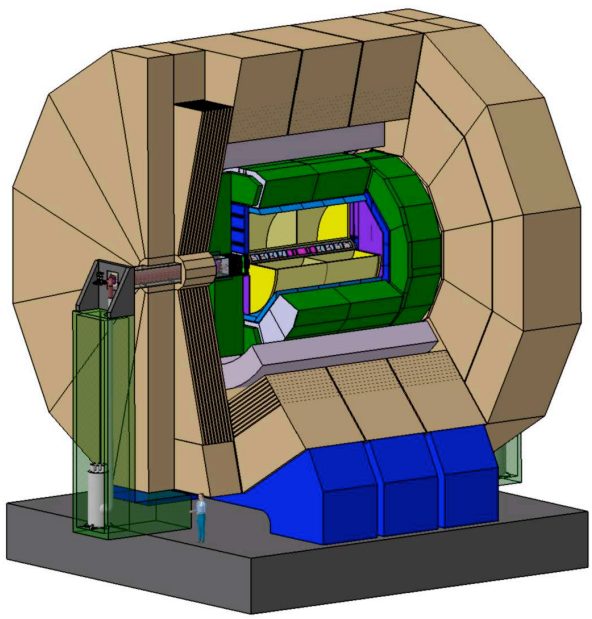

Figure 3.3: View of the ILD detector concept[29].

- A multi-layer pixel-vertex detector (VTX), with three super-layers each comprising two layers. To minimize the occupancy from background hits, the first super-layer is only half as long as the outer two. Whilst the underlying detector technology has not yet been decided, the VTX is optimized for excellent point resolution and minimum material thickness. A five layer geometry, VTX-SL, with

Model Name		ILD
Simulator		Mokka
B field (T)		3.5
Beam-pipe R_{min}		14.5
Vertex Detector	Geometry	ladders
	Layers	3 doublets
	R_{min}	16.0
Barrel SIT	Layers	2 cylinders
	Radii	165, 309
TPC drift region	R_{min}	395
	R_{max}	1739
	z_{max}	2247.5
TPC pad rows		224
ECAL barrel	R_{min}	1847.4
	Layers	20+9
	Total X_0	23.6
ECAL endcap z_{min}		2450
HCAL barrel	Layers	48
	R_{max}	3330
λ_I (ECAL+HCAL)		6.86

Table 3.3: Parameters of the ILD baseline detector concept. Unless otherwise specified, values are shown in units of mm[29].

the layers spaced at equal distances to the IP is investigated as an alternative. In either case the vertex detector has a purely barrel geometry.

- A system of strip and pixel detectors surrounding the VTX detector. In the barrel, two layers of Si strip detectors (SIT) are arranged to bridge the gap between the VTX and the TPC. In the forward region, a system of Si-pixel and Si-strip disks (FTD) provides low angle tracking coverage.

- A large volume time projection chamber (TPC) with up to 224 points per track. The TPC is optimized for excellent 3-dimensional point resolution and minimum material in the field cage and in the end-plate. It also provides dE/dx based particle identification capabilities.

- A system of Si-strip detectors, one behind the end-plate of the TPC (ETD) and one in between the TPC and the ECAL (SET). These provide additional high precision space points which improve the tracking measurements and provide additional redundancy in the regions between the main tracking volume and the calorimeters.

- A highly segmented SiW electromagnetic calorimeter (ECAL) providing up to 30 samples in depth and 5×5 mm transverse cell size. A physics prototype of the SiW ECAL is developed by CALICE calibration[30], see Chapter 4 for details.

- A highly segmented hadronic calorimeter (HCAL) with up to 48 longitudinal samples and small transverse cell size.
- A system of high precision, radiation hard, calorimetric detectors in the very forward region (LumiCAL, BCAL, LHCAL). These extend the calorimetric coverage to almost 4π, measure the luminosity, and monitor the quality of the colliding beams.
- A large volume superconducting coil surrounds the calorimeters, creating an axial B-field of nominally 3.5 Tesla.
- An iron yoke, instrumented with scintillator strips or RPCs, returns the magnetic flux of the solenoid, and at the same time, serves as a muon filter, muon detector and tail catcher.
- A sophisticated data acquisition (DAQ) system which operates without an external trigger.

3.2.1 Tracking Performance

The tracking system envisaged for ILD consists of three subsystems, VTX, FTD and the TPC. They are augmented by three auxiliary tracking systems, the SIT, SET and ETD, which provide additional high resolution measurement points. The study of tracking performance in this section is referred to [29], based on the detector simulation of single muons and $t\bar{t} \rightarrow 6$ jet events.

Figure 3.4(left) shows the average number of reconstructed hits as a function of polar angle (θ), associated with simulated 100 GeV muons. The TPC provides full

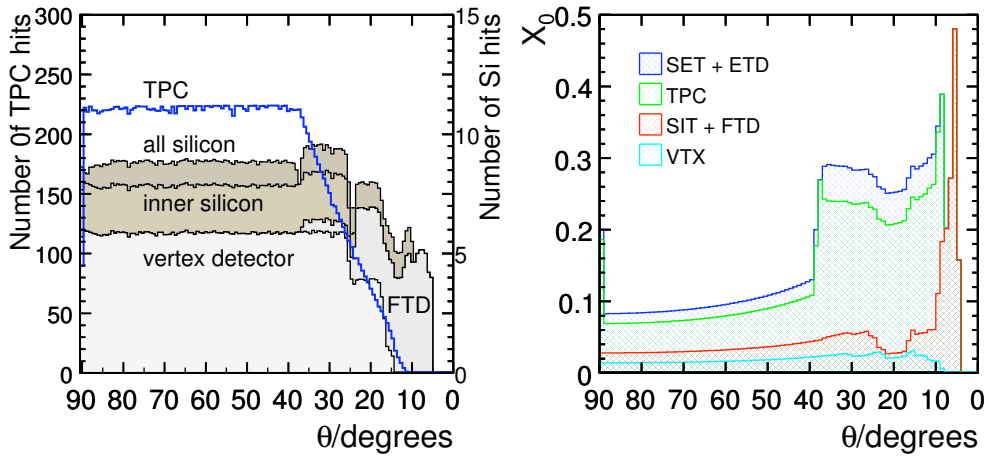

Figure 3.4: Left: Average number of hits for simulated charged particle tracks as a function of polar angle[29]. Right: Average total radiation length of the material in the tracking detectors as a function of polar angle[29].

coverage down to $\theta = 37°$. Beyond this the number of measurement points decreases. The last measurement point provided by the TPC corresponds to $\theta \approx 10°$. The central inner tracking system, consisting of the six layer VTX and the two layer SIT, provides eight precise measurements down to $\theta = 26°$. The innermost and middle double layer of the VTX extend the coverage down to $\theta \sim 16°$. The FTD provides up to a maximum of five measurement points for tracks at small polar angles. The SET and ETD provide a single high precision measurement point with large lever arm outside of the TPC volume down to a $\theta \sim 10°$. The different tracking system contributions to the detector material budget, including support structures, is shown in Figure 3.4(right).

The momentum resolution achieved with the ILD simulation and full reconstructions shown in Figure 3.5(left). The study was performed using muons generated at fixed polar angles of $\theta = 7°, 20°, 30°$ and $85°$, and the momentum was varied over the range $1 - 200\,\mathrm{GeV}$. For two polar angles, this is compared to the expected parametric form of, $\sigma_{1/p_T} = a \oplus b/(p_T \sin\theta)$, with $a = 2 \times 10^{-5}\,\mathrm{GeV}^{-1}$ and $b = 1 \times 10^{-3}$. As can be seen, at a polar angle of 85°, the required momentum resolution is attainable over the full momentum range from 1 GeV upwards, this remains true over the full length of the barrel region of the detector, where the TPC in conjunction with the SET is able to provide the longest possible radial-lever arm for the track fit. For high momentum tracks, the asymptotic value of the momentum resolution is $\sigma_{1/p_T} = 2 \times 10^{-5}\,\mathrm{GeV}^{-1}$. At $\theta = 30°$, the SET no longer contributes, the effective lever-arm of the tracking system is reduced by 25 %. Nevertheless, the momentum resolution is still within the required level of performance. In the very forward region, the momentum resolution is inevitably worse due to the relatively small angle between the B-field and the track momentum.

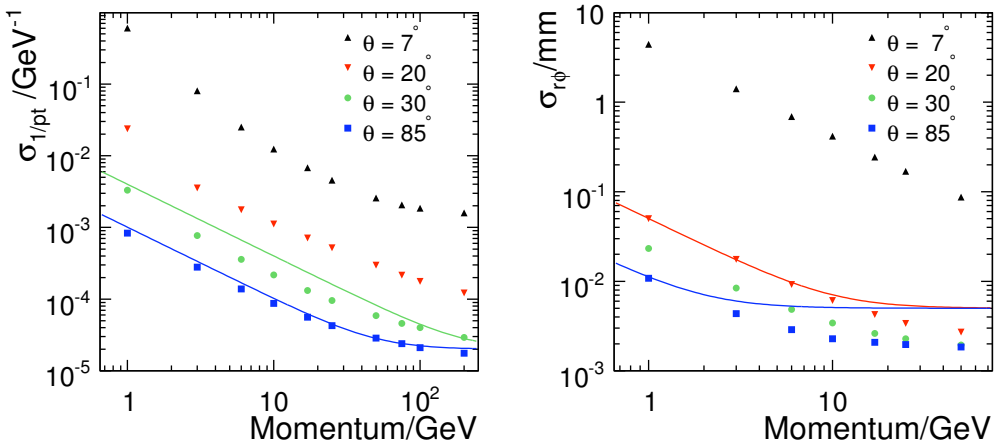

Figure 3.5: Left: Transverse momentum resolution for muons plotted versus polar angle for four different simulated muon momenta. The lines show $\sigma_{1/p_T} = 2 \times 10^{-5} \oplus 1 \times 10^{-3}/(p_T \sin\theta)$ for $\theta = 30°$ (green) and $\theta = 85°$ (blue)[29]. Right: Impact parameter resolution for muons versus polar angle for four different simulated muon momenta[29].

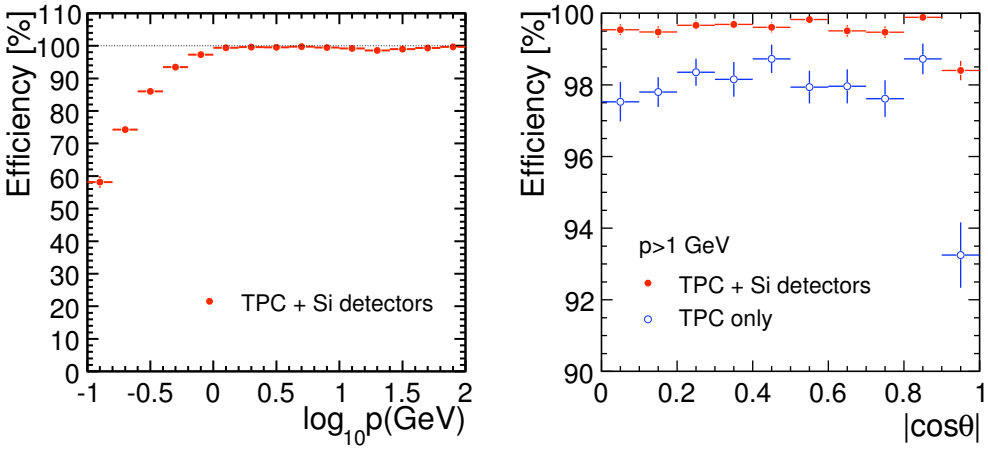

Figure 3.6: Tracking Efficiency as a function for $t\bar{t} \rightarrow 6$ jets at 500GeV plotted against momentum (left) and $\cos\theta$ (right). Efficiencies are plotted with respect to MC tracks which leave at least 4 hits in the tracking detectors including decays and V^0s[29].

Figure 3.5(right) shows $r\phi$ impact parameter resolution as a function of the track momentum. The required performance is achieved down to a track momentum of 1 GeV, whilst it is exceeded for high momentum tracks where the asymptotic resolution is $2\,\mu$m. The rz impact parameter resolution (not shown) is better than $\sim 10\,\mu$m down to momenta of 3 GeV and reaches an asymptotic value of $< 5\,\mu$m for the whole barrel region. Because of the relatively large distance of the innermost FTD disk to the interaction point, the impact parameter resolution degrades for very shallow tracks, $\theta < 10°$. It should be noted that these studies do not account for the possible misalignment of the tracking systems.

With over 200 contiguous readout layers, pattern recognition and track reconstruction in a TPC is relatively straightforward, even in an environment with a large number of background hits. In addition, the standalone tracking capability of the VTX enables the reconstruction of low transverse momentum tracks which do not reach the TPC. Hermetic tracking down to low angles is important at the ILC and the FTD coverage enables tracks to be reconstructed to polar angles below $\theta = 7°$.

Figure 3.6 shows, as a function of momentum and polar angle, the track reconstruction efficiency in simulated (high multiplicity) $t\bar{t} \rightarrow 6$ jet events at $\sqrt{s}$ =500 GeV. For the combined tracking system, the track reconstruction efficiency is approximately 99.5 % for tracks with momenta greater than 1 GeV across almost the entire polar angle range.

3.2.2 Material Budget, Electron Tracking

In the last section, the tracking performance is studied base on single muons. As required by the study of Higgs recoil mass and cross section measurements, which will

be detailed in Chapter 6, a study of the electron tracking and passive material of the ILD detector is performed in this section, using the Higgs-strahlung data sample with $Z \to e^+e^-$.

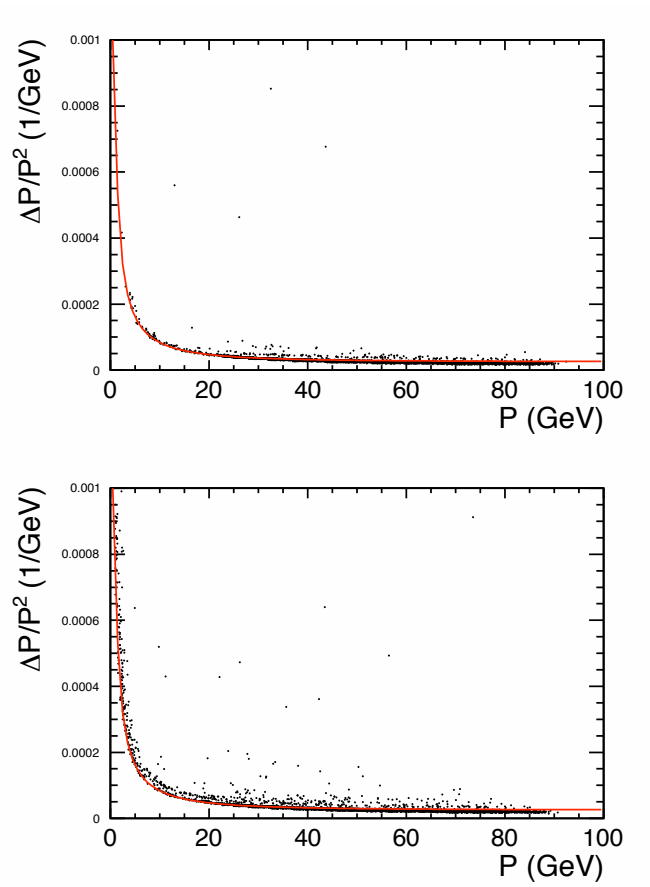

Figure 3.7: $\Delta P/P^2$ as a function of track momentum of muon (top) and electron (bottom) candidates decayed from Z of Higgs-strahlung process, in the barrel region of the ILD.

Figure 3.7 gives the tracking momentum resolutions ($\Delta P/P^2$) of $Z \to \mu^+\mu^-$ (top) and $Z \to e^+e^-$ (bottom) in the barrel region ($|cos\theta| < 0.78$) of the ILD detector. In which, the uncertainty of the momentum (ΔP) is derived from the error matrix of the given track by error propagation. Thereafter, the momentum resolution can be parameterized as:

$$\Delta P/P^2 = a \oplus b/P \ , \tag{3.1}$$

where a and b are the parameters to characterize the tracking performance of a detector. For ILD, as measured from Figure 3.7, they are $a = 2.5 \times 10^{-5}$ GeV^{-1} and $b = 8 \times 10^{-4}$, as drawn in the red curve on the plots.

By comparing the two plots in Figure 3.7, it is clear that the Equation 3.1 with

parameters just given can describe reasonably the *best momentum resolution* for both the electrons and muons. However, the badly measured tracks and low momentum tracks are much more abundant for electrons than for muons. The major reason for the worse tracking performance of electrons is the Bremsstrahlung, which is studied in the following.

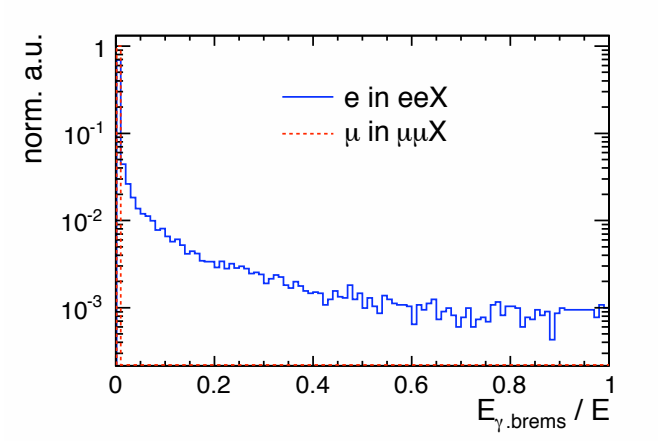

Figure 3.8: Distributions of the fraction of Bremsstrahlung energy loss for electrons and muons before entering TPC, using the Higgs-strahlung samples with $Z \to e^+e^-$ and $Z \to \mu^+\mu^-$, respectively.

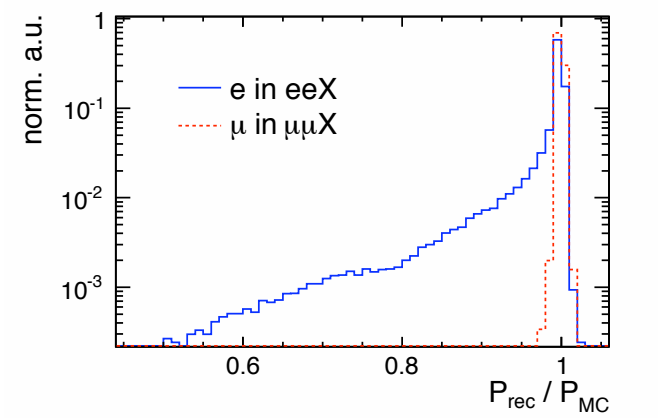

Figure 3.9: Distributions of the ratio between reconstructed momentum and Monte-Carlo truth for electrons and muons, using the Higgs-strahlung samples with $Z \to e^+e^-$ and $Z \to \mu^+\mu^-$, respectively.

Figure 3.8 shows the distributions of the fraction of energy loss due to Bremsstrahlung before entering the TPC, for electrons and muons in the Higgs-strahlung sample with $Z \to e^+e^-$ and $Z \to \mu^+\mu^-$, respectively. From the figure, no energy loss can be observed for muons, however, for electrons, about 15% of them lose more than 10% of their energy due to Bremsstrahlung.

In Figure 3.9, the ratio between the momentum reconstructed and the Monte Carlo truth are compared between the electrons and muons, using the Higgs-strahlung sample with $Z \to e^+e^-$ and $Z \to \mu^+\mu^-$, respectively. According to the figure, momenta of muons can be correctly reconstructed, while that of the electrons are strongly subtracted due to the Bremsstrahlung energy loss.

Both the two figures discussed before show that the Bremsstrahlung seriously affects the electron final states, and the energy loss is proportional to the material budget of the detector. Therefore, the vertex of the Bremsstrahlung photon can be used to sketch the passive material of the ILD detector. Figure 3.10 shows such a sketch, using electrons from the Higgs-strahlung with $Z \to e^+e^-$. The accumulation of the vertices corresponds to the passive material of the detector components as labeled in the figure.

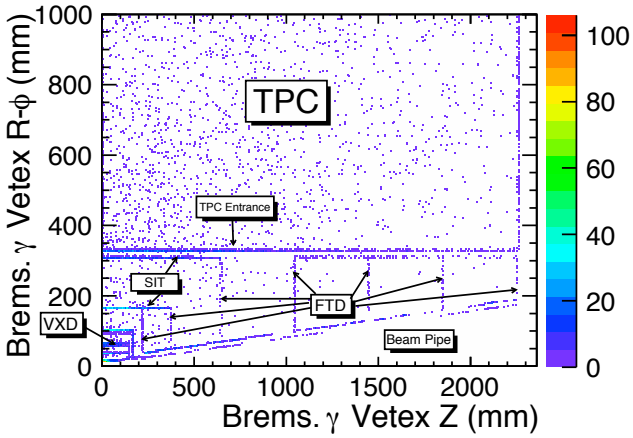

Figure 3.10: Vertices of Bremsstrahlung photons. The accumulation of vertices corresponds to the passive material of detector components as labeled. Figure is drawn using the Higgs-strahlung sample with $Z \to e^+e^-$.

Components	Thickness (X_0)
Beam Pipe	0.2%
VXD (3 double-layers)	0.48%
Beryllium Shell	0.14%
Aluminum Foil	0.6%
SIT (2 layers)	1.3%
TPC inner field-cage	1.3%
Sum	4%

Table 3.4: Transverse passive material budget of the ILD baseline design.

For simplicity, Figure 3.11 gives the material budget in the barrel region before the TPC, sketched by bremsstrahlung photon vertexes. The positions of the photon vertex correspond to the locations of detector components as labeled. While, the amount of the material is propotional to the mean energy loss due to Bremsstrahlung. From this sketch, the transverse material budget that summarized in Table 3.4 can be visualized.

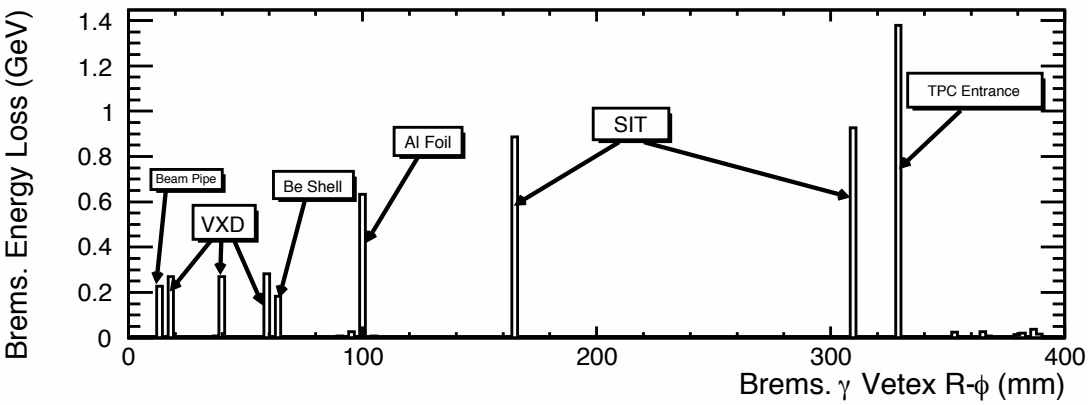

Figure 3.11: Mean Bremsstrahlung energy loss as a function of the Bremsstrahlung photon vertex in the barrel region of the ILD detector, for electrons in the Higgs-strahlung sample with $Z \rightarrow e^+e^-$. The vertices correspond to the positions of the detector components as labeled, with the mean energy loss proportional to the amount of material.

The studies above show that there are totally about 4% X_0 material in front of the TPC, which makes an electron quite often lose a large fraction of its energy due to Bremsstrahlung before entering the TPC. As the main drift chamber with up to 224 points of measurements, the TPC is the most precision detector component in ILD to measure the momentum of a charged track. Therefore, the momentum of an electron that precisely measured by the TPC, may not be the one at the interaction point. Instead, it may be the momentum after Bremsstrahlung energy loss. Thus the Bremsstrahlung effect of electrons introduces additional difficulty when measuring the Higgs recoil mass with $ZH \rightarrow eeX$. The influence on the results will be shown and discussed in Chapter 6.

Chapter 4

CALICE SiW ECAL Prototype

The CALICE (CAlorimeter for LInear Collider Experiment) collaboration[30] consists more than 280 physicists and engineers from around the world, and conducts the R&D for new and high performance calorimeters for the future ILC. The physics requirements of the ILC demand high performance calorimetry, which is best achieved using a finely segmented system that allows to reconstruct events using the Particle Flow Algorithm (PFA)[31].

The calorimeter systems for high energy physics experiments normally consist of three main subsystems: electromagnetic calorimeter (ECAL) to detect electromagnetic showers produced by electrons (or positrons) and photons, hadronic calorimeter (HCAL) to measure hadron-induced showers, and muon tracker (or so-called tail catcher) to identify highly penetrating particles such as muons. CALICE develops the prototypes of these calorimeters which were subjected to beam tests, at DESY during May 2006 with low energy electron beams, at CERN in the summer of 2006 and 2007 with high energy electron and hadron beams, and at FNAL in May and July of 2008 with low energy electron and hadron beams.

The current ILD and SiD[27] baseline choice of the ECAL is a high granularity sampling calorimeter with tungsten as absorber and silicon as sensitive material (SiW ECAL)[32]. As a proof of principle, a physics prototype has been constructed consisting of thirty sensitive layers. Each layer has an active area of 18×18 cm^2 and a pad size of 1×1 cm^2. The absorber thickness is 24 radiation lengths in total.

This chapter introduces the SiW ECAL physics prototype. The design of the prototype is described in Section 4.1, followed by an introduction of its data acquisition system and the pedestal and noise studies in Section 4.2 and 4.3. Its performances are given in Section 4.4, based on the data acquired in 2006 beam tests at DESY and CERN. Unless further cited, the references of this chapter are the two CALICE publications [32] and [33].

4.1 Design

The SiW ECAL prototype is a compact and high granularity sampling calorimeter with tungsten as absorber (or **passive medium**) and silicon as sensitive detector (or **active medium**).

The choice of the absorber material is driven by the need to separate particles in a jet and the need for compactness. The Separation of particles in the transverse and longitudinal directions requires small Molière radius (R_M) and small radiation length (X_0), respectively, so that the electromagnetic showers are compact[1]. The same requirements also result in a compact ECAL. Tungsten, which has a Molière radius of 9 mm and a radiation length of 3.5 mm, fulfills these requirements and is chosen as the absorber material. Moreover, the ratio of interaction length to radiation length is 27.4 so that hadronic showers typically develop later than electromagnetic showers. Better separation of particles also requires high granularity and high resistivity of the active medium. Silicon is the choice, with the pad size of 1×1 cm^2. This size is compatible to the Molière radius of tungsten.

To contain high energy showers, the longitudinal total thickness of the prototype is about 24 X_0 (20 cm), which ensures a containment of 99.5% of the energy for 5 GeV electron showers, and greater than 98% for 50 GeV ones. Totally **30 layers** are chosen to provide sufficient longitudinal granularity. The layers are divided in three independent structures with different absorber thicknesses:

- **Structure 1.4**: 0- 9 layers, 0.4 X_0 (1.4 mm)
- **Structure 2.8**: 10-19 layers: 0.8 X_0 (2.8 mm)
- **Structure 4.2**: 20-29 layers: 1.2 X_0 (4.2 mm)

Figure 4.1(left) gives the schematic view of the SiW prototype, where the three independent structures with different absorber thicknesses can be distinguished.

To keep the calorimeter as compact as possible, and also self-supporting, for every two cconsecutive layers, the tungsten absorber of one of them is incorporated into the **alveolar composite structures** shown in Figure 4.1(left), while that of the other layer is combined into a detector **slab** as a **structure type-H** shown in Figure 4.1(right).

One slab includes two layers of active medium. Each of them is glued to a 14-layer **printed circuit board** (PCB), which is 2.1 mm thick and 600 mm long, and mounted on each side of the structure type-H. The slab is shielded on both sides by an aluminum foil of 0.1 mm thick to protect the silicon modules from electromagnetic noise and provide the wafer substrate ground.

Each silicon layer has an active area of about 18×18 cm^2, divided into 3×3 **modules** (**wafers**); each module is then segmented into 6×6 readout **pads** with size of 1×1 cm^2. Therefore, the active volume of the prototype consists of 9720 pads (**channels**) in total.

[1]For the relevant calorimetry physics, please refer to *Section 27 - Passage of particles through matter* of *Review of Particle Physics*[5].

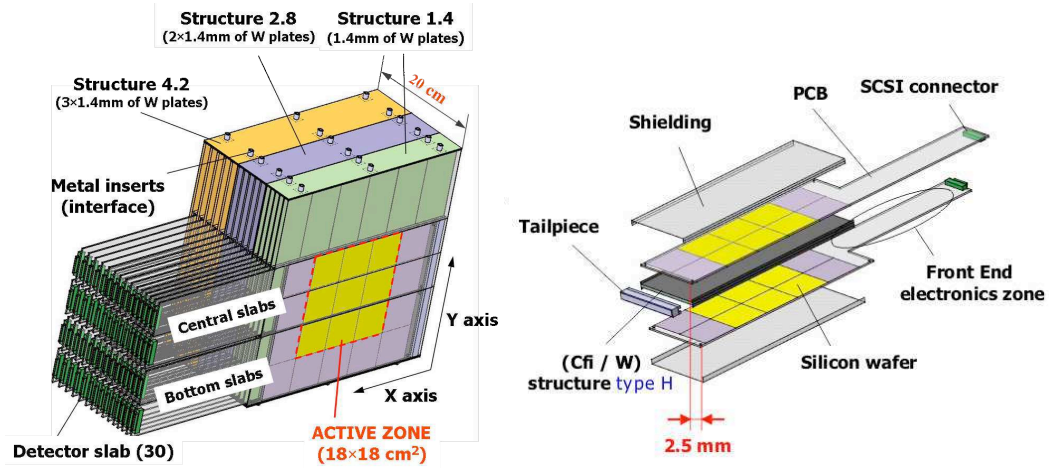

Figure 4.1: Left: Schematic view of the SiW prototype. Right: Schematic diagram showing the components of a detector slab[32].

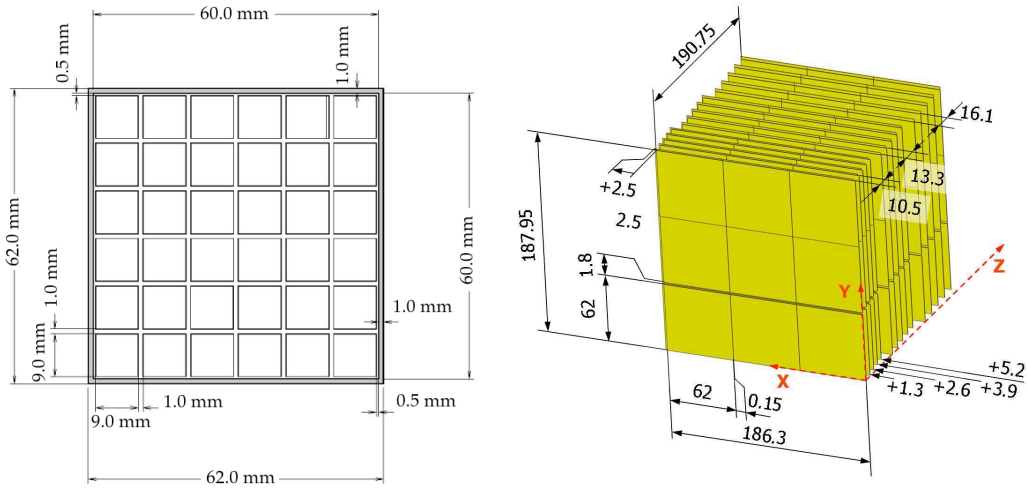

Figure 4.2: Left: Details of the matrix dimensions in a module (wafer). Right: Details of passive area and layer offsets. Offsets are indicated by single-headed arrows. All distances are in mm[32].

The silicon active medium has a thickness of 525 μm. A minimum ionizing particle (MIP) produces about 80 electronhole pairs per μm, hence 42k electrons are obtained for the thickness of 525 μm. The details of the module dimensions are shown in Figure 4.2(left).

The wafers are cut into square modules of 62×62 mm^2, separated from each other by a 0.15 mm wide mounting gap. To reduce overlapping passive areas, the two active medium layers of each slab are offset by 2.5 mm as shown in Figure 4.1(right). Furthermore, the slabs in each substructures are offset by 1.3 mm in the X direction as illustrated in Figure 4.2(right).

Two slabs are inserted per layer, into center and bottom slots of the alveolar composite structures, as shown in Figure 4.1(left). The active area of the center slab consists of 3×2 modules, while that of the bottom slab consists of 3×1 modules.

4.2 Data Acquisition

The very-front-end (VFE) ASICs used to read out the silicon modules have been specifically designed for the prototype and are called FLC_PHY3. The outputs of the VFE ASICs are transmitted to the off-detector electronics using differential analogue lines.

The FLC_PHY3 VFE chip is an 18 channel, charge sensitive, front end circuit. It provides a shaped signal proportional to the input charge. Two chips are necessary to read out one module. Each channel is made of a variable gain charge preamplifier followed by two parallel shaping filters of different gain. Each of these shapers is followed by a sample & hold device driving a single multiplexed output.

For a center slab, the 216 channels are read out by twelve FLC_PHY3 chips. Two 16-bit calibration ASICs, each having six channels, are also mounted on the PCB. Depending on the type of slabs on which they will be mounted, i.e., central and bottom slabs, three variants of the PCBs have been assembled: for the central slabs, fully equipped with an array of 3×2 modules as shown in Figure 4.3; and for the bottom slabs, left or right equipped with a row of 3 modules.

The analogue-to-digital conversion (ADC) is done on off-detector VME boards – "**CALICE Readout Cards**" (CRC), using 16-bit ADCs. Each CRC can read out 96 VFE ASICs, which is corresponding to 1728 channels, hence 6 CRCs are required for the full ECAL readout of 9720 channels. The CRC distributes the sample & hold signal required by the VFE electronics within a latency of 180 ns, with an uncertainty of less than 10 ns, and allows signal timing to 6.25 ns; it provides the digital sequencing necessary to multiplex the analogue signals from the VFE PCBs and analogue-to-digital conversion (ADC). The digitized data are thus stored in memory for subsequent readout by an online readout software system written in C++.

The triggers are controlled using a specific CRC, and are distributed to other CRCs. To ensure that complete events can be built from the same trigger, independent trigger counters are implemented and read periodically. The trigger rising edge provides the system synchronization signal and all timings. All trigger inputs are recorded in a trigger history buffer, which allows the detailed time structure of the trigger logic to be

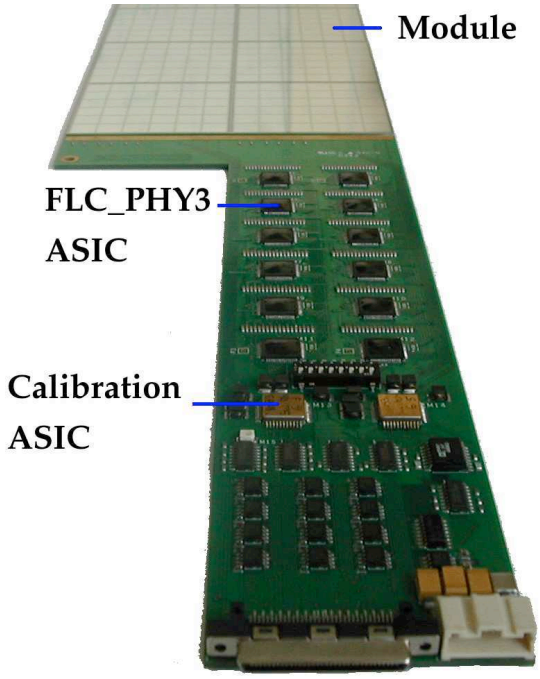

Figure 4.3: Picture of the very from end PCB, and description of its elements[32].

observed as well as readout several other beam line elements such as veto scintillator counters and a Čerenkov detector.

4.3 Pedestal and Noise

For a given channel, the pedestal is defined by the mean value of the readout signal without beam, i.e. coming from electronics, and the noise by the corresponding standard deviation. Subtraction of the pedestal from the readout signal gives the actual signal value.

A data-taking run consists of 500 pedestal events, 500 events with charge injection via the calibration chips, and beam data events between 10,000 to 40,000, after which the sequence repeats. In a first iteration, the pedestals and noises are measured using the 500 pedestal events. The measured pedestals are then subtracted from the later on 30,000 beam data events, which is a procedure carried out channel by channel.

However, instabilities of the pedestals have been observed during the time between two sets of pedestal events. There are two major sources of pedestal shifts observed and studied since the 2006 beam test:

- PCB-wise pedestal shifts
- signal-induced pedestal shifts

The PCB-wise pedestal shifts are due to the non-isolation of the VFE PCB power supply lines, which results in changes to the working point of the output signal lines. The appearance is a (or several) pedestal shift(s) common to all the channels of a PCB within the beam data period between two set of pedestal events, the noise appears to be artificially large and correlated within a PCB.

The correction of the PCB-wise pedestal shifts is on an event-by-event basis, after the first iteration of pedestal subtraction. The pedestal and noise of one event are measured using a sample of channels on a PCB without signal hits. The measured pedestal is thus subtracted from all the channels on the PCB of the event.

The signal-induced pedestal shifts are possibly because of the existence of an intermittent bad contact between the aluminum foil and the module. It appears as the high noise correlations for all the 26 channels on a module.

The correction of the signal-induced pedestal shifts is similar to that of the PCB-wise pedestal shifts on an event-by-event basis, however, the pedestal and noise are estimated per module rather than per PCB.

After pedestal subtraction and all corrections, noise and residual pedestal values are verified to be stable within a run.

4.4 Performance

The performance studies of the SiW ECAL prototype are based on beam test electron data taken at DESY and CERN in 2006. In the beam tests, trigger was defined by the coincidence signal of two of the three scintillator counters, together with that of the Čerenkov detector, which was applied offline for e/π discrimination.

With the electron selection detailed in [33], the performance of the ECAL prototype is presented in this section in terms of energy resolution, linearity of the response, spatial resolution as well as the longitudinal and lateral development of the electromagnetic showers.

4.4.1 Linearity and Energy Resolution

The distribution of reconstructed energy (E_{rec}) for electrons at 30 GeV is shown in Figure 4.4, where the position of the maximum is the mean energy response, named as E_{mean} in the following. Figure 4.5 gives the E_{mean} as a function of the beam energy (E_{beam}).

The beam energy spread ΔE_{beam} is estimated from the dispersion of the E_{mean} in the different runs at the same nominal beam energy:

$$\frac{\Delta E_{\text{beam}}}{E_{\text{beam}}} = \frac{0.12}{E_{\text{beam}}(\text{GeV})} \oplus 0.1\% \tag{4.1}$$

The mean energy response E_{mean} can be parameterized as

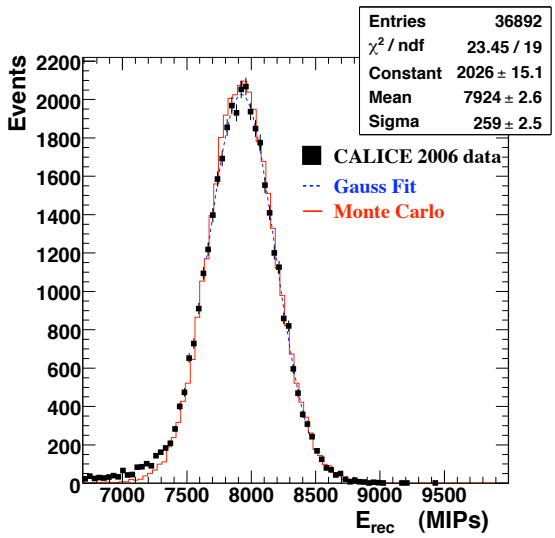

Figure 4.4: Distribution and Gaussian fit of E_{rec} for 20 GeV electrons, together with that of the Monte Carlo simulation. The range of the fit is $[-\sigma, +2\sigma]$[33].

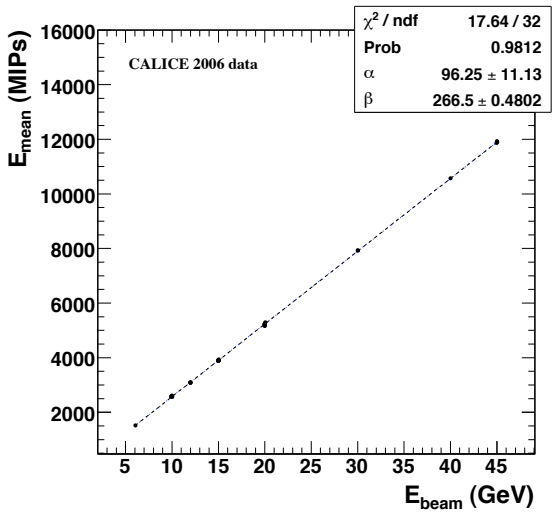

Figure 4.5: Energy responses of the prototype as a function of the beam energy[33].

$$E_{mean}(\text{MIP}) = \beta \cdot E_{beam}(\text{GeV}) - \alpha, \tag{4.2}$$

while the *measured* energy E_{meas} is given by

$$E_{meas}(\text{GeV}) = \frac{E_{mean}(\text{MIP}) + \alpha}{\beta}, \tag{4.3}$$

where parameter β is the global MIP[2] to GeV conversion factor, and the offset α is partly due to the rejection of low energy hits and increases steadily with the hit energy threshold.

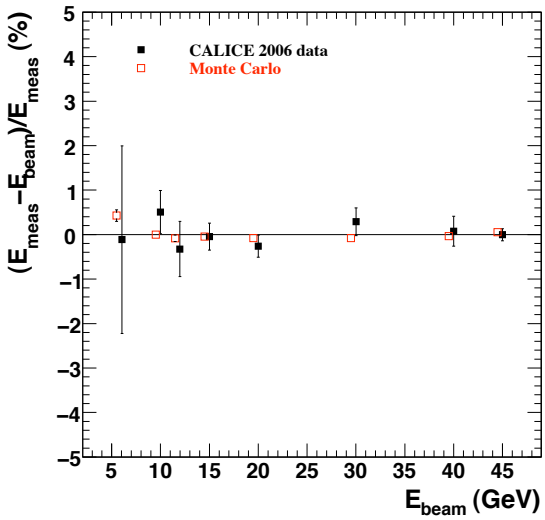

Figure 4.6: The linearity of the response, $(E_{meas} - E_{mean})/E_{meas}$, as a function of the beam energy[33].

The linear fit shown in Figure 4.5 gives the values of MIP to GeV conversion factor β and the offset α as

$$\beta = 266.5 \pm 0.5 \text{ MIP/GeV}; \quad \alpha = 96.25 \pm 11.13 \text{ MIP}. \tag{4.4}$$

Thus, the linearity of the response, $(E_{meas} - E_{mean})/E_{meas}$, is shown in Figure 4.6 as a function of the beam energy. The residuals are approximately within 1% level and consistent with zero non-linearity. Data and simulation agree within one standard deviation.

The relative energy resolution, $\delta(E_{meas})/E_{meas}$, as shown in Figure 4.7, is parameterized by a quadratic sum of stochastic and constant terms

[2]MIP is the energy deposition of the minimal ionizing particles (mip) in the active medium of the ECAL prototype, see Chapter 5 for details.

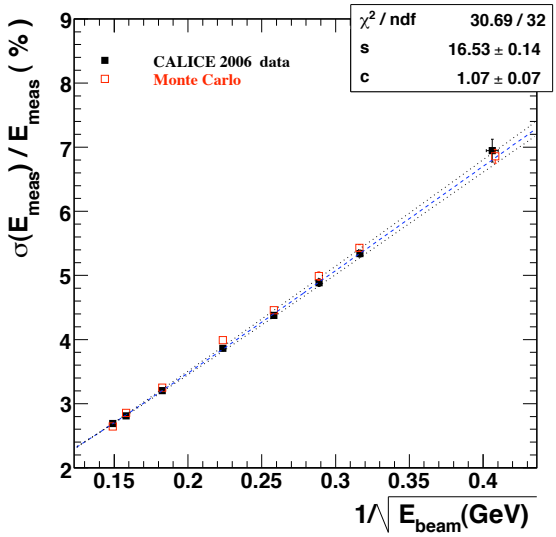

Figure 4.7: Relative energy resolution $\delta(E_{meas})/E_{meas}$ as a function of $1/\sqrt{E_{beam}}$, and the fit with parameterization $s/\sqrt{E} \oplus c$[33].

$$\frac{\sigma(E_{\text{meas}})}{E_{\text{meas}}} = \left(\frac{16.53 \pm 0.14(\text{stat}) \pm 0.4(\text{syst})}{\sqrt{E(\text{GeV})}} \oplus (1.07 \pm 0.07(\text{stat}) \pm 0.1(\text{syst})) \right) \%, \tag{4.5}$$

where the intrinsic energy spread of the beam was subtracted, the contribution of a possible $1/E$ term in the energy resolution is negligible. The dominant systematic uncertainty is due to the rejection of the pre-shower electrons (electrons that start showering before entering the ECAL), which introduces a uncertainty of 0.3% in the stochastic term. A systematic shift in the beam energy of 150 MeV would lead to an additional variation of 0.13% into the stochastic term.

4.4.2 Spatial and Angular Resolutions

The shower direction and position at the front face of the prototype are constructed on an event-by-event basis using a linear two-parameter chi-square fit to the shower barycenter in each layer for the x and y coordinates separately.

The fitted results are compared with the position and angle measured by the tracking system. The expected positions and directions of electrons at the front face are obtained from a fit of hits on the drift chambers as a straight line. Systematic uncertainties are the residual misalignment, the material modeling and the background rate, which are estimated by the extrapolation of the track to the front face of the prototype.

The position and angular resolutions are displayed in Figure 4.8 of DESY beam test data at low energies and in Figure 4.9 of CERN beam test data at high energies.

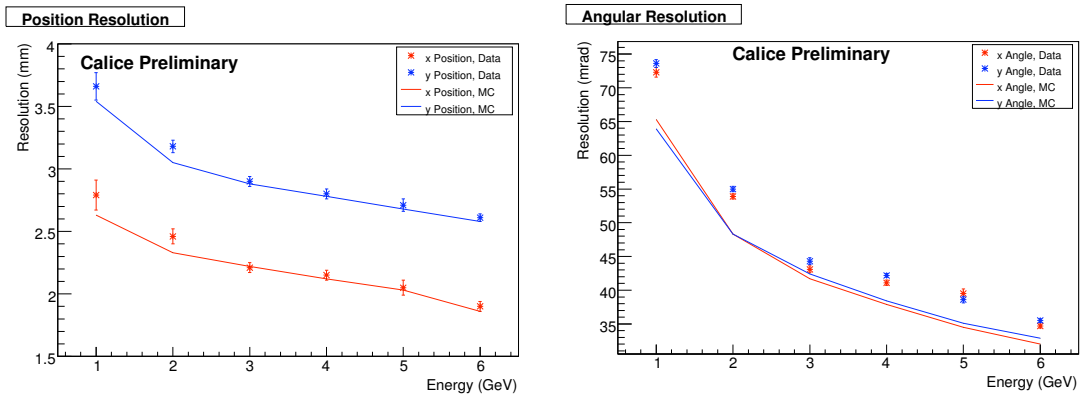

Figure 4.8: Position and angular resolutions as a function of beam energy of DESY beam test data at low energies. The data are shown as points with error bars, while the Monte Carlo simulations are shown by the continuous lines[33].

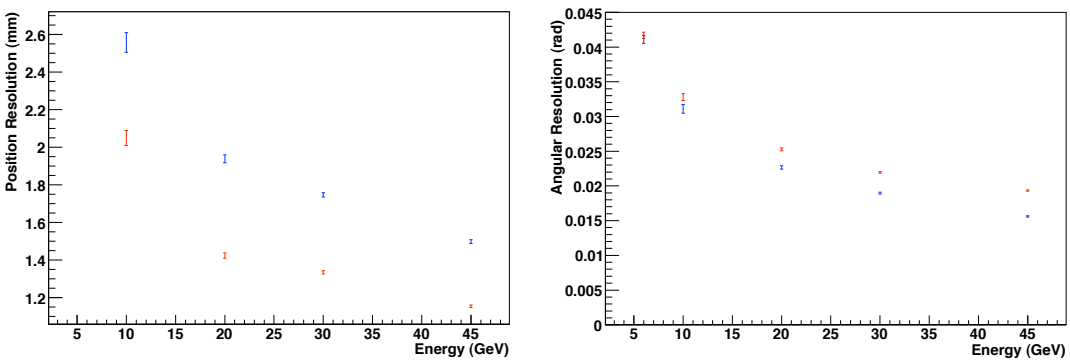

Figure 4.9: Position and angular resolutions as a function of beam energy of CERN beam test data at high energies. The data are shown as points with error bars, with resolution along x axis in blue, and y axis in red[34].

4.4.3 Shower Development

The longitudinal development of the showers is studied using the events outside the inter-wafer gaps. Figure 4.10(left) shows the longitudinal shower profile, with the mean energy distribution fitted by parameterization

$$\gamma(t) = c \cdot t^{\alpha} \cdot e^{-\beta}, \tag{4.6}$$

where t is the calorimeter depth, c is an overall normalization, α and β are constants. The position of the shower maximum grows logarithmically with the beam energy as shown in Figure 4.10(right).

The lateral radii, within which the prototype contains 90% and 95% of the electron energy, are shown in Figure 4.11 as a function of beam energy. The measured radii are 20 mm and 28 mm for 90% and 95% energy containments, respectively.

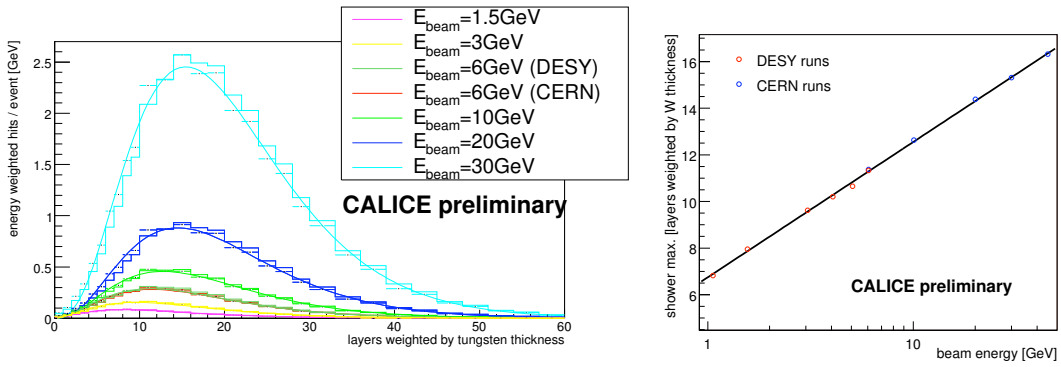

Figure 4.10: Left: Longitudinal shower profile for the data (points) and Monte Carlo simulation (histogram)[33]. Right: Evolution of the shower maximum as a function of the beam energy[33].

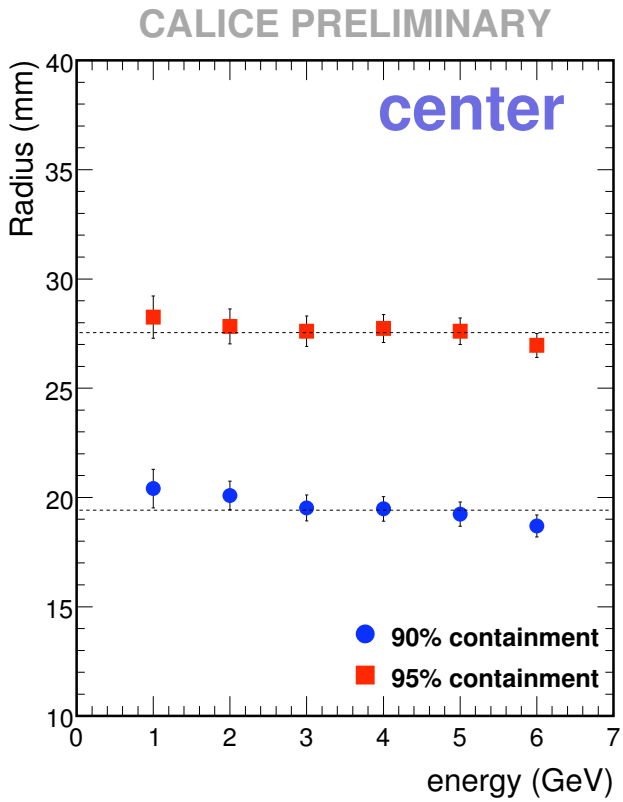

Figure 4.11: Radii for 90% and 95% containment of electrons as a function of the beam energy, with center slabs employed only[33].

Chapter 5

MIP Calibration of the SiW ECAL Prototype

Calibration is the process of establishing the relationship between a measuring device and the units of measure. This is done by comparing the output of a measuring device to a standard, which can be a constant in nature. The calibration of the SiW ECAL physics prototype is to establish the relationship between its electronic signal (in units of ADC) and the energy unit.

The calibration procedure of the SiW ECAL prototype consists of two steps:

The first step a relative calibration, also called MIP calibration. It is is to assign a standard energy scale to the electronic readout from the silicon active medium of each pad. The choice of the standard is the energy loss of muons with momentum from a few hundreds MeV to a few tens GeV when passing through the detector. In this momentum range, muons lose their energy only through ionization, and have the ionization energy loss rates close to the minimum, as shown in Figure 5.1. These muons are said to be minimum ionizing particles, which mostly penetrate the whole detector with (near) identical energy loss rate. Therefore, these muons provide a nature standard of energy for the calibration. The mean energy loss of the muons in the active medium of a pad is defined as an energy unit, MIP. After the first step of calibration, a calibration constant is assigned to each pad, converting its readout signal from the unit of ADC to the energy unit MIP.

The second step is an absolute calibration, the response of the prototype is converted from the unit of MIP to GeV, using electrons that deposit their energies completely into the prototype, where, the energies of the electron beams are known in advance. In this step, the sampling scheme of the ECAL prototype is considered.

This chapter details the procedure of the MIP calibration for the 2008 FNAL beam test data, following the same algorithm developed in [32].

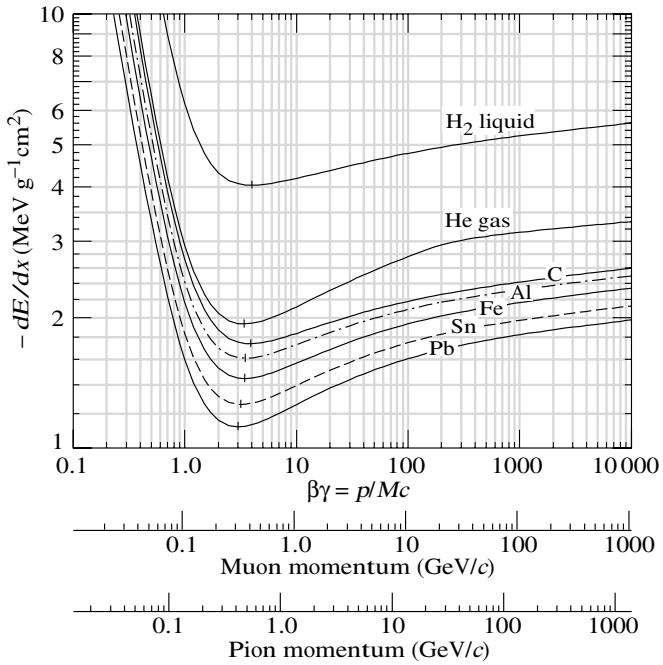

Figure 5.1: Mean energy loss rate as a function of the momenta of muon, pion and proton in liquid (bubble chamber) hydrogen, gaseous helium, carbon, aluminum, iron, tin, and lead[5].

5.1 Data Samples

The muon events that are used in the MIP calibration are recorded during the July beam test period of 2008 with energy of 32 GeV. The number of events that are recorded and successfully reconstructed is more than 520,000. These events are triggered with a 20×20 scintillator counter, which gives a full coverage of the surface of the active area of the prototype. The beam line setup of the 2008 FNAL beam test is given in Figure 5.2.

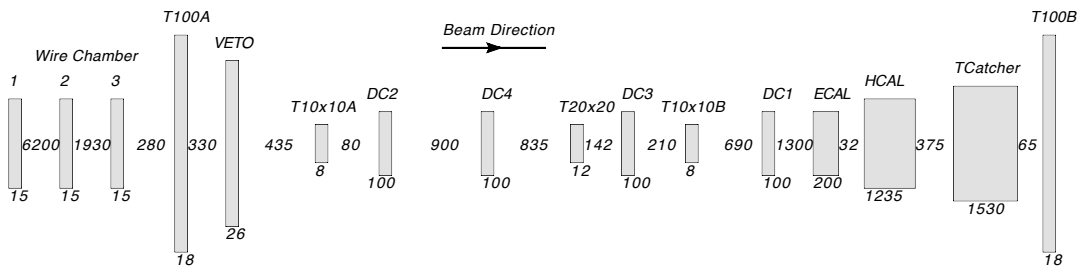

Figure 5.2: Beam line setup of the beam test at FNAL in 2008. The Čerenkov detector in the up stream, which is not drawn in this figure. All distances and dimensions are in mm.

5.2 Pedestal Analysis

In a first step, the pedestals are subtracted for these muon data with the procedure described in Section 4.3. Thereafter, the resulting residual pedestals and noises are checked for each pad. The noise peak is fitted with a Gaussian function for each pad in the range [-10, 5] ADC counts, to avoid being biased by the signal. Thus, the mean of the Gaussian is defined as the residual pedestal and the width is defined as the noise. This noise is later on referred as pedestal noise.

Figure 5.3(left) and 5.4 show the fitted residual pedestal and pedestal noise as a function of pad index for the muon calibration data, which are uniform and stable over pads. The **pad index** is defined as

$$Pad\ ID = 9 \times 36 \times K + 36 \times (3 \times W_x + W_y) + (6 \times P_x + P_y)\ , \tag{5.1}$$

where K is the layer index in the z direction, $W_{x,\ y}$ are the wafer indices in x and y directions, and $P_{x,\ y}$ are the pad indices of a wafer in x and y directions. All the indices are starting from zero, with the coordinates x, y, z defined in Figure 4.1(left) and 4.2(right).

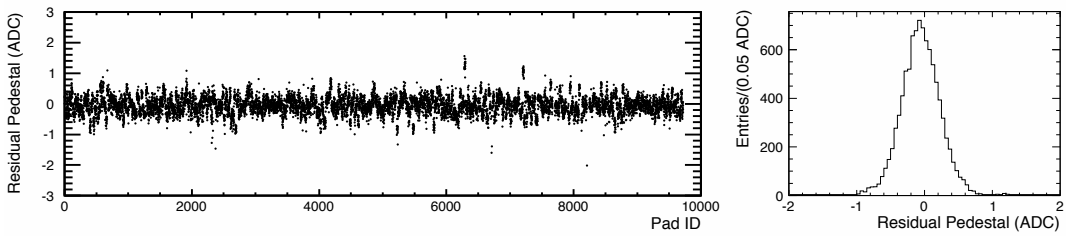

Figure 5.3: Left: Residual pedestal as a function of the pad index (defined in Equation 5.1) for the muon calibration data. Right: Distribution of residual pedestal with each entry representing a pad, with a mean of -0.058 ± 0.003 ADC counts and a RMS of 0.281 ± 0.002 ADC counts.

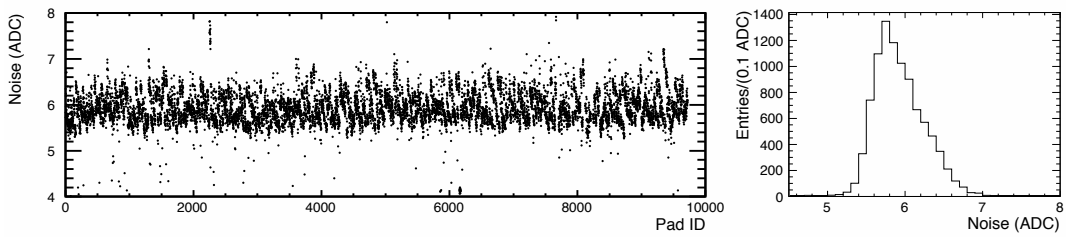

Figure 5.4: Left: Pedestal noise as a function of the pad index (defined in Equation 5.1) for the muon calibration data. Right: Distribution of pedestal noise with each entry representing a pad, with a mean of 5.930 ± 0.003 ADC counts and a RMS of 0.330 ± 0.002 ADC counts.

The resulting average residual pedestal over all channels is -0.058 ± 0.003 ADC

counts for these muon data, with a standard deviation (RMS) of 0.281 ± 0.002 ADC counts, as shown in Figure 5.3(right). While the average pedestal noise is 5.930 ± 0.003 ADC counts, with a RMS of 0.330 ± 0.002 ADC counts, as shown in Figure 5.4(right).

5.3 Muon Selection

The calibration constants are extracted for each pad using the the signal created by the muon hit. Since a minimal ionizing muon passes the ECAL as a straight line leaving a thread of hits in the pads it passed, a muon event is selected by requiring:

- A fit to the hits as a straight line requiring the χ^2/Ndf within 0 to 3;
- The number of hits in the straight line must be greater than 10;
- The distance between two hits in consecutive layers must be less than 2 cm.

The resulting number of hits for each pad from the sample of selected muons is shown in Figure 5.5 as a distribution of all the pads. Within all the 9720 pads, there are 476 dead pads (4.9%) without any hit, while 9016 pads (92.8%) with number of hits more than 500. The pads with small number of hits are most located in the border regions of the active area, due to the non-uniform lateral spread of the muon beams.

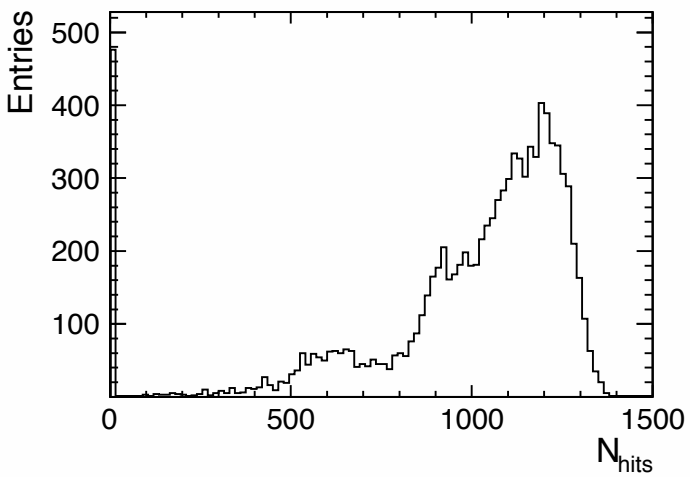

Figure 5.5: Distribution of number of hits for each pad, each entry represents a pad.

5.4 Fitting

For each pad, the calibration constant is determined by fitting the hit energy distribution by a convolution of a Landau distribution with a Gaussian. The Landau distribution describes the energy loss of a charged particle passing through a thin layer

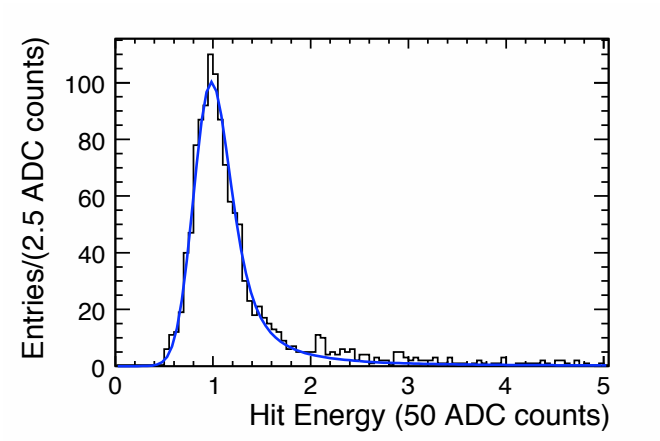

Figure 5.6: A typical fitting of the hit energy distribution of a pad to extract the calibration constant. The fit function is a convolution of Landau with Gaussian. The resulting calibration constant for this particular pad is 46.57 ± 0.04 ADC counts given by the Landau MPV, while the signal induced noise is 7.26 ± 0.73 ADC counts given by the Gaussian sigma.

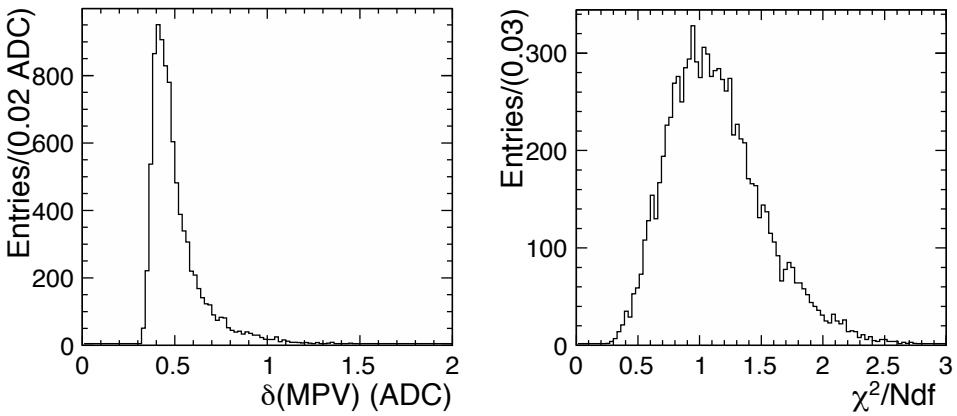

Figure 5.7: Left: Distribution of the statistical error of fitted Landau MPV for each pad, with a mean of 0.516 ± 0.002 ADC counts and a RMS of 0.173 ± 0.001 ADC counts. Right: Distribution of χ^2/Ndf for each pad of the fit to the hit energy spectrum, with a mean of 1.139 ± 0.004, with a RMS of 0.394 ± 0.003.

of matter, where the most probable value (MPV) defines the calibration constant. The Gaussian distribution describes the uncertainty of the detector response, where its sigma is taken as the noise. This noise is later on referred as signal induced noise to be distinct from the pedestal noise mentioned before. The fitting range is set to be between 25 and 78.5 ADC counts. A typical fit of the hit energy distribution of a pad is shown in Figure 5.6.

The distribution of the χ^2/Ndf of the fit to the hit energy distribution for each pad is

shown in Figure 5.7(right) . The average χ^2/Ndf over all the pads is 1.139 ± 0.004, with a RMS of 0.394 ± 0.003. While Figure 5.7(left) shows the distribution of the statistical error ($\delta(MPV)$) of the fitted value of Landau MPV for each pad. On average for all pads, the $\delta(MPV)$ is 0.516 ± 0.002 ADC counts, with a RMS of 0.173 ± 0.001 ADC counts. The statistical error is about two times larger than that of the 2006 CERN beam test, as given in [32]. This is due to the statistics of the muon calibration data are much higher in 2006 CERN beam test.

5.5 Corrections for Dead Pads and Fitting Failures

In the calibration muon runs, 476 pads are found to be dead, which have either zero hit or number of hits less than 100. The map of dead pads is shown in Figure 5.8. From this map, it can be seen that the dead pads appear either at random or as a whole dead chip (a chip reads out half of a wafer, see Section 4.2) due to connection problem.

Beside the dead pads, 47 pads are not converged in the fittings. If any one of the criteria following is not satisfied, the fitting for the pad is said to have failed:

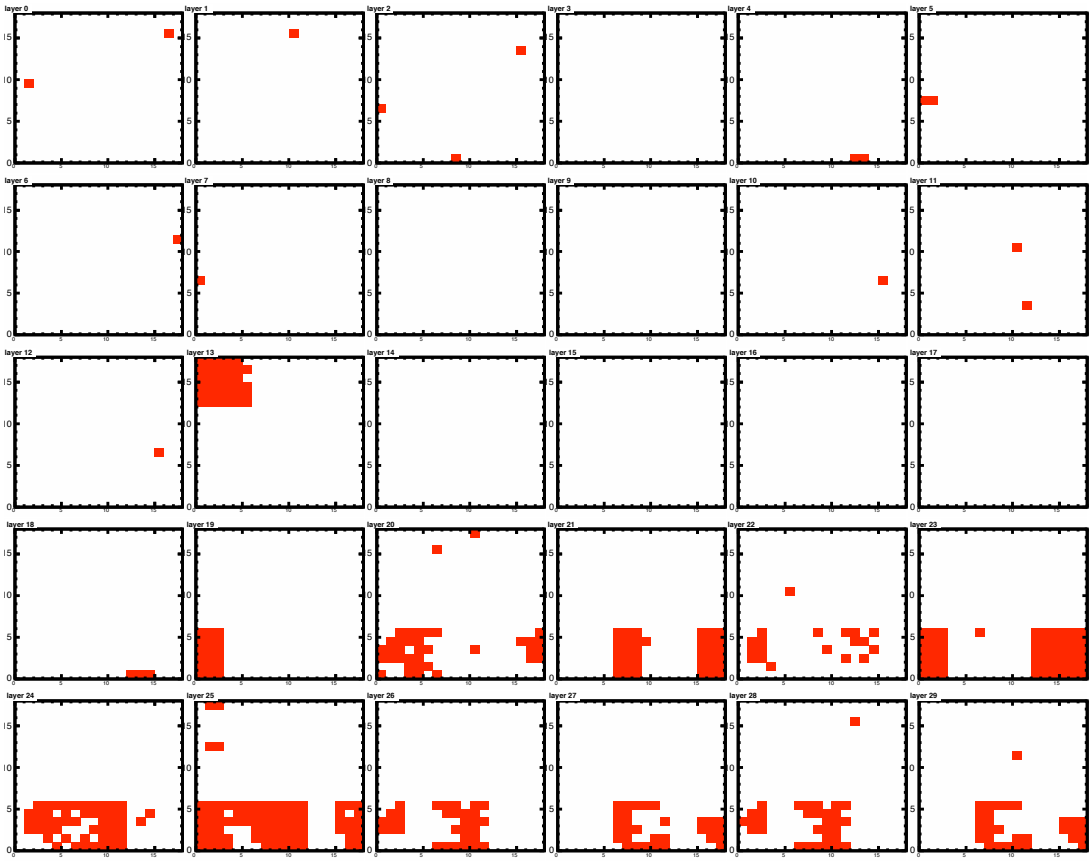

Figure 5.8: Map of the dead pads of all the 30 layers. Layer numbering is starting from left to right and then from top to bottom. Dead pads are marked by color.

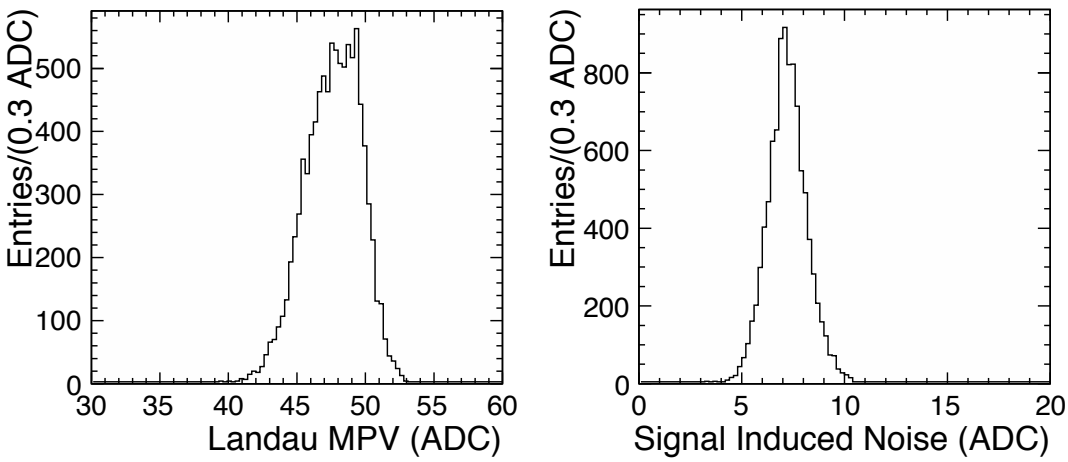

Figure 5.9: Left: Distribution of Landau MPV (calibration constant) with each entry representing a pad, with a mean of 47.61 ± 0.02 ADC counts and a RMS of 2.06 ± 0.01 ADC counts. Right: Distribution of signal induced noise with each entry representing a pad, with a mean of 7.22 ± 0.01 ADC counts and a RMS of 1.00 ± 0.01 ADC counts.

- The measured calibration constant is within (37.5, 53.5) ADC counts;
- The statistical error is less than 2 ADC counts;
- The measured signal induced noise is within (2, 14) ADC counts;
- χ^2/Ndf within (0.5, 3).

The fit failure is due to either short in statistics or an abnormally residual pedestal which has large difference than the average.

The procedure to correct the fitting failures and the dead pads is itemized below:

1. For the fitting failures:
    - They are firstly re-fitted using the same convolution function, together with an additional Gaussian function to account for the abnormal residual pedestals. Out of the 47 fitting failures, 14 are recovered by this re-fitting.
    - The remaining 33 fitting failures are mostly due to short in statistics. They are treated as dead pads.
2. For the dead pads:
    - If a dead pad is found randomly among successful fitted pads, its calibration constant and error is replaced by the average and RMS, respectively, of the successful fitted pads in the same chip. This RMS on average for all the chips is measured to be 1.31 ± 0.03 ADC counts.

- If the dead pads sum up to be a dead chip, the average calibration constant of the successful fitted pads in the same PCB is taken as substitute, with the RMS taken as the error. The average of the RMS for all PCBs is measured to be 1.57 ± 0.03 ADC counts.
- In case that more than half of the pads in a PCB are dead, the average calibration constant of the other PCB in the same slab is taken as substitute. The RMS of the difference between the mean of one PCB and each pad of the other PCB in the same slab, is taken as the error. This RMS is measured to be 1.81 ± 0.01 ADC counts using all the slabs.

After the corrections, the distributions of the calibration constant and the signal induced noise for each pad are shown in the left and right plots of Figure 5.9, respectively. The average of the calibration constants over all pads is 47.61 ± 0.02 ADC counts with a RMS of 2.06 ± 0.01 ADC counts, and the average of the signal induced noise is 7.22 ± 0.01 ADC counts with a RMS of 1.00 ± 0.01 ADC counts.

5.6 Systematic Errors

The sources of systematic errors are coming from:

- The residual pedestals;
- Different fitting ranges in extracting the calibration constants;
- Timing offsets between different triggers.

5.6.1 The Residual Pedestals

In Section 5.2, the uniformity of residual pedestals after pedestal subtraction is studied. There, a resulting average residual pedestal over all pads of -0.058 ± 0.003 ADC counts is obtained from the muon calibration data. This value corresponds to 0.12% of a MIP, is taken as a systematic error due to uncertainty of pedestal subtraction.

5.6.2 Different Fitting Ranges

The fitting range to extract the calibration constants using the convolution of Landau with Gaussian is limited to be between 25 and 78.5 ADC counts. However, if the entire range is fitted, the extracted calibration constants are found to be slightly different. The average difference over all pads of the calibration constants using the two different fitting ranges is 0.258 ± 0.004 ADC counts, with a RMS of 0.366 ± 0.003 ADC counts. The RMS is taken as a systematic error due to different fitting ranges, which is corresponding to 0.77% of a MIP.

5.6.3 Timing Offsets between Different Triggers

The calibration muon runs are triggered with a 20×20 scintillator counter. While the data runs are triggered with either the same 20×20 scintillator counter (20×20 trigger), or two 10×10 scintillator counters together with a Čerenkov detector (10×10&Čerenkov trigger) for the e/π discrimination.

Different trigger setups have different delays in opening the DAQ gate. For instance, the Čerenkov detector is the most slowest one amount the trigger devices just mentioned, since it is putted farther up stream thus has a longer signal propagation time. When the 10×10 scintillator counters are used together with the Čerenkov detector, it has a delay of $62.5ns$ than that of the 20×20 scintillator counter.

On the other hand, certain time after the trigger arrived, the DAQ electronics read out the analogue signal. The time between trigger arrival and signal read out is called the *hold value*. The analogue signal from the detector as a function of time is illustrated in Figure 5.10, which is obtained by the chip scan for the VFE of the ECAL prototype. In the figure, the analogue signal can be parameterized as $f(x) = x \cdot Exp(1-x)$, and the trigger arrival, the signal read out, and the hold value is labeled.

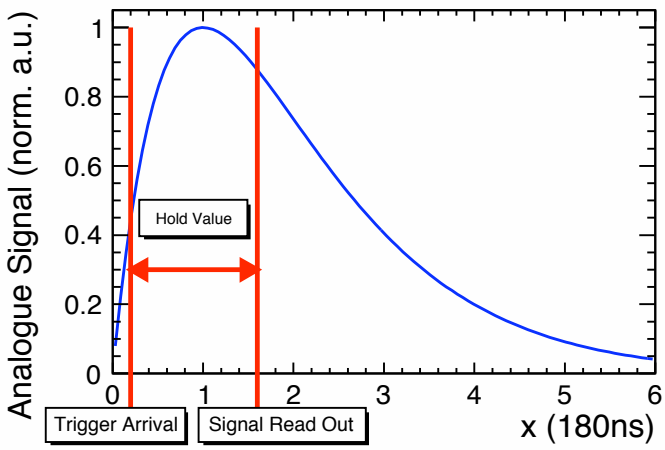

Figure 5.10: Analogue signal curve obtained by the chip scan for the VFE of the ECAL prototype[35]. The hold value, the time of trigger arrival and signal read out are labeled for illustration.

The differences in the time of trigger arrival and in hold values, may introduce a time offset between different trigger setups to read the signal. For example, suppose one trigger setup is holding on the maximum of the signal curve, while the other one is holding much later. Given an identical energy deposition, the response using the first trigger setup will be larger than that of the second one.

Thus, when applying the calibration constants obtained using the muon data with 20×20 trigger, to the data with 10×10&Čerenkov trigger, a systematic error may be introduced.

The method to verify this issue is to take the pion runs with 10×10&Čerenkov

trigger, select the minimal ionizing pions and follow the same calibration as described before. By comparing this set of calibration constants obtained from the minimal ionizing pions with that of the muon one, the differences can be extracted.

Figure 5.11 shows the differences between these two set of calibration constants in a pad-by-pad basis. Due to the 10×10 scintillator only covers the central region of the ECAL active area, the number of pads that can be used for the comparison is 3187. The average of the differences over all available pads is 0.97 ± 0.02 ADC counts, with a RMS of 1.19 ± 0.02 ADC counts.

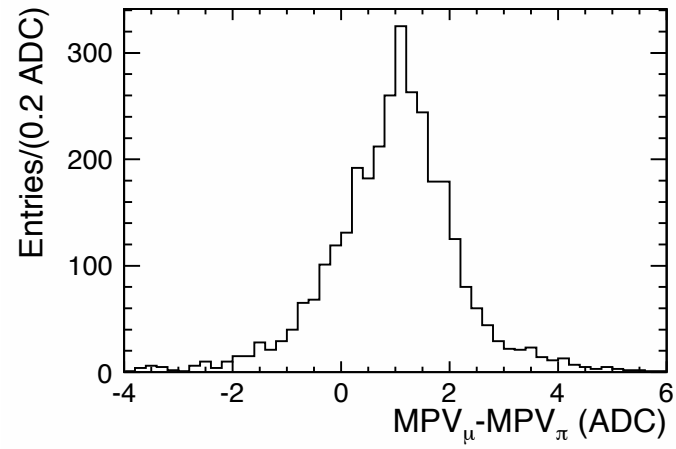

Figure 5.11: Differences of the calibration constants for each pad, between that obtained from muons with 20×20 trigger and from pions with 10×10&Čerenkov, with a mean of 0.97 ± 0.02 ADC counts and a RMS of 1.19 ± 0.02 ADC counts.

Thus, two options are available to account for this systematic error:

- Take the average as the correction factor of the calibration constants and the RMS as the systematic error;
- Take the average itself as the systematic error.

Since the average is smaller than the RMS, the average differences, which corresponding to 0.2% of a MIP, is taken as the systematic error due to the timing offset when apply the calibration constants to the data triggered by 10×10&Čerenkov.

With the beam test conditions at FNAL, it is found that the trigger arrival is always later than the maximum of the analogue signal, even for the fastest trigger, i.e. the 20×20. Therefore, the hold value is set to be zero, in order to read the signal immediately after the trigger arrival. At the same time, most of the electron runs are taken with the same trigger as the muon calibration runs, in order to eliminate the systematic error due to the trigger timing offset. Only low energy pion runs are taken with the 10×10&Čerenkov trigger, for which the e/π discrimination is essential due to the large electron containment in low energy beam.

5.7 Uniformity and Stability

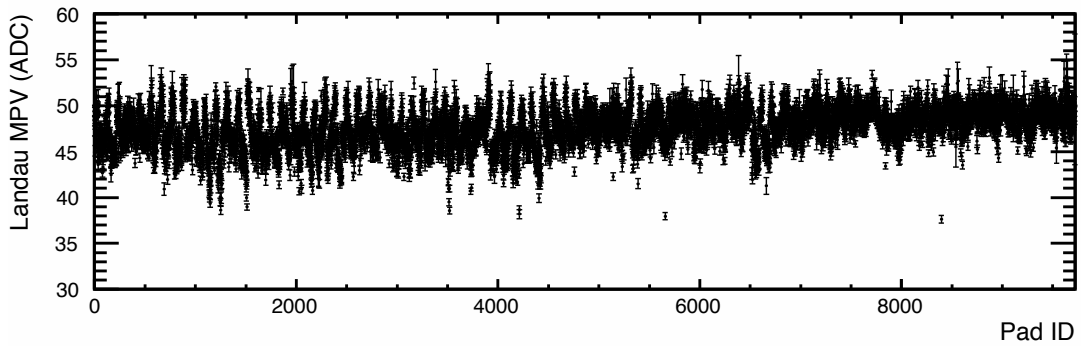

Figure 5.12: Landau MPV (calibration constants) with errors as a function of pad index (defined in Equation 5.1).

Figure 5.12 shows uniformity of the calibration constants of 2008 FNAL across the detector, where the calibration constants for all the pads with errors are given as a function of the pad index.

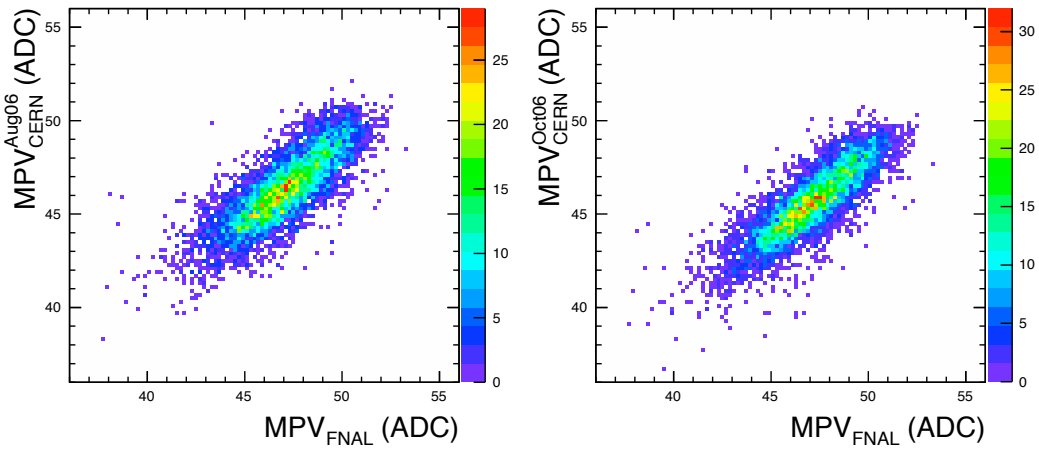

Figure 5.13: Correlation of calibration constants obtained from August (left plot) and October (right plot) 2006 CERN muon runs with those obtained from 2008 FNAL muon runs. A correlation coefficient of 80.30% is found when comparing with August 2006 CERN, while 83.76% is found when comparing with October 2006 CERN.

The calibration constants obtained from 2008 FNAL muon runs are compared with that obtained from the August and October 2006 CERN muon runs, to check the stability in time. In 2006 CERN beam tests, the ECAL prototype was equipped with only the center slabs. Thus, the comparisons are performed only for the 6480 pads in the center slabs, and the pad index in Figure 5.14 and 5.15 is re-defined as

$$Pad\ ID = 6 \times 36 \times K + 36 \times (2 \times W_x + W_y - 1) + (6 \times P_x + P_y)\ , \qquad (5.2)$$

instead of that in Equation 5.1.

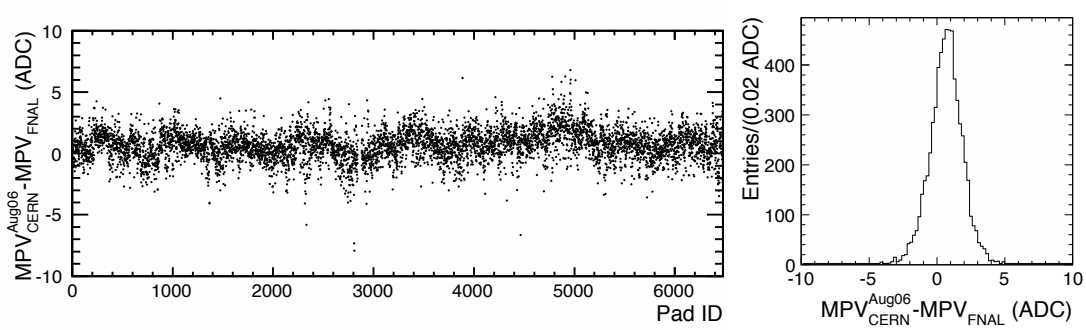

Figure 5.14: Left: Difference of the calibration constants between August 2006 CERN runs and 2008 FNAL runs as a function of pad index (defined in Equation 5.2). Right: Distribution of the difference of each pad, with a mean of 0.67 ± 0.02 ADC counts and a RMS of 1.21 ± 0.01 ADC counts.

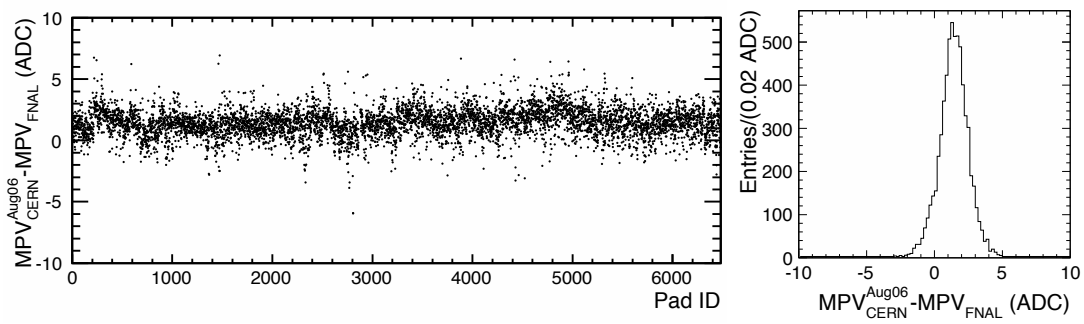

Figure 5.15: Left: Difference of the calibration constants between October 2006 CERN runs and 2008 FNAL runs as a function of pad index (defined in Equation 5.2). Right: Distribution of the difference of each pad, with a mean of 1.42 ± 0.01 ADC counts and a RMS of 1.08 ± 0.01 ADC counts.

In comparing the calibration constants of 2008 FNAL with that of the August 2006 CERN, the correlation is shown in Figure 5.13(left), with a correlation coefficient of 80.30%. The difference between these two sets of calibration constants is checked on a pad-by-pad basis, and shown in Figure 5.14(left) as a function of pad index. The mean value of the differences for all channels is found to be 0.67 ± 0.02 ADC counts with a RMS of 1.21 ± 0.01 ADC counts, as shown in Figure 5.14.

In comparing the calibration constants of 2008 FNAL with that of the October 2006 CERN, the correlation is shown in Figure 5.13(right), with a correlation coefficient of 83.76%. The difference between these two sets of calibration constants is checked on a pad-by-pad basis, and shown in Figure 5.15(left) as a function of pad index. The mean

value of the differences for all channels is found to be 1.42 ± 0.01 ADC counts with a RMS of 1.08 ± 0.01 ADC counts, as shown in Figure 5.15.

The mean value of the differences gives a systematic shift between two set of calibration constants. The reason is the difference of the timing offsets using different triggers, as explained in Section 5.6.3.

5.8 Conclusion

The calibration constants of the SiW ECAL prototype are extracted for each pad for the beam test in 2008 at FNAL. The average of the calibration constants over all pads is 47.61±0.02 ADC counts, and that of the statistical error is 0.516±0.002 ADC counts (1.08% of a MIP). The measured electronic noise is 5.930±0.003 ADC counts on average of all pads, thus a ratio about 7.95 is obtained between the calibration constant and the noise.

The total systematic error is 0.37 ADC counts (0.78% of a MIP) when they are applied to the data using the same trigger, while 1.04 ADC counts (2.18% of a MIP) when they are applied to the data with the other trigger.

The stability of the calibration constants are checked by comparing with those obtained for the beam test at CERN in 2006. The correlation coefficient is 83.76% between the calibration constants obtained at FNAL in 2008 and at CERN in 2006. Considering that plenty of operations like mounting, un-mounting, and shipment were applied on it between 2006 and 2008, this high correlation coefficient demonstrates the stability with time of the SiW ECAL prototype. The difference between the two sets of calibration constants can be understood from the difference of the timing offsets of employed triggers as required by different experimental conditions.

The result gives evidence that the calibration can also be well controlled for a full SiW ECAL in a detector at the ILC.

Chapter 6

Higgs Recoil Mass and Higgs-strahlung Cross Section Measurements

As discussed in Section 2.6, the Higgs-strahlung process $e^+e^- \rightarrow ZH$ offers an unique opportunity for a model independent precision measurement of the mass of Higgs bosons, by means of the recoil mass to the Z, with Z decays to e^+e^- (eeX-channel) or $\mu^+\mu^-$ ($\mu\mu X$-channel). At the same time, the Higgs-strahlung cross section and therefore also the coupling strength at the HZZ vertex can be determined.

This chapter presents the study of the Higgs recoil mass and Higgs-strahlung cross section measurements at the ILD detector concept. It is the major benchmark reaction proposed in the *Letter of intent Studies for ILC detectors*[38], and the results represented in this chapter are included in the *ILD Letter of Intent*[29]. The analysis is studied at $\sqrt{s} = 250$GeV with $M_H = 120$GeV, assuming an integrated luminosity of 250fb^{-1} corresponding to two years of data taking. The Monte Carlo (MC) production is based on the beam parameters given as "Nom.250" in Table 3.2. The events generated are then subjected to a detailed detector simulation of ILD. Unless otherwise stated, the figures and results are given with these conditions.

Two parallel analyses are performed. One is called *Model Independent (MI) Analysis*, where no assumption on the Higgs decay mode is made. The second one is named *Model Dependent (MD) Analysis*, for which, it is assumed that the Higgs decay products must result into at least two charged particles. Accompany with MI and MD analyses, different scenarios in the background rejection are composed.

In this chapter, the Monte Carlo production is introduced first, followed by the lepton identification and the selection of good lepton candidates. In Section 6.4, the variables for the background rejection are studied, the methods are presented and discussed, and the efficiency of the signal selection are given. Section 6.5 studies the methods to extract the Higgs mass and the cross section through fitting to the remaining signal plus background. Three fitting methods, which are either newly developed or updated, are studied in depth. In Section 6.6, the results are given. The discussions

and conclusions are given in Section 6.7. Where, the major effects that influencing the accuracies on the measurements of the Higgs recoil mass and Higgs-strahlung cross section are studied at first. A possible improvement on the eeX-channel by measuring the Bremsstrahlung photon is examined in the following. Finally, the potential systematic errors and solutions are discussed.

6.1 Monte Carlo Production

The Monte Carlo (MC) samples analyzed in this chapter are centrally generated by SiD optimization group[27, 28] using the version 1.40 of the event generator WHIZARD[36]. The luminosity spectrum is generated using GUINEA-PIG[37] with beam parameters named "Nom.250" given in Table 3.2 in Section 3.1. The resulting differential luminosity spectrum is shown on Figure 3.2 in the same section, with beam energy spread of 0.28% and 0.18% for electron and positron beams respectively. Both the Initial-State Radiation (ISR) and Final-State Radiation (FSR) are included in the event generation.

The generated signal and background samples together with their cross sections at $\sqrt{s} = 250$ GeV with $M_H = 120$ GeV are given in the Table 6.1 and 6.2 for the beam polarization modes $e^-_L e^+_R$ and $e^-_R e^+_L$, respectively. The two beam polarization modes are defined as:

$$\begin{aligned} e^-_L e^+_R : &\quad e^- : -80\% \; and \; e^+ : +30\% \\ e^-_R e^+_L : &\quad e^- : +80\% \; and \; e^+ : -30\% \end{aligned} \tag{6.1}$$

Process	Cross-Section
$\boldsymbol{\mu\mu X}$	**11.67 fb**
$\mu\mu$	10.44 pb (84.86 fb)
$\tau\tau$	6213.22 fb
$\mu\mu\nu\nu$	481.68 fb
$\mu\mu ff$	1196.79 fb

Process	Cross-Section
$\boldsymbol{eeX}$	**12.55 fb**
ee	17.30 nb (357.14 fb)
$\tau\tau$	6213.22 fb
$ee\nu\nu$	648.51 fb
$eeff$	4250.58 fb

Table 6.1: Processes and cross sections for polarization mode $e^-_L e^+_R$. The signal is indicated by bold face letters; the cross section in the parentheses of e^+e^- and $\mu^+\mu^-$ are that after Pre-Cuts, see Table 6.3 for the Pre-Cuts definition.

The MC samples generated are grouped into processes according to the final states. A process in Table 6.1 and 6.2 may include one or several reactions through different intermediate states. The processes and the major reactions they consist of, are defined in the following:

- $\boldsymbol{\mu\mu X}$: The Higgs-strahlung process with $Z \to \mu^+\mu^-$. It is the signal process of $\mu\mu X$-channel analysis.
- $\boldsymbol{eeX}$: This process includes two reactions. The dominant reaction is the Higgs-strahlung with $Z \to e^+e^-$, it is the signal reaction of the eeX-channel analysis. It also includes minor (~7%) contribution from the

Process	Cross-Section
$\boldsymbol{\mu\mu X}$	**7.87 fb**
$\mu\mu$	8.12 pb (58.26 fb)
$\tau\tau$	4850.05 fb
$\mu\mu\nu\nu$	52.37 fb
$\mu\mu ff$	1130.01 fb

Process	Cross-Section
$\boldsymbol{eeX}$	**8.43 fb**
ee	17.30 nb (335.47 fb)
$\tau\tau$	4814.46 fb
$ee\nu\nu$	107.88 fb
$eeff$	4135.97 rb

Table 6.2: Processes and cross sections for polarization mode $e^-_R e^+_L$. The signal is indicated by bold face letters; the cross section in the parentheses of e^+e^- and $\mu^+\mu^-$ are that after Pre-Cuts, see Table 6.3 for the Pre-Cuts definition.

ZZ Fusion ($e^+e^- \to e^+e^- Z^* Z^* \to e^+e^- H$), which is treated as a background in this analysis context.

$\boldsymbol{\mu\mu}$: A background process of $\mu\mu X$-channel analysis through intermediate states γ^* or Z.

$\boldsymbol{ee}$: A background process of eeX-channel analysis, consists of the Bhabha scattering, and annihilation reactions through intermediate states γ^* or Z.

$\boldsymbol{\tau\tau}$: This process is a background for both the $\mu\mu X$-channel and eeX-channel analyses, since the decay of the tau pair may create a pair of muons or electrons. After the lepton identification detailed in Section 6.2, events without a pair of muons or electrons will be removed. Also note that, the cross section of process $\tau\tau$ in Table 6.1 and 6.2 refers to the total cross section of the τ pair production.

$\boldsymbol{\mu\mu\nu\nu}$ / $\boldsymbol{ee\nu\nu}$: Background processes of $\mu\mu X$-channel and eeX-channel analyses, respectively. They consist mainly of the WW reaction with both W decay to a muon/electron with a corresponding neutrino. However, they also consist a minor fraction of ZZ reaction with one Z decaying to a pair of muons/electrons while the other one decaying to a pair of neutrinos.

$\boldsymbol{\mu\mu ff}$ / $\boldsymbol{eeff}$: Background processes of $\mu\mu X$-channel and eeX-channel analyses, respectively. They consist of reactions through intermediate states ZZ, $\gamma^*\gamma^*$, $Z\gamma^*$ or $\gamma^* Z$, and the f refers to all possible fermions excepts neutrinos.

The integrated luminosities of the MC samples are $\mathcal{L} = 10\,\mathrm{ab}^{-1}$ of the Higgs-strahlung process for each polarization mode. For the background processes, they are mostly larger than $250\,\mathrm{fb}^{-1}$, except for the $\tau\tau$ process, which is only 9 fb^{-1}[1]. In the histograms that shown in this chapter, the statistics are all scaled to the luminosity of 250 fb^{-1} as assumed, with error bars corresponding to 250 fb^{-1}.

Due to the large cross section of the ee and $\mu\mu$ processes, pre-cuts have been applied in order to reduce the simulation time. These cuts are given in Table 6.3 and will be

[1]Due to an initial mistake in the luminosity spectrum in event generation, a re-weighting algorithm[39] is applied in the background samples for correction.

ee process	$\mu\mu$ process
$\lvert cos\theta_{e^+/e^-}\rvert < 0.95$	
$\mathrm{M_{dl}} \in (71.18, 111.18)$ GeV	$\mathrm{M_{dl}} \in (71.18, 111.18)$ GeV
$\mathrm{P_{Tdl}} > 10$ GeV	$\mathrm{P_{Tdl}} > 10$ GeV
$\mathrm{M_{recoil}} \in (105, 165)$ GeV	$\mathrm{M_{recoil}} \in (105, 165)$ GeV

Table 6.3: Pre-Cuts for $e^+e^- \to e^+e^-$ and $e^+e^- \to \mu^+\mu^-$ production.

later on referred as *Pre-Cuts*. Here, $\mathrm{M_{dl}}$ is the invariant mass of the lepton pair of the Z decay; $\mathrm{P_{Tdl}}$ denotes the transverse momentum calculated from the vectorial sum of the two leptons; and $\mathrm{M_{recoil}}$ refers to the recoiling mass against the lepton pair system. These variables are discussed in Section 6.4.1.

Thereafter, the generated events are subject to a detailed ILD detector simulation. The simulation is performed with the MOKKA[40] software package which provides the geometry interface to the GEANT4[41] simulation toolkit. The event reconstruction is performed under the Marlin Framework[42], using the *LDC Tracking*[43] and *PandoraPFA*[31] as the tracking and particle plow algorithms, respectively. For this study the versions as contained in the software package *ILCSoft v01-06*[44] are employed.

6.2 Lepton Identification

The task of lepton identification (Lepton-ID) is to identify the muons and electrons produced in the decay of the Z. In a first step, the energy deposition in the ECAL (E_{ecal}), the total calorimetric energy (E_{total}) and the measured track momentum (P_{track}) are compared accordingly for each final state particle. The Lepton-ID is mainly based on the assumption that an electron deposits most of its energy in the ECAL while a muon passes both the ECAL and HCAL as a minimal ionizing particle. The observables and cut values are summarized in Table 6.4. The motivation of the cut values can be inferred from Figure 6.1 where the spectra for the corresponding lepton type in the relevant momentum range $P > 15\,\mathrm{GeV}$ compared with those from other particles are displayed.

	μ-Identification	e-Identification
E_{ecal}/E_{total}	< 0.5	> 0.6
E_{total}/P_{track}	< 0.3	> 0.9

Table 6.4: Variables and cut values for the Lepton-ID.

The criteria to estimate the quality of the Lepton-ID and hence the signal selection are the *Efficiency* and *Purity*. These are defined as follows:

$$\text{Efficiency} = \frac{N_{true \cap iden}}{N_{true}}$$

$$\text{Purity} = \frac{N_{true \cap iden}}{N_{iden}} \tag{6.2}$$

Here N_{true} defines the generated number of the corresponding lepton type and N_{iden} defines the identified number of leptons with the corresponding lepton type according to the selection criteria. For electrons and muons with $P > 15\,\text{GeV}$ in the signal samples the obtained values are listed in Tab. 6.5.

The efficiencies and purity are well above 95% except for the purity of the muon identification. This is caused by final state charged pions which pass the detector as minimal ionizing particles and which are indistinguishable from muons with the applied selection criteria. This deficiency is partially balanced by the fact that two leptons of the same type are required for the reconstruction of the Z and that they should yield the mass of the Z. Indeed, using the above selection cuts, without the $P > 15\,\text{GeV}$ request, the efficiency to identify a pair of leptons from the Z decay is 95.4% for the case $Z \to \mu\mu$ and 98.8% for the case $Z \to \text{e}^+\text{e}^-$.

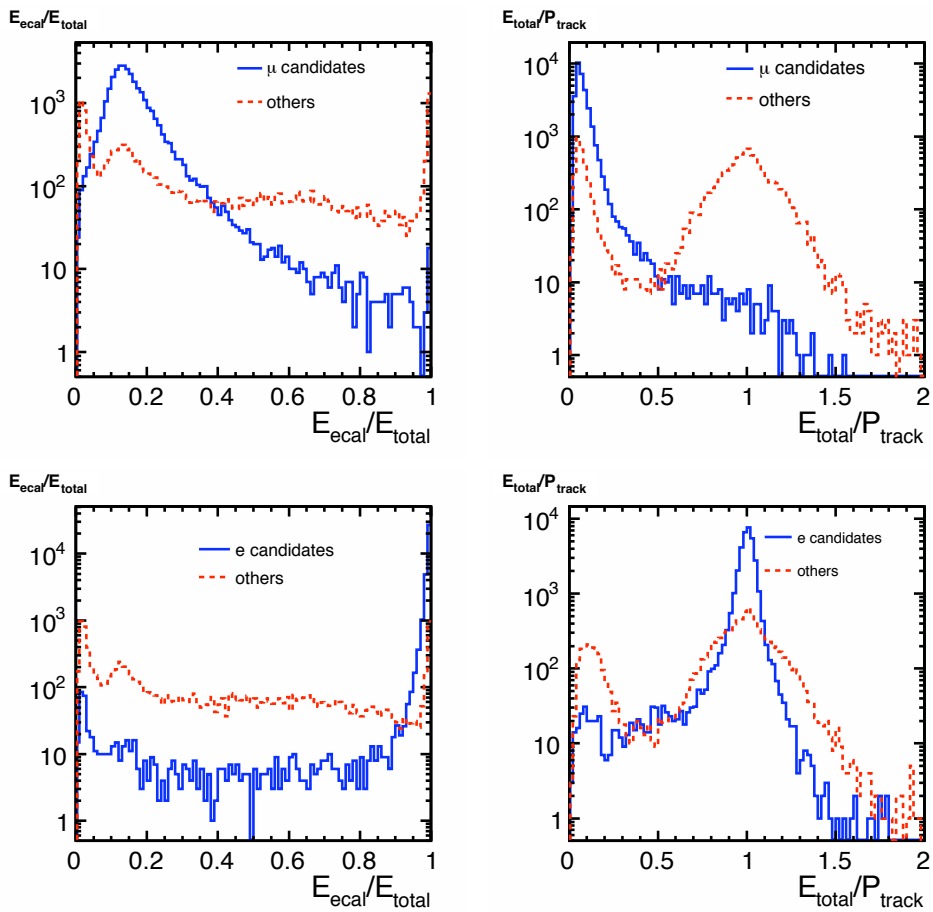

Figure 6.1: Distributions of the variables for Lepton-ID of lepton candidates and other particles with $P > 15\,\text{GeV}$.

	μ ID in $\mu\mu X$	e ID in eeX
N_{true}	31833	34301
$N_{true \cap iden}$	31063	33017
N_{iden}	33986	34346
Efficiency	97.6%	96.3%
Purity	91.4%	96.1%

Table 6.5: Lepton-ID Efficiency and Purity for reconstructed particles with $P > 15\,\text{GeV}$, where *Efficiency* and *Purity* are defined in Equation 6.2.

6.3 Track Selection

As the invariant mass of the lepton pair system and thus the recoil mass will be calculated from the four momenta reconstructed from the tracks, badly measured tracks need to be discarded from the analysis. The track quality can be estimated by the ratio $\Delta P/P^2$ where the uncertainty ΔP is derived from the error matrix of the given track by error propagation.

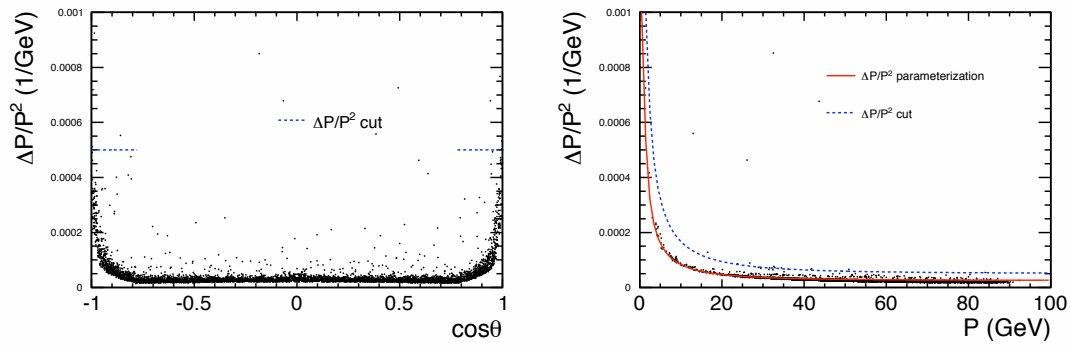

Figure 6.2: 2D $\Delta P/P^2$ distribution vs. $cos\theta$ (left) and $\Delta P/P^2$ distribution vs. track momentum (right) of muon candidates decayed from Z^0 of Higgs-strahlung process.

Figure 6.2 and 6.3 show, for muons and electrons separately, the dependency of $\Delta P/P^2$ on the polar angle $cos\theta$ and on the track momentum P. For reasons discussed in the following the latter has been restricted to $|cos\theta| < 0.78$, i.e. the central region. For both variables the distributions exhibit for muon tracks a narrow band with well measured momenta equivalent to small $\Delta P/P^2$. The track quality decreases as expected towards large $|cos\theta|$, i.e. towards the acceptance limits of the TPC which motivates the restriction to the central region when displaying $\Delta P/P^2$ versus P. These distributions show a decrease in track quality towards small particle momenta as expected from multiple scattering effects. Beyond that, the number of badly measured tracks and the low momentum tracks are much more abundant for electrons than for muons, with the reason discussed in Section 3.2.2.

Based on the momentum resolution given by Equation 3.1 in Section 3.2.2, the procedure for track selection is developed as

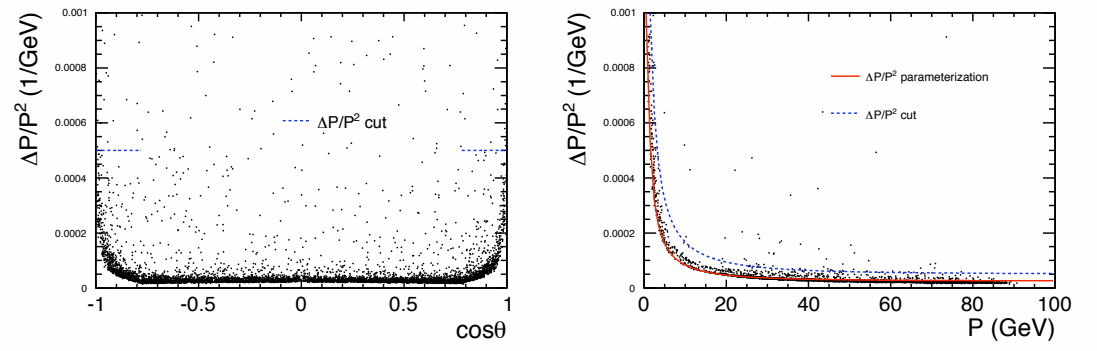

Figure 6.3: 2D $\Delta P/P^2$ distribution vs. $cos\theta$ (left) and $\Delta P/P^2$ distribution vs. track momentum (right) of electron candidates decayed from Z^0 of Higgs-strahlung process.

- For $|cos\theta| < 0.78$ the shape of $\Delta P/P^2$ versus P is approximated by:

$$\Delta P/P^2 = a \oplus b/P; \text{ with } a = 2.5 \times 10^{-5} \text{ (GeV}^{-1}) \text{ and } b = 8 \times 10^{-4} \tag{6.3}$$

  Tracks are rejected if $\Delta P/P^2 > 2\delta(1/P)$

- For $|cos\theta| > 0.78$ tracks are rejected if $\Delta P/P^2 > 5 \times 10^{-4}(GeV^{-1})$

The cuts are indicated in Figure 6.2 and 6.3. The tracks created by electrons are rejected considerably more often, which will reduce the number of reconstructed Z in the corresponding channel.

6.4 Background Rejection

The recoil mass analysis is based on the identification of the lepton pair system as produced by the decay of the Z. It is thus necessary to distinguish the processes which lead to two leptons in the final state as given in Table 6.1 and Table 6.2 from the ones produced in the Higgs-strahlungs process. This is a procedure named as background rejection or signal selection.

The background rejection can be accomplished by looking for differences between the signal and background, based on the physics beneath them. In practice, it is a procedure to search for common variables that can distinguish the signal and the background. Once the common variables are identified, one can either apply direct cuts on them, or employ them to construct a multi-variate analysis (e.g. the Likelihood), or both.

This section includes three subsections: Section 6.4.1 introduces the variables that can be employed as the criteria for background rejection. Section 6.4.2 shows the first step background rejection based on cuts, where the cut-chains with assumptions of MI and MD are given. Section 6.4.3 presents the Likelihood method for the further rejection after the first step cut-based rejection.

The tables of number of events remaining after each step of background rejection, for both the signal and background, with both the MI and MD assumptions, are put in Appendix B.

6.4.1 Variables for Background Rejection

Before describing the procedures of the background rejection, it is informative to introduce and discuss the common variables that can distinguish the signal and the background effectively.

The transverse momentum of the lepton pair system.

The transverse momentum of the lepton pair is noted as $\mathrm{P_{Tdl}}$. The normalized distributions of $\mathrm{P_{Tdl}}$ for signal and background are shown in Figure 6.4.

Based on the angular distribution given by Equation 2.28, the $\mathrm{P_{Tdl}}$ distribution of Higgs-strahlung process can be expressed as:

$$f(\mathrm{P_{Tdl}}) \propto \left[8M_Z^2/(s\lambda) + \frac{\mathrm{P_{Tdl}}^2}{|\mathbf{P}_Z|^2}\right]\frac{\mathrm{P_{Tdl}}}{|\mathbf{P}_Z|}\frac{1}{\sqrt{|\mathbf{P}_Z|^2 - \mathrm{P_{Tdl}}^2}}; \qquad \mathrm{P_{Tdl}} < |\mathbf{P}_Z| \tag{6.4}$$

As confirmed by Figure 6.4, in case of the Higgs-strahlung process, the distribution of $\mathrm{P_{Tdl}}$ given by Equation 6.4 increases towards large $\mathrm{P_{Tdl}}$ value with a maximum at $|\mathbf{P}_Z| \sim 66$ GeV.

For processes ee and $\mu\mu$, in case of no radiative effects, the pair of leptons are produced back-to-back, thus the $\mathrm{P_{Tdl}}$ should be zero. In case of radiative effects, such as the ISR, it is possible that a large transverse momentum is hold by the ISR, thus, a large $\mathrm{P_{Tdl}}$ is required for balancing. However, the radiation effects are minor compared to the large cross sections of these two processes. Therefore, this cut is very efficient. The survived events after this cut will be more effectively removed by $\mathrm{P_T}$ balance between the ISR photon and the lepton pair system, this will be discussed later.

For the $\tau\tau$ process, with a pair of muons or electrons in the $\tau\tau$ decay, the $\mathrm{P_{Tdl}}$ is maximized at small value. It is discussed separately:

1. A muon pair created from the $\tau\tau$ decay: Dominantly, this can happen when both the $\tau^+\tau^-$ decay as $\tau^+ \rightarrow \mu^+\nu_\mu\bar{\nu_\tau}$ and $\tau^- \rightarrow \mu^-\bar{\nu_\mu}\nu_\tau$, respectively. Different from ee and $\mu\mu$ processes, the momenta of the $\mu^+\mu^-$ decayed from $\tau\tau$ do not equal in amount, since there are also neutrinos produced. However, the angular distribution of $\tau^+\tau^-$ is maximized at ± 1 ($\propto (1+cos^2\theta)$), and the 1.78GeV τ mass is negligible compared to momentum of the τ (on average $P_\tau \sim \sqrt{\mathrm{s}}/2 = 125\mathrm{GeV}$), so the decay products ($\mu\nu\nu$) will fallow the same direction as τ. As a result, the $\mathrm{P_{Tdl}}$ of the $\mathrm{e^+e^-}$ or $\mu^+\mu^-$ system cannot be large.

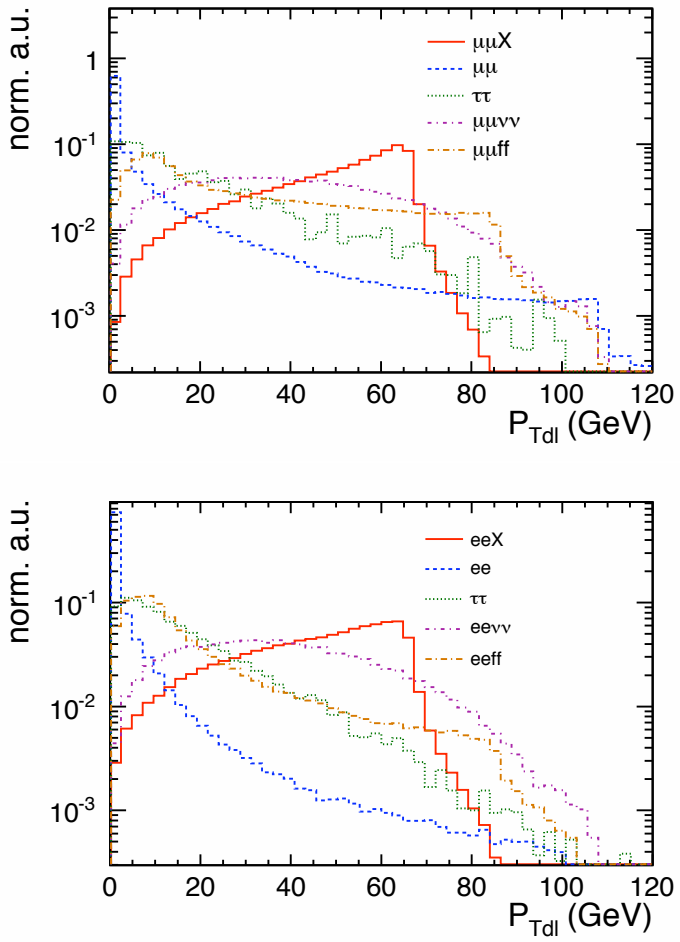

Figure 6.4: P_{Tdl} distributions of $\mu\mu X$ (left) and eeX (right), and of their corresponding backgrounds.

2. An electron pair created from the $\tau\tau$ decay: Two major reactions can make it happen. One is the same as a muon pair creation, both the $\tau^+\tau^-$ decay to an electron/positron with two neutrinos. The other is that one of the $\tau^+\tau^-$ decays to $\pi^-\pi^0\nu_\tau$ or $\pi^+\pi^0\bar{\nu_\tau}$, with $\pi^0 \to e^+e^-$. In this case, the e^+e^- system will follow the direction of the τ they decayed from, thus, the P_{Tdl} is small.

The $ee\nu\nu$ and $\mu\mu\nu\nu$ processes, are mostly through the WW intermediate state, where the pair of electrons or muons are coming from different W. Given a W mass of 80 GeV, the decay products will not follow the direction of W. As a result, the angular distribution of the pair of leptons decayed from the WW is isotropic, thus the P_{Tdl} distribution is also isotropic.

The $eeff$ and $\mu\mu ff$ processes include reactions through intermediate states of ZZ, $\gamma^*\gamma^*$, $Z\gamma^*$ or γ^*Z. However, for all the possible cases, their angular distributions are maximized at ± 1. Thus, the P_{Tdl} of the lepton pair decayed from either Z or γ^* are

small.

The cosine of the polar angle θ of the lepton pair system.

The cosine of the polar angle of the lepton pair system is noted as $\cos\theta_{\mathrm{dl}}$. The distributions of $\cos\theta_{\mathrm{dl}}$ for signal and background are shown in Figure 6.5.

The $\cos\theta_{\mathrm{dl}}$ of the Higgs-strahlung process is the $cos\theta$ of Z. The angular distribution of the Higgs-strahlung is given by Equation 2.28. From the equation, it is clear that the distribution of $\cos\theta_{\mathrm{dl}}$ of Higgs-strahlung is actually a parabola opened downwards, maximized in the central region, while that of the background is not.

The $\cos\theta_{\mathrm{dl}}$ is a variable strongly correlated with the $\mathrm{P_{Tdl}}$, which can be expressed as a function of $\mathrm{P_{Tdl}}$:

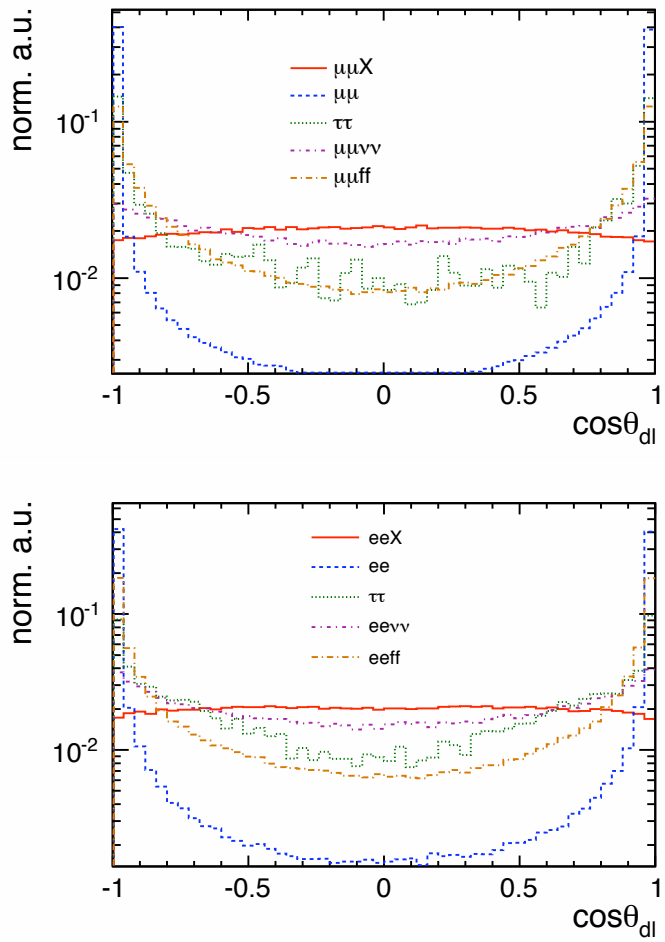

Figure 6.5: $\cos\theta_{\mathrm{dl}}$ distributions of $\mu\mu X$ (left) and eeX (right), and of their corresponding backgrounds.

$$\cos\theta_{\mathrm{dl}} = \sqrt{1 - \frac{\mathrm{P_{Tdl}}^2}{|\mathbf{P_{dl}}|^2}} \ . \tag{6.5}$$

Thus, it is straightforward to understand the distributions of $\cos\theta_{\mathrm{dl}}$ after the discussion on the $\mathrm{P_{Tdl}}$, which is given before. Therefore, if the $\mathrm{P_{Tdl}}$ distribution is maximized at small value, that of the $\cos\theta_{\mathrm{dl}}$ is maximized at ± 1; and if the $\mathrm{P_{Tdl}}$ distribution is isotropic, that of the $\cos\theta_{\mathrm{dl}}$ is also isotropic.

The Acollinearity and Acoplanarity of the pair of leptons.

The acollinearity and acoplanarity of the pair of leptons are defined as:

$$acol = cos^{-1}\left(\frac{\mathbf{P_1} \cdot \mathbf{P_2}}{|\mathbf{P_1}||\mathbf{P_2}|}\right) , \tag{6.6}$$

$$acop = cos^{-1}\left(\frac{\mathbf{P_{T1}} \cdot \mathbf{P_{T2}}}{|\mathbf{P_{T1}}||\mathbf{P_{T2}}|}\right) , \tag{6.7}$$

where 1 and 2 refer to the two leptons in the lepton pair, $\mathbf{P_T} = P_x\hat{\mathbf{x}} + P_y\hat{\mathbf{y}}$ and $\mathbf{P} = P_x\hat{\mathbf{x}} + P_y\hat{\mathbf{y}} + P_z\hat{\mathbf{z}}$.

Figure 6.6 and 6.7 show the acollinearity and acoplanarity, respectively, for the signal and background. Once the distributions of *acol* can be understood, that of the *acop* is understood accordingly, since *acop* is nothing more than a projection of the *acol* to the X-Y (or R-Φ) plane.

In case that the lepton pair comes from a Z decay, deriving from Equation 6.6, using energy and momentum conservations and Lorenz transformation, the *acol* can be expressed as:

$$acol = cos^{-1}\left(1 - \frac{2}{\gamma^2 - (\gamma^2 - 1)cos^2\theta^*}\right) , \tag{6.8}$$

where, θ^* is the polar angle of one of the leptons in the rest frame of the Z, and $\gamma = E_Z/M_Z$ is the Lorenz factor. Due to the Lorenz boost of the Z, a clear Jacobian peak should appear for $\theta^* = \pi/2$ in the acollinearity distribution, with its position determined by γ.

For the Higgs-strahlung process, from Equation 2.30 with $\sqrt{\mathrm{s}} = 250$ GeV, $\mathrm{M_H} = 120$ GeV and $\mathrm{M_Z} = 91.2$ GeV, one can get the $\gamma = 1.24$. Thereafter, taking this γ and $\theta^* = \pi/2$ into Equation 6.8, the position of the Jacobian peak at $acol = 1.90$ can be derived, which can be confirmed by Figure 6.6.

For the *ee* and $\mu\mu$ processes, this Jacobian peak only appears in case of an energetic ISR, which allows the reaction going through the intermediate state of a highly boosted Z. In this case, by simply removing the $\mathrm{M_H}$ term from Equation 2.30, and following the same calculation as for the Higgs-strahlung, one can get the Jacobian peak at

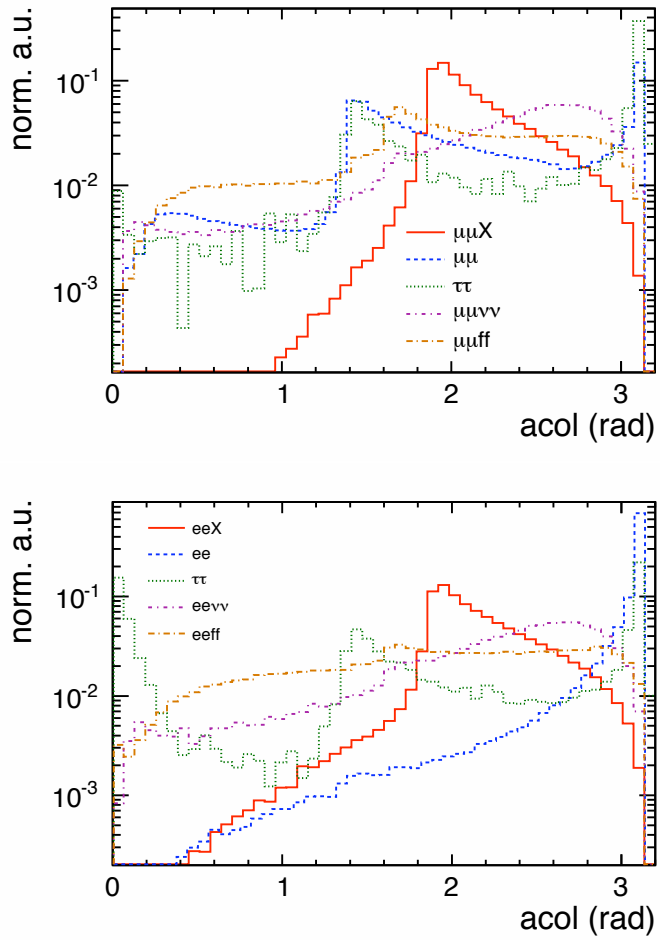

Figure 6.6: *acol* distributions of $\mu\mu X$ (left) and eeX (right), and of their corresponding backgrounds.

$acol = 1.4$. However, in most of the cases, they do not react through the Z intermediate state, where, a maximum at $acol = \pi$ is expected. This is extremely true for the ee process, since it is dominantly the Bhabha scattering, as shown in Figure 6.6(bottom).

The process $\tau\tau$ can be understood similarly as $\mu\mu$ or ee process, in the case that the pair of muons or electrons come from different taus. However, in case of a pair of electrons in the decay products, and they come from a single tau, a maximum at $acol = 0$ is expected, since they are following the same direction, as can be observed in Figure 6.6(bottom).

For processes $eeff$ and $\mu\mu ff$, two Jacobian peaks can appear, which corresponding to two possible intermediate states, ZZ and $Z\gamma^*$, and for both of them the pair of leptons should decay from the Z. In case of the ZZ intermediate state, by substituting M_H with M_Z in Equation 2.30, a Jacobian peak at $acol = 1.6$ can be calculated. In case of the $Z\gamma^*$ intermediate state, a same Jacobian peak at $acol = 1.4$ as the ee or $\mu\mu$ process can

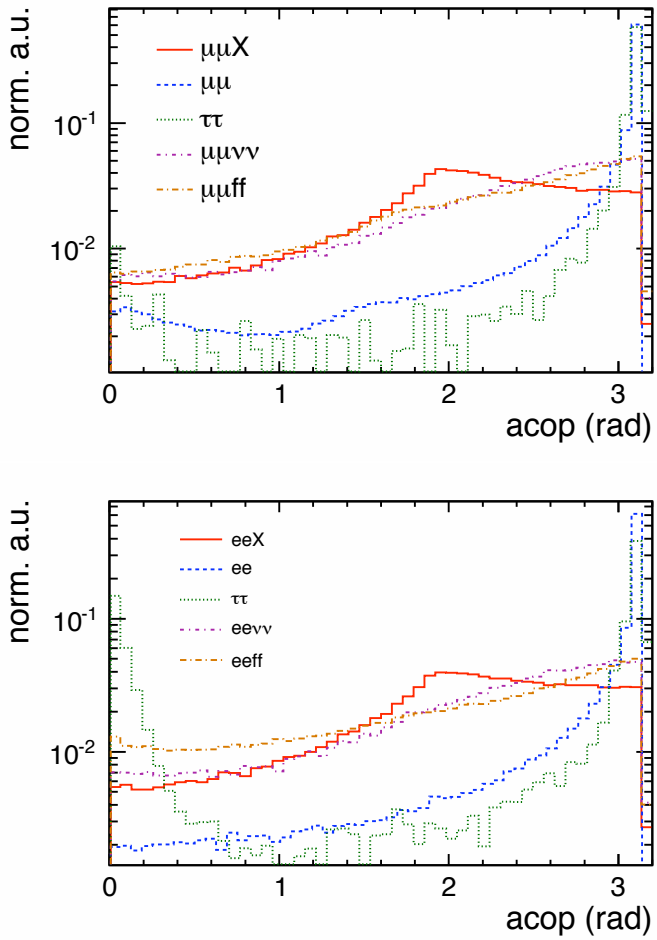

Figure 6.7: *acop* distributions of $\mu\mu X$ (left) and eeX (right), and of their corresponding backgrounds.

be derived.

While for the $ee\nu\nu$ and $\mu\mu\nu\nu$, the *acol* is randomly distributed due to the same reason that discussed for P_{Tdl} and $\cos\theta_{dl}$.

The invariant mass and recoil mass of the lepton pair system.

The invariant mass (M_{dl}) and recoil mass (M_{recoil}) of the lepton pair system, are shown in Figures 6.8 and 6.9, respectively, for signal and background. They are given by Equation 2.34.

In the Higgs-strahlung process, the M_{dl} is the M_Z, which is maximized at 91.2GeV, and the M_{recoil} gives the Higgs mass M_H. The M_{dl} distribution features a Breit-Wigner shape symmetrical with respect to M_Z. The observed M_Z distribution has a tail to the smaller value, see Figure 6.8. This is due to the FSR and the Bremsstrahlung

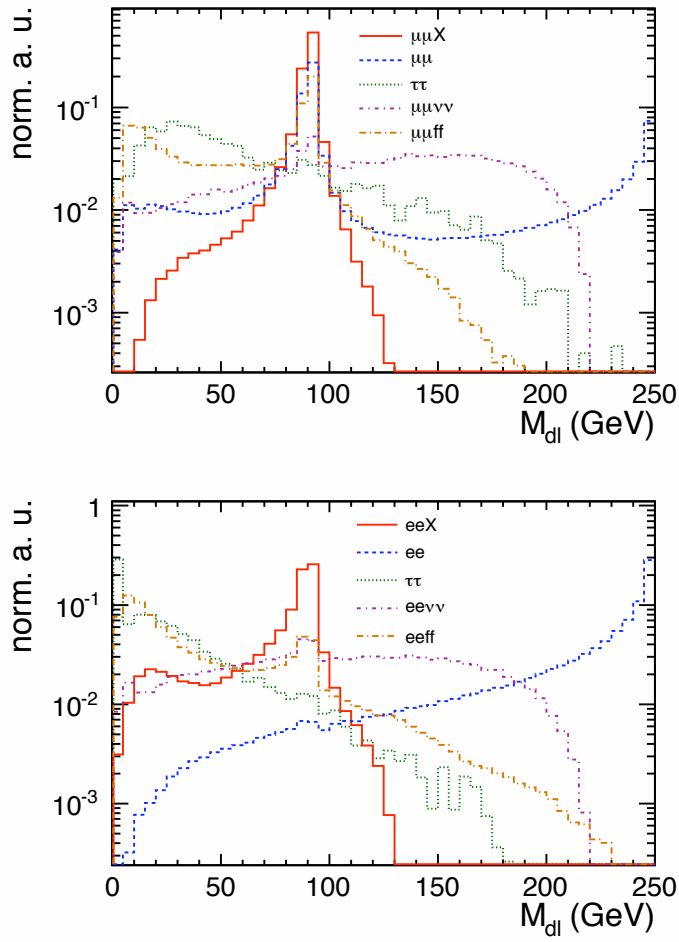

Figure 6.8: M_{dl} distributions of $\mu\mu X$ (top) and eeX (bottom), and of their corresponding backgrounds.

energy losses. One may noticed that in Figure 6.8(bottom), there is an accumulation of events at small value in the eeX-channel. This is due to the contaminations of the photon conversions. In which, the electron pair converted from a radiation photon is mis-selected as the signal event.

Turning to the M_{recoil} distribution. It is already discussed in Section 2.6. However, as can be observed in Figure 6.9(top), there is a sudden decrease in the distribution at around 159 GeV in the $\mu\mu X$-channel. As introduced in Section 2.6, the M_{recoil} distribution is a convolution of smearing effects and radiative effects, where the radiative effects consist of Beamstrahlung, ISR, FSR and Bremsstrahlung (only affecting eeX-channel). Among these radiative effects, the Beamstrahlung and ISR are limited by the mass threshold $M_H + M_Z$. Taking this mass threshold into Equation 2.34, the M_{recoil} at the mass threshold is calculated to be 159 GeV. In other words, the Beamstrahlung and ISR cannot contribute to the tail that greater than 159 GeV, while the FSR still can. This sudden decreasing is hardly visible in eeX-channel, since it is overwhelmed

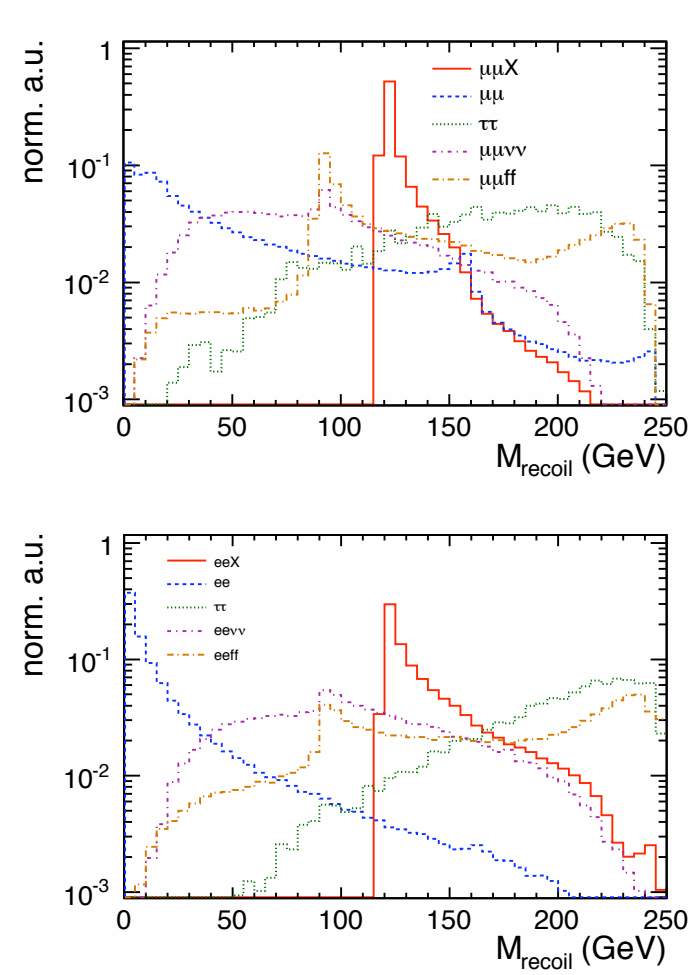

Figure 6.9: M_{recoil} distributions of $\mu\mu X$ (top) and eeX (bottom), and of their corresponding backgrounds.

by the Bremsstrahlung effect.

For the $\mu\mu$ process, in case of the muon pair comes from a Z decay, a maximum at $M_Z = 91.2$ GeV in the M_{dl} distribution with a corresponding maximum at $\sqrt{s} - M_Z = 159$ GeV in the M_{recoil} distribution can be observed, as shown in Figure 6.8(top) and Figure 6.9(top), respectively. These two maxima are nearly invisible in process ee, since it is dominantly the Bhabha scattering, as shown in Figure 6.8(bottom) and Figure 6.9(bottom).

Similarly, for the $eeff$ and $\mu\mu ff$ processes, in case of the lepton pair comes from a Z decay, the M_{dl} forms a M_Z. However, in the M_{recoil} distribution, the intermediate state of ZZ can give a maximum at M_Z, as shown in Figure 6.9. While all the other intermediate states can be discussed accordingly.

For processes $ee\nu\nu$, $\mu\mu\nu\nu$ and $\tau\tau$, since the lepton pair in their final states is mostly coming from different particles, both their M_{dl} and M_{recoil} distributions are rather

isotropic.

To the end of background rejection, the request that M_{dl} around M_Z is applied, which is also served as a rejection of the FSR events in the Higgs-Strulung; and the M_{recoil} cut is applied as the fit window, i.e. $M_{recoil} > 115$GeV and $M_{recoil} < 150$GeV in this study.

The P_T balance between the ISR photon and the lepton pair system.

Due to the large cross sections of the background processes ee and $\mu\mu$, the rejections using the variables previously introduced are not sufficient. However, it is found that the remaining events are mostly associated with a high energetic ISR radiation. Therefore, in case of an energetic ISR radiation having a high transverse momentum, the lepton pair could gain an equal transverse momentum to balance it.

Figure 6.10(top) shows the correlation between the transverse momentum of the muon pair (P_{Tdl}) and that of the identified most energetic photon ($P_{T\gamma}$) for process

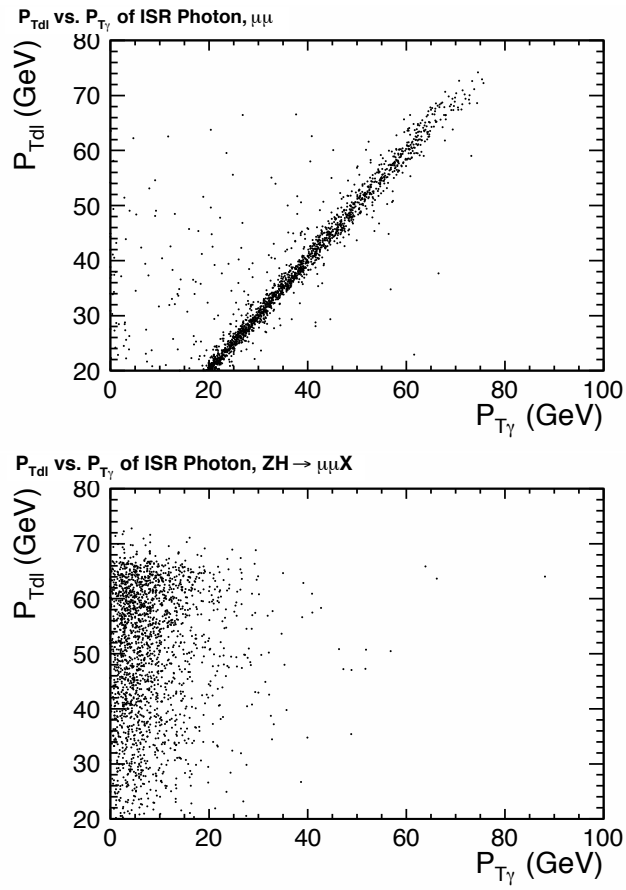

Figure 6.10: Correlation between P_{Tdl} and $P_{T\gamma}$ for the $\mu\mu$ process (top) and for the Higgs-strahlung $\mu\mu X$ process (bottom).

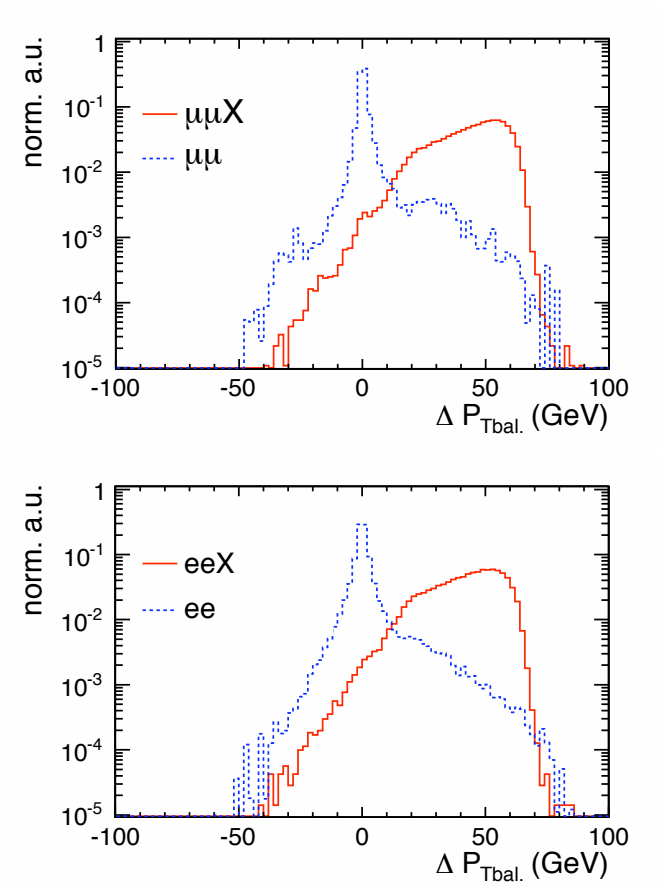

Figure 6.11: $\Delta P_{Tbal.}$ distributions of Higgs-strahlung and $\mu\mu/ee$ backgrounds for the $\mu\mu X$-channel (top) and eeX-channel (bottom).

$\mu\mu$. Here, the identified most energetic photon is assumed to be created by ISR. In this figure, a strong correlation can be observed between these two transverse momenta. However, for the Higgs-strahlung $\mu\mu X$ process, no such a correlation can be found, as shown in Figure 6.10(bottom).

Thereafter, a variable $\Delta P_{Tbal.}$ is defined as:

$$\Delta P_{Tbal.} = P_{Tdl} - P_{T\gamma} \ , \tag{6.9}$$

where, $P_{T\gamma}$ is the transverse momentum of the ISR photon.

Figure 6.11 shows the $\Delta P_{Tbal.}$ distributions of the signal Higgs-strahlung process and the background $ee/\mu\mu$ processes. In the figure, a strong maximum at zero can be observed in the distributions of ee and $\mu\mu$ processes, however, not of the Higgs-strahlung.

There are two essential cuts should be applied before the $\Delta P_{Tbal.}$:

- The P_{Tdl} cut: E.g. $P_{Tdl} > 20$ GeV. This cut enables the lepton pair in the

remaining events of $\mu\mu$ and ee processes having a sizable transverse momentum, which is the hypothesis to construct the $\Delta P_{Tbal.}$ variable.

- The M_{dl} cut: E.g. $M_{dl} \in (80, 100)$ GeV. This cut selects the events of $\mu\mu$ and ee processes that forming a Z, which are always accompanied by an energetic ISR radiation. At the same time, the lower boundary of M_{dl} cut removes the events with larger FSR and Bremsstrahlung. So that, it enforces the correlation between the two transverse momenta.

Number of additional tracks besides the two lepton candidates

The number of additional tracks besides the two lepton candidates is noted as $N_{add.TK}$. This is a model dependent variable, assuming the Higgs decay products should be visible and at least contain two charged tracks. Based on this assumption, for the Higgs-strahlung process, the number of additional tracks besides the two tracks from the Z decay, $N_{add.TK}$, should be greater than two, which come from the Higgs decay.

However, for the background processes ee, $\mu\mu$, $\tau\tau$, $ee\nu\nu$ and $\mu\mu\nu\nu$, ideally, the $N_{add.TK}$ should be zero. Therefore, this variable itself can efficiently separate the Higgs-strahlung process from the background processes just mentioned. It should be noticed that, the variable $N_{add.TK}$ does not work for the background processes $eeff$ and $\mu\mu ff$. This is due to the fact that with one of the Z or γ^* decays to a pair of electrons or muons, the other one has a large chance to create more than 2 tracks, e.g. $Z \rightarrow hadron\ jets$ has a branching ratio of about 70%.

Figures 6.12 and 6.13 show the $N_{add.TK}$ distributions of the Higgs-strahlung and

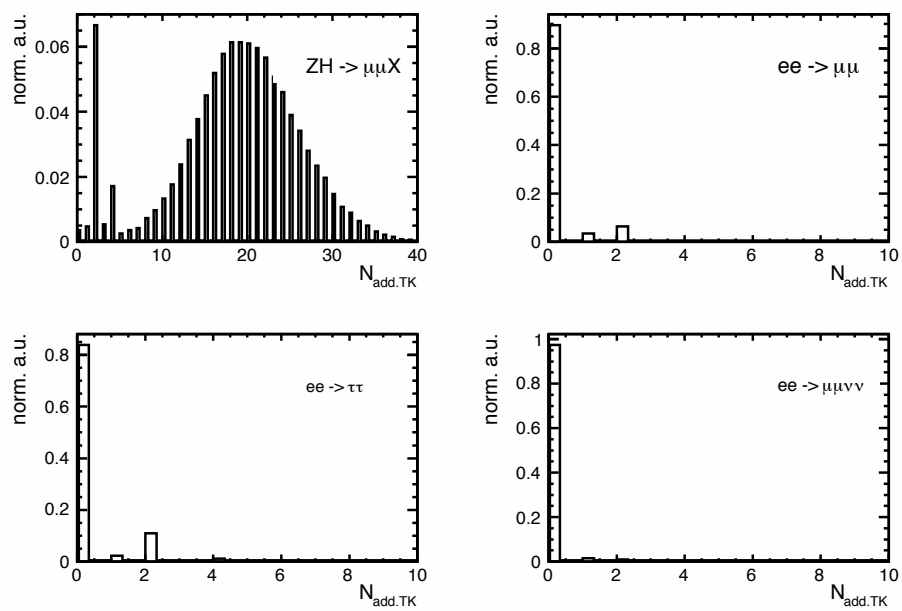

Figure 6.12: $N_{add.TK}$ distributions for signal and background in the $\mu\mu X$-channel.

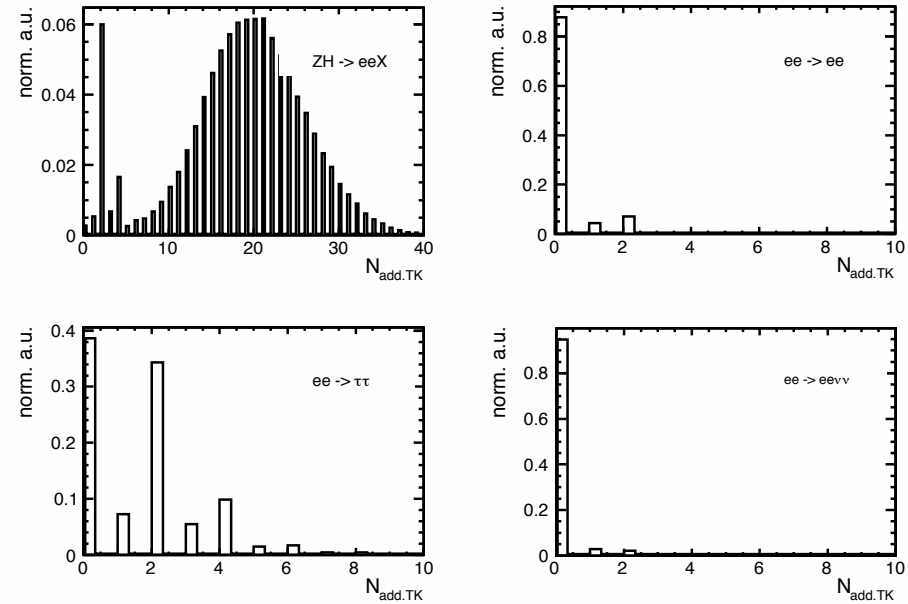

Figure 6.13: $N_{add.TK}$ distributions for signal and background in the eeX-channel.

the corresponding background processes as labeled, for $\mu\mu X$-channel and eeX-channel, respectively. Since the MC generation of the Higgs-strahlung assumes the Higgs decay SM like, its $N_{add.TK}$ are mostly much greater than two. While for the corresponding background, dominantly, the $N_{add.TK}$ are zero. As can be observed in the distributions of the background, there are also many events with $N_{add.TK} \geq 2$. This is mainly due to the ISR photon conversions that creating additional charged tracks. In case of $\tau\tau$ process, especially with the tau pair goes to a pair of electrons, much more events with $N_{add.TK} > 2$ can be observed than other background. This is due to the complicate τ decay scenario as discussed before.

Looking back to the signal distribution, the figure shows a maximum at $N_{add.TK} = 2$, which is mainly the $H \to \tau^+\tau^-$ in the SM Higgs decay scenario. In order to keep these events, the cut on $N_{add.TK}$ at most could be $N_{add.TK} > 1$. To suppress the backgrounds with $N_{add.TK} > 1$, the other variables discussed before should be applied together with $N_{add.TK}$. At the same time, for the additional tracks created due to the ISR photon conversions, two angular variables are studied in the following.

Polar angle difference between the two additional tracks for events with $N_{add.TK} = 2$, and the minimal polar angle difference between the lepton candidates and the additional tracks

In case of an energetic ISR photon radiated, the ISR photon may convert to a pair of charged tracks without difference between their polar angles. The photon conversion is responsible for the accumulation of event with $N_{add.TK} = 2$ in the background processes ee, $\mu\mu$ and $\tau\tau$, which is visible in Figure 6.12 and 6.13. It is also the reason for the

larger tail on the right side of the maximum in the $\Delta P_{\mathrm{Tbal.}}$ distribution of processes ee and $\mu\mu$, as shown in Figure 6.11. However, the last introduced cut $N_{\mathrm{add.TK}} > 1$ cannot remove these background events with ISR photon conversion.

Therefore, a variable noted as $|\Delta\theta_{2\mathrm{tk}}|$ is introduced, which is defined as the polar angle difference between the two additional tracks for events with $N_{\mathrm{add.TK}} = 2$. As shown in Figure 6.14, the $|\Delta\theta_{2\mathrm{tk}}|$ for $\mu\mu$ and ee are almost zero, while that of the Higgs-strahlung are isotropically distributed. The difference is due to the fact that, in the Higgs-strahlung process, the two additional tracks are coming from the Higgs decay, mostly $H \to \tau^+\tau^-$ in case of the Higgs decays SM like. Moreover, the only chance of this variable to lose its generality is that, the Higgs decay is invisible and there is an energetic ISR photon conversion with a sizable transverse momentum. However, with the mass threshold of the Higgs-strahlung process, the probability to have this special case is assumed to be extremely small.

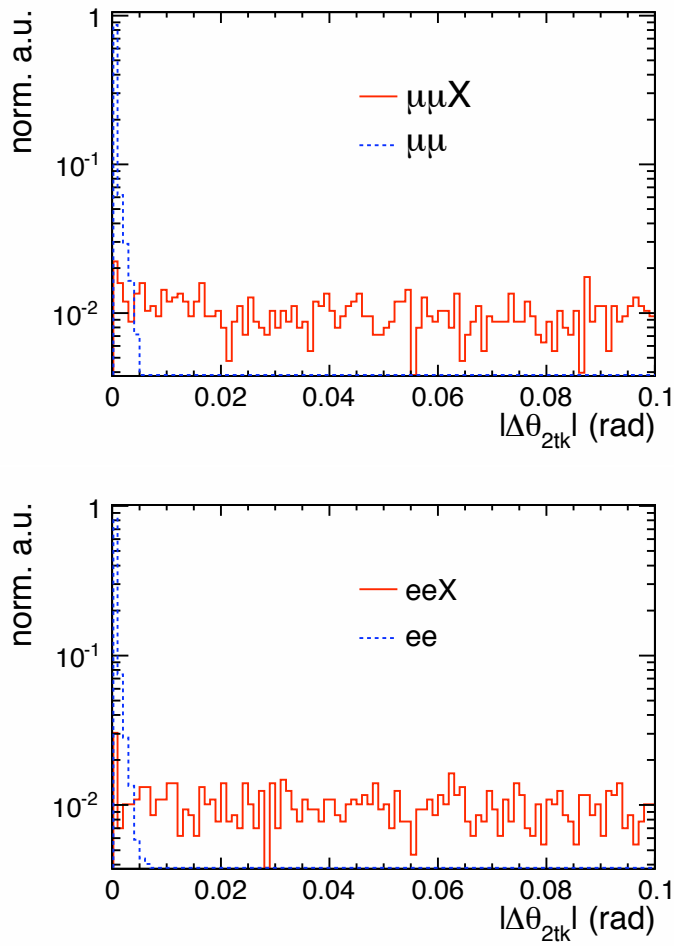

Figure 6.14: $|\Delta\theta_{2\mathrm{tk}}|$ distributions of Higgs-strahlung and $\mu\mu/ee$ backgrounds for the $\mu\mu X$-channel (top) and eeX-channel (bottom).

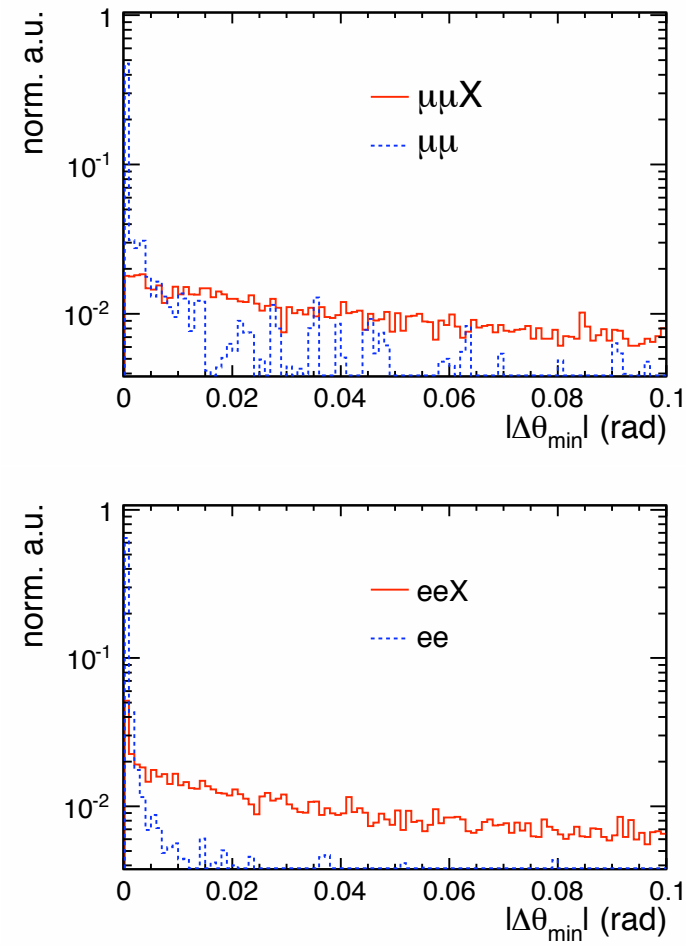

Figure 6.15: $|\Delta\theta_{\text{min}}|$ distributions of Higgs-strahlung and $\mu\mu/ee$ backgrounds for the $\mu\mu X$-channel (top) and eeX-channel (bottom).

Due to the reason that there exists certain misidentification of the leptons, certain photon conversions are misidentified as the lepton candidates. In order to remove these background events, an additional variable noted as $|\Delta\theta_{\text{min}}|$ is introduced. The $|\Delta\theta_{\text{min}}|$ is defined as the minimal polar angle difference between the lepton candidates and the additional tracks. As can be seen in Figure 6.15, the $|\Delta\theta_{\text{min}}|$ can also provide an excellent separation of the Higgs-strahlung process and the background processes $\mu\mu$ and ee. Furthermore, the variable $|\Delta\theta_{\text{min}}|$ is only calculated for events with $\text{N}_{\text{add.TK}} < 10$, since there are nearly no events with more than 10 additional tracks for the background shown in Figure 6.12 and 6.13.

The missing *cosθ*

The missing *cosθ* is noted as $|\cos\theta_{\text{missing}}|$, which refers to the polar angle of the total momentum of the particles that cannot be detected by the detector. These particles

are named as *missing particles* in the following. The $|\cos\theta_{\text{missing}}|$, therefore, can be calculated from the momenta of the detected particles, as given by

$$|\cos\theta_{\text{missing}}| = \frac{|\sum P_{z,missing}|}{|\sum \mathbf{P}_{missing}|} = \frac{|0 - \sum P_{z,detected}|}{|0 - \sum \mathbf{P}_{detected}|} = \frac{|\sum P_{z,detected}|}{|\sum \mathbf{P}_{detected}|} \ . \tag{6.10}$$

The missing particles can be divided into two categories:

- Physically undetectable (invisible) particles, i.e. neutrinos.
- The particles that fall into the dead regions of the detector. They are dominantly the ISR photons that go along the beam pipe.

In general, the $|\cos\theta_{\text{missing}}|$ distribution is resulting from the combined effect of these two categories of missing particles in the reaction final states.

In case of the dominant effect comes from invisible particles in the final states, the $|\cos\theta_{\text{missing}}|$ distribution is depending on the polar angles of them. For instance the processes $\mu\mu\nu\nu$ and $ee\nu\nu$, the neutrinos in the final states are evenly distributed in the polar angle. Therefore, the $|\cos\theta_{\text{missing}}|$ distribution is almost isotropic, as shown in Figure 6.16.

For the ISR photons that go along the beam pipe, the dominance of their effect is depending on how energetic they are. And the possible energies of the ISR photons are restricted by the mass threshold of a particular reaction. The $\tau\tau$ process is a good example. This process has considerable amount of neutrinos in the final states. However, it has no mass threshold to restrict the energies of the ISR photons. The ISR photon can be energetic enough to dominate the $|\cos\theta_{\text{missing}}|$ distribution. As the result, the $|\cos\theta_{\text{missing}}|$ is strongly maximized at one due to the energetic ISR photons, with a sizable tail to zero due to the effect from the neutrinos, as shown in Figure 6.16. Comparing with the processes $\mu\mu\nu\nu$ and $ee\nu\nu$, in which a mass threshold of $2\mathrm{M_W}$ restricts the energies of the ISR photons. As a result, the effect of ISR photons is not dominant, and the $|\cos\theta_{\text{missing}}|$ distribution is much isotropic than that of the $\tau\tau$ process.

For the Higgs-strahlung, ee, $\mu\mu$, $eeff$ and $\mu\mu ff$ processes, there are either no, or only minor neutrino composition in their final states. Therefore, their $|\cos\theta_{\text{missing}}|$ distributions are dominated by the forward ISR photons, and depending on the energies of the forward ISR photons. According to their mass threshold, i.e. $\mathrm{M_H}+\mathrm{M_Z}$ for Higgs-strahlung, $2\mathrm{M_Z}$ for $eeff$ and $\mu\mu ff$ through ZZ intermediate state, and minor or no mass threshold for the rest of them, their $|\cos\theta_{\text{missing}}|$ distributions are more and more maximized at one in the sequence, as can be seen in Figure 6.16.

Furthermore, the energy or momentum resolutions of the detector may also affect the $|\cos\theta_{\text{missing}}|$ distribution, since the $|\cos\theta_{\text{missing}}|$ is calculated from the momenta of the final states measured by the detector. For different particles, the energy or momentum resolution may be different, i.e. the (hadronic) jet energy resolution could be one to two orders of magnitude worse than that of the (lepton) track momentum. However, this

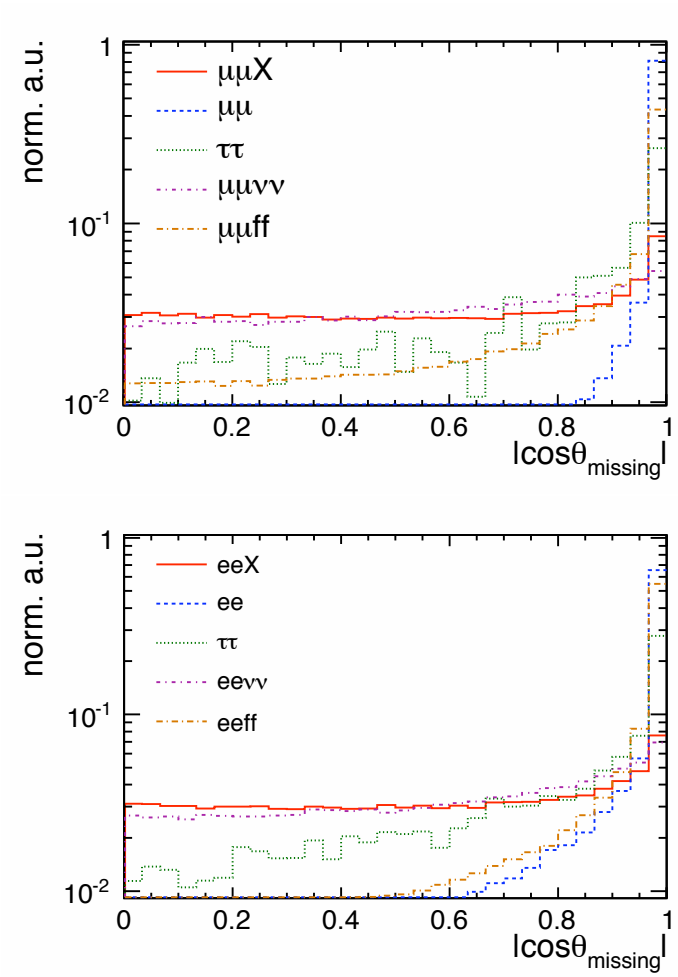

Figure 6.16: $|\cos\theta_{\text{missing}}|$ distributions of $\mu\mu X$ (top) and eeX (bottom), and of their corresponding backgrounds.

is assumed to be only a minor effect compared to the two major effects just discussed before.

6.4.2 Cut-Based Rejection

As mentioned before, two parallel analyses are performed. One is *Model Independent (MI) Analysis*, which is the general case, where no assumption on the Higgs decay mode is made. The second one is named *Model Dependent (MD) Analysis*, where the characteristics of Higgs decay are employed.

Based on the studies in Section 6.4.1, the cuts for MI and MD analyses selected and given in Table 6.6. These will be referred as *MI Cut-Chain* and *MD Cut-Chain* in the following. The cuts are applied sequentially in the same order as listed.

Reminding that in the production of ee and $\mu\mu$ processes, the Pre-Cuts (Table 6.3)

MI Cut-Chain
(1) Tightened Pre-cuts
(2) $P_{Tdl} > 20\,GeV$
(3) $M_{dl} \in (80,\ 100)\,GeV$
(4) $acop \in (0.2,\ 3.0)$
(5) $\Delta P_{Tbal.} > 10\,GeV$
(6) $\lvert\Delta\theta_{2tk}\rvert > 0.01$
(7) $\lvert cos\theta_{missing}\rvert < 0.99$
(8) $M_{recoil} \in (115,\ 150)\,GeV$
(9) Likelihood Further Rejection

MD Cut-Chain
(1) Tightened Pre-cuts
(2) $N_{add.TK} > 1$
(3) $\Delta\theta_{2tk} > 0.01$
(4) $\Delta\theta_{min} > 0.01$
(5) $acop \in (0.2, 3.0)$
(6) $\lvert cos\theta_{missing}\rvert < 0.99$
(7) $M_{recoil} \in (115, 150)\,GeV$
(8) Likelihood Further Rejection

Table 6.6: Model Independent (MI) and Model Dependent (MD) Cut-Chain. The *Tightened Pre-Cuts* are listed in Table 6.7, and the Likelihood further rejection is introduced in Section 6.4.3.

eeX channel	$\mu\mu X$ channel
$\lvert cos\theta_{e^+/e^-}\rvert < 0.95$	$\lvert cos\theta_{\mu^+/\mu^-}\rvert < 0.99$
$M_{e^+e^-} \in (75, 110)\ GeV$	$M_{\mu^+\mu^-} \in (75, 110)\ GeV$
$P_{Te^+e^-} > 15\ GeV$	$P_{T\mu^+\mu^-} > 15\ GeV$
$M_{recoil} \in (110, 160)\ GeV$	$M_{recoil} \in (110, 160)\ GeV$

Table 6.7: Tightened Pre-Cuts for all the reactions.

are applied in order to reduce the simulation time. This treatment may have a potential underestimation of the migration effect. The migration effect can be illustrated by the M_{recoil} distribution of the *ee* process. After detector simulation, some events that were outside the M_{recoil} window (i.e. 115 to 150 GeV) in the event generation, are migrated into this window, due to the Bremsstrahlung and uncertainties of the detector measurement. To compensate this effect, the Pre-Cuts applied in the event generation should be sufficiently loose. After detector simulation, they should be replaced by a set of more tightened cuts, which should also be applied to the other processes. The Tightened Pre-Cuts are listed in Table 6.7 and will be referred as *Tightened Pre-Cuts* in the following.

Ana.	Pol.	Ch.	S (%)	B
MI	$e^-_R e^+_L$	$\mu\mu X$	1367 (69.46%)	2124
		eeX	1033 (49.04%)	3658
	$e^-_L e^+_R$	$\mu\mu X$	2028 (69.48%)	6388
		eeX	1539 (49.04%)	8776
MD	$e^-_R e^+_L$	$\mu\mu X$	1453 (73.85%)	1813
		eeX	1161 (55.10%)	3953
	$e^-_L e^+_R$	$\mu\mu X$	2154 (73.81%)	2846
		eeX	1731 (55.16%)	4877

Table 6.8: Resulting number of signal (S) and background (B), and the efficiency of signal selection (in the parentheses) after *Cut-Based* background rejection.

The number of signal and background remaining after each cuts are given in tables in Appendix B, for all the eight analysis channels, i.e, for $\mu\mu X$ and eeX channels with $e^-_L e^+_R$ and $e^-_R e^+_L$ polarization modes in MI and MD analyses. From these tables one can examine the efficiencies of the background rejection variables.

Table 6.8 summarized the number of signal and background, and the selection efficiency after the Cut-Based rejection. On average, the MD Cut-Chain gives about 5% higher efficiencies on the signal selection and better backgrounds suppressions, than that of the MI Cut-Chain. However, in both cases, the number of background remaining is larger than expected. A Likelihood based rejection is applied afterwards to suppress these background events further.

6.4.3 Likelihood Further Rejection

With the cut-based rejection, certain background events are found to be irreducible without crucial loss of the signal. Therefore, the Likelihood method is introduced, to provide the functionality to combine several variables and calculate an estimator, which gives a further separation of the signal and background.

The Likelihood of one event to be a particular reaction R is defined as:

$$\mathcal{L}_R = \prod P^i_R \ , \tag{6.11}$$

where, P^i_R is the probability of this event given by the Probability Density Function (PDF) of the ith variable of the reaction R.

According to Equation 6.11, the Likelihood gives the *likeliness* of one event to be of reaction R, the greater the $\mathcal{L}_R$ the more likely the event to be of reaction R. Replacing the reaction R by the signal or the background, the Likelihood of one event to be the signal ($\mathcal{L}_S$), and the Likelihood of one event to be the jth background ($\mathcal{L}_{Bj}$) can be defined as:

$$\begin{aligned} \mathcal{L}_S &= \prod P^i_S \ , \\ \mathcal{L}_{Bj} &= \prod P^i_{Bj} \ . \end{aligned} \tag{6.12}$$

Hereafter, the *Likelihood Fraction*, f_L, is defined as

$$f_L = \frac{\mathcal{L}_S}{\mathcal{L}_S + \sum \mathcal{L}_{Bj}} \ , \tag{6.13}$$

where, f_L is within (0,1). Based on this definition, the closer is the f_L to *one*, the more likely the event to be the signal; the closer is the f_L to *zero*, the more likely the event to be the background. A cut on f_L to be greater than some value can, therefore, perform a selection of the signal or a suppression of the background.

In practice, the PDF of a particular variable of a particular process is given by its normalized differential distribution. In the context of this analysis, the variables employed are,

$$\mathrm{P_{Tdl}},\ \cos\theta_{\mathrm{dl}},\ acol,\ \text{and}\ \mathrm{M_{dl}}.$$

Thus, the ith variable in Equation 6.12 refers to one of these four variables, with their PDFs given in Figures 6.4, 6.5, 6.6 and 6.8 in Section 6.4.1, respectively.

After the cut-based background rejection, some backgrounds are already completely suppressed. As shown in the tables in Appendix B, the remaining backgrounds are mainly $eeff/\mu\mu ff$ processes for the MD analysis, while $eeff/\mu\mu ff$, $ee\nu\nu/\mu\mu\nu\nu$ and $ee/\mu\mu$ for the MI analysis. Therefore, only PDFs of these backgrounds are employed in the calculation of the Likelihoods, as listed in Table 6.9 for different analysis channels.

Ana. Mode	Ana. Channel	Backgrounds (Bj)
MI	$\mu\mu X$	$\mu\mu$, $\mu\mu\nu\nu$, $\mu\mu ff$
	eeX	ee, $ee\nu\nu$, $eeff$
MD	$\mu\mu X$	$\mu\mu ff$
	eeX	$eeff$

Table 6.9: The background processes of which the PDFs are employed in the Likelihood calculation, for different analysis channels.

The cut on f_L is then optimized according to the maximum of the significance $S/\sqrt{S+B}$, where S and B refer to the number of remaining events of signal and background, respectively. The optimization procedure to determine the f_L cut is performed for all the eight analysis channels separately, i.e., for $\mu\mu X$ and eeX channels with $\mathrm{e_L^- e_R^+}$ and $\mathrm{e_R^- e_L^+}$ polarization modes in the MI and MD analyses.

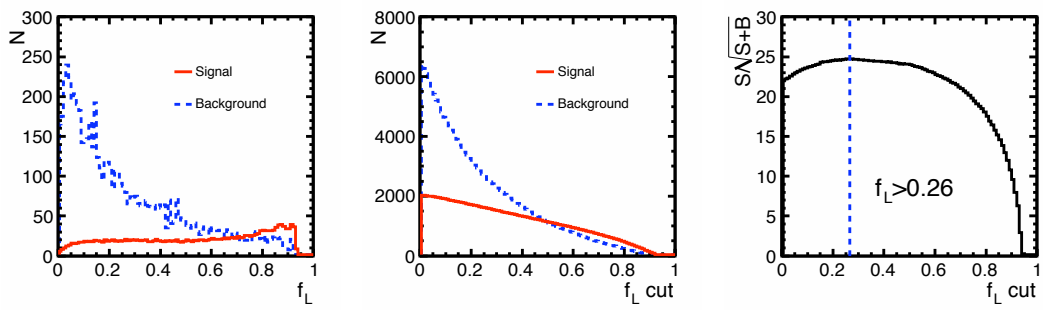

Figure 6.17: The distributions of the Likelihood Fraction f_L (left), the number of remaining events versus the cut on f_L (middle), and the significance versus f_L cuts (right). The distributions are shown for the $\mu\mu X$-channel with polarization mode $\mathrm{e_L^- e_R^+}$ in the MI Analysis.

Figure 6.17 shows an example of the optimization procedure, for the $\mu\mu X$-channel with polarization mode $\mathrm{e_L^- e_R^+}$ in the MI Analysis. In this figure, the left plot gives

the distributions of f_L of signal and background; the middle plot shows the number of events remaining as a function of the cut on f_L for signal and background; and the one on the right is the significance versus the f_L cuts, where the maximum on the significance is marked and the optimized f_L cut value is labeled. The figures for all the other analysis channels are given in Appendix A.

The number of events remaining after the Likelihood rejection for signal and various backgrounds for all eight analysis channels are listed in the tables in Appendix B. With the Likelihood rejection, all the backgrounds are further suppressed by about a factor of two, while the loss of the signal is at most 12%.

The number of signal and total number of background remaining, together with the final signal selection efficiency of all eight analysis channels are summarized in Table 6.10.

Ana.	Pol.	Ch.	S (%)	B
MI	$e^-_R e^+_L$	$\mu\mu X$	1165 (59.20%)	1023
		eeX	909 (43.14%)	1991
	$e^-_L e^+_R$	$\mu\mu X$	1596 (54.68%)	2563
		eeX	1153 (36.74%)	3508
MD	$e^-_R e^+_L$	$\mu\mu X$	1289 (65.53%)	883
		eeX	889 (42.20%)	1139
	$e^-_L e^+_R$	$\mu\mu X$	1911 (65.49%)	1397
		eeX	1378 (43.90%)	1679

Table 6.10: The final number of signal (S) and number of background (B) after background rejection, and the corresponding efficiencies of signal selection (in the parentheses).

6.5 Fit Methods

In the previous section, the methods to select the signal and to suppress the background have been studied and applied. The resulting number of signal and background are summarized in Table 6.10. The remaining spectrum is a superimposition of signal and background events.

The next analysis step is to extract the Higgs mass ($\mathrm{M_H}$) and the total Higgs-strahlung cross section (σ) from the remaining spectrum, where the cross section is determined by the number of signal events (N_S) as given by Equation 2.36.

For this purpose, a composed model $F_M(x)$ can be constructed, with at least two parameters, $\mathrm{M_H}$ and N_S. These two parameters together with their statistical errors can be determined by fitting the $F_M(x)$ to the remaining spectrum of signal plus background. The composed model can be constructed as

$$F_M(x;\ \mathrm{M_H}, N_S) = N_S \cdot F_S(x;\ \mathrm{M_H}) + N_B \cdot F_B(x)\ , \tag{6.14}$$

where, N_S and N_B are the number of events of signal and background, respectively, $F_S(x;\ \mathrm{M_H})$ and $F_B(x)$ are the functions describing the spectra of signal and background, respectively.

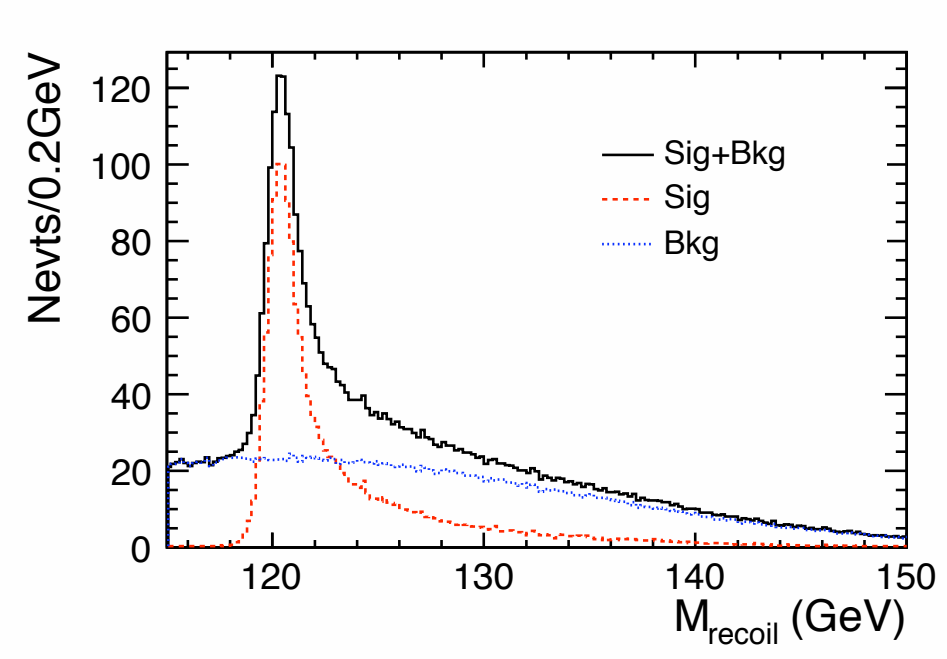

Figure 6.18: Recoil mass distributions after background rejection, of signal, background, and signal plus background. Illustration using MI analysis, $\mu\mu X$ channel with polarization mode $\mathrm{e^-_L e^+_R}$.

The next step is to construct the two functions, $F_S(x;\ \mathrm{M_H})$ and $F_B(x)$. Figure 6.18 shows the typical distributions of signal, background and signal plus background.

For the background distribution, since it is comparably flat, the choices of the $F_B(x)$ can be a Polynomial function or a broad Gaussian function. In the later on analysis, the $F_B(x)$ for a particular analysis channel is chosen to be one of the two functions depending on which one could give a better description.

As discussed in Section 2.6.2, the signal distribution has a maximum, which can be interpreted as the Higgs mass, and a long tail to the higher value. It is a convolution of smearing effects and radiative effects as shown in Equation 2.37. In the following sections, three choices of the $F_S(x)$ are studied.

The maximum of the signal in Figure 6.18 is not exactly at 120 GeV, but several hundreds MeV greater than 120 GeV. This is a pure mathematical effect. In a convolution of a symmetrical smearing function (e.g., a Gaussian function) with an asymmetrical radiative function (e.g., an Exponential function), the maximum will be shifted. Later on, this effect is referred as *Convolution Effect*.

6.5.1 GPET Function

GPET refers to Gaussian Peak Exponential Tail. It is a constructed partial function using a Gaussian core to describe the maximum and an Exponential function to supplement the tail, with its original formula applied in earlier studies[17, 18, 19]. The original function is hereafter modified, such that the function itself and its first derivative are continuous. After modification, the GPET function is defined as

$$F_S(x;\ \mathrm{M_H}) = \begin{cases} G(x;\ s+\mathrm{M_H},\sigma) & : \frac{x-s-\mathrm{M_H}}{\sigma} \leq k \\ \beta \cdot G(x;\ s+\mathrm{M_H},\sigma) + (1-\beta)\cdot e^{\frac{k^2}{2}} \cdot e^{-(x-s-\mathrm{M_H})\frac{k}{\sigma}} & : \frac{x-s-\mathrm{M_H}}{\sigma} > k \end{cases}, \tag{6.15}$$

where, $G(x;\ \mu,\sigma)$ is a Gaussian function with mean μ, and variance σ^2. The first part of Equation 6.15 is a pure Gaussian and the second part is a sum of the Gaussian and an Exponential with relative fractions β and $1-\beta$, respectively, where $\beta \in (0,1)$. The factor k defines the transition point between the two parts. By requiring that the $k > 0$, the transition point is greater than the Gaussian mean $s + \mathrm{M_H}$, which ensures the pure Gaussian part covers the maximum of the distribution. The term $e^{\frac{k^2}{2}}$, which multiplied with the Exponential, is introduced to keep the partial function continuous in both itself and its first derivative. The parameter s in the Gaussian mean accounts for the Convolution Effect mentioned before.

Figure 6.19 shows a typical fit to the pure signal using the GPET function, which describes very well the recoil mass maximum. However, at around 121 to 123 GeV, the GPET function is apparently lower than the histogram. This is due to the fact that the background rejection distorts the signal distribution, especially largely suppressed the tail, as shown in Figure 6.20. This suppression makes the description of the tail using Exponential function no more perfect. At the same time, the fitting procedure

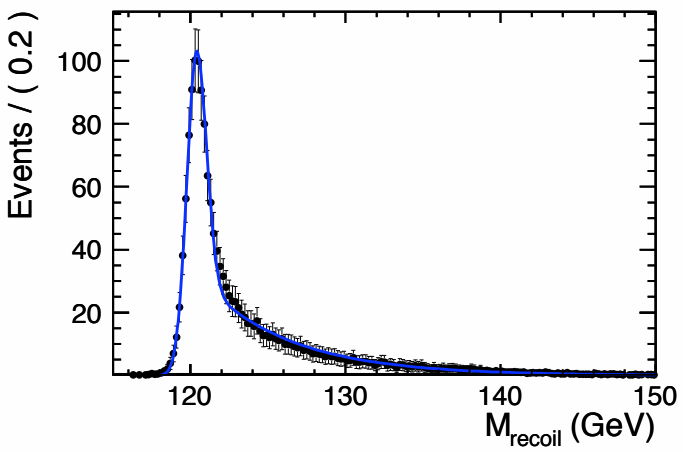

Figure 6.19: Fit to pure signal *after background rejection* using GPET formula. Illustration using MI analysis, $\mu\mu X$ channel with polarization mode $\mathrm{e^-_L e^+_R}$.

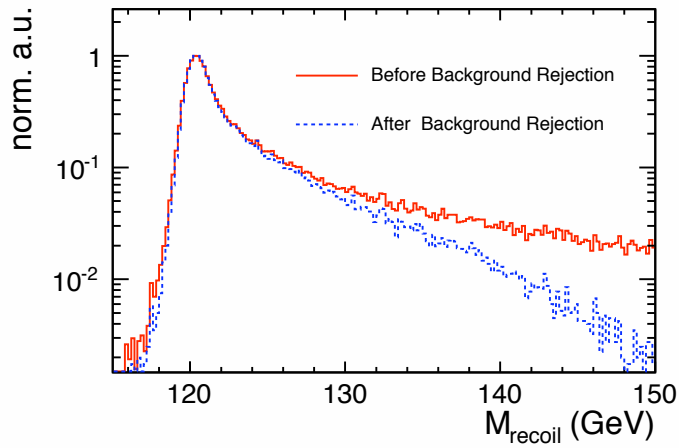

Figure 6.20: M_{recoil} distribution of Signal *before and after background rejection*. Maximum of the distributions are normalized to be *one*. Illustration using MI analysis, $\mu\mu X$ channel with polarization mode $e^-_L e^+_R$.

is inclined to have a better description of a wider range, i.e., the tail from 123 to 150 GeV, instead of a narrower range, i.e., the region from 121 to 123 GeV. Thus, a better description of the largely suppresses the tail, results a worse description of the region from 121 to 123 GeV. This effect is referred as the *Background Rejection Effect* in the following.

The Background Rejection Effect can be considered by summing an additional Gaussian at around 121 to 123 GeV to complement the spectrum, as given by

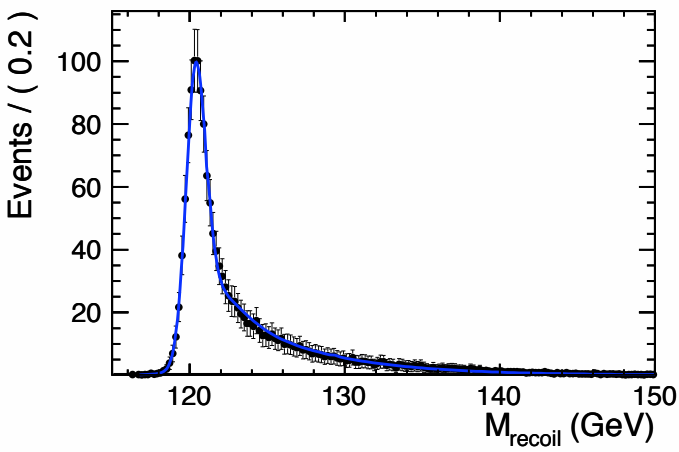

Figure 6.21: Fit to pure signal *after background rejection* using *Corrected GPET formula*. Illustration using MI analysis, $\mu\mu X$ channel with polarization mode $e^-_L e^+_R$.

$$F'_S(x;\ \mathrm{M_H}) = N_1 G(x; \mu_1, \sigma_1) + F_S(x) \tag{6.16}$$

where, $G(x;\ \mu_1, \sigma_1)$ is the complementary Gaussian, with a normalization N_1, a mean μ_1 and a variance σ_1^2. The μ_1 is around 122 GeV, the σ_1 is between 1 to 3 GeV, together with the N_1, they have to be determined in the fit.

The fit using the corrected GPET function given in Equation 6.16 is shown in Figure 6.21. Comparing with the one before (Figure 6.21), the corrected GPET function provides a much better description of the region from 121 to 123 GeV while keeping the same good description of the long tail.

Figure 6.22 shows the fit to the spectrum of signal plus background using the composed model $F_M(x)$ with the GPET function to describe the signal, for $\mu\mu X$ and eeX channels with polarization mode $\mathrm{e_L^- e_R^+}$ in the MD analysis. The statistical errors on the Higgs mass measurement are 31 MeV from $\mu\mu X$-channel and 64 MeV from eeX-channel, while that on the cross section measurement are 2.75% from $\mu\mu X$-channel and

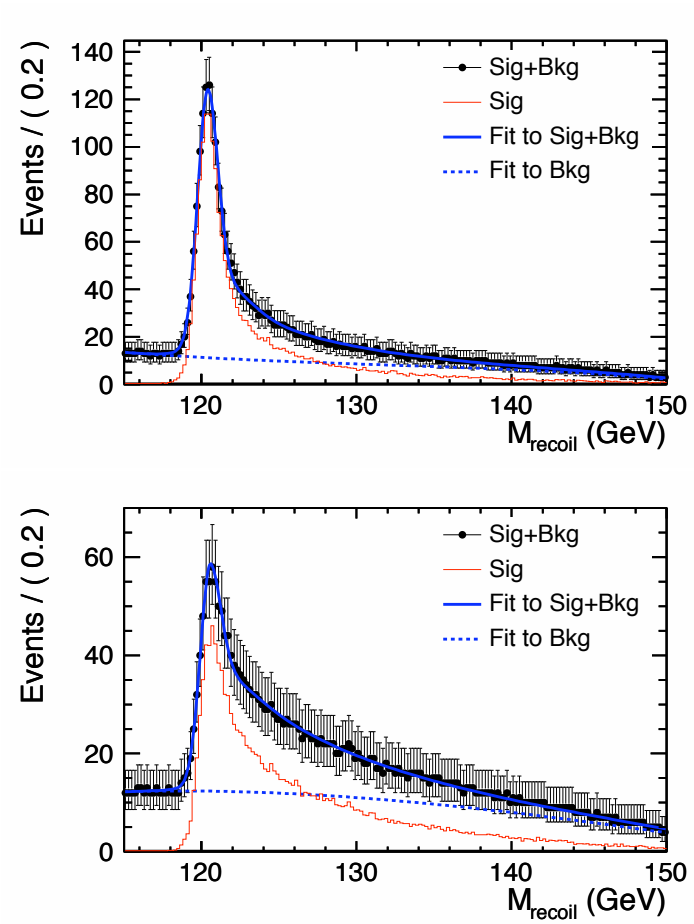

Figure 6.22: Fit to the signal plus background using *GPET Function* of $\mu\mu X$ (top) and eeX (bottom) channels with polarization mode $\mathrm{e_L^- e_R^+}$ in MD analysis.

3.59% from eeX-channel. The fit plots of all the other analysis channels are shown in Appendix D, and the results are given in Section 6.6.

6.5.2 Kernel Estimation

This is an application[2] of the Kernel Estimation[45], which is extensively used in the Higgs searches at LEP[46, 47]. The Kernel Estimation is an universal method, through which, an analytical function can be derived to describe any distribution. However, there is no physical significance included in the function.

The Kernel Estimation provides an unbinned and non-parametric estimate of the probability density function from which a set of data is draw. The *Adaptive Kernel Estimation*[45] of the parent distribution is given by

$$f(x) = \frac{1}{N}\sum_{i=1}^{N}\frac{1}{h_i}K\left(\frac{x-t_i}{h_i}\right), \tag{6.17}$$

with

$$h_i = (\frac{4}{3})^{1/5}\ N^{-1/5}\sqrt{\frac{\sigma_i}{f_0(t_i)}}\ , \tag{6.18}$$

where, $\{t_i\}$ represents the unbinned data totally N events, the h_i is the smoothing parameter (also called the *bandwidth*) of the *ith* event, the σ_i is the local standard deviation of the *ith* event, and the $f_0(x)$ is the parent distribution. The function $K(x)$ is the *Kernel Function* to spread out the contribution of each data point in the estimate of the parent distribution. An obvious and natural choice of $K(x)$ is a Gaussian with $\mu = 0$ and $\sigma = 1$:

$$K(x) = G(x;\ 0,1) = \frac{1}{\sqrt{2\pi}}e^{-x^2/2}. \tag{6.19}$$

However, the application of the original Adaptive Kernel Estimation, although possible but not simple. First of all, to initialize the function using unbinned data implies that the number of "parameters" involved is enormous, i.e., at least two times the number of events N. Second, the parent distribution $f_0(x)$ and the local standard deviation are unknown, which involves additional works, i.e., to estimate the parent distribution using the *Fixed Kernel Estimation*[45] .

Due to the reasons above, a simplification of the original Adaptive Kernel Estimation is performed. The *Simplified Kernel Estimation using Gaussian Kernel* is given by

[2]The application study of the Kernel Estimation is inspired by a sum of four Gaussian kernels[48] to describe the Higgs recoil mass spectrum, which is eventually used to produce the results presented in the ILD Letter of Intent.

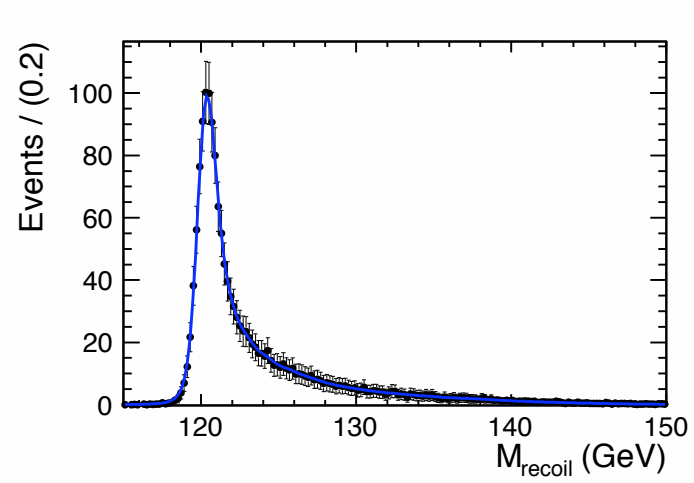

Figure 6.23: Fit to pure signal *after background rejection* using *Kernel Estimation*. Illustration using MI analysis, $\mu\mu X$ channel with polarization mode $e^-_L e^+_R$.

$$F_S(x) = \frac{1}{N}\sum_{j=1}^{m} n_j G(x; t_j, h_j), \tag{6.20}$$

with

$$h_j = (\frac{4}{3})^{1/5}\ N^{-1/5}\Delta x\sqrt{\frac{N}{n_j}}\ , \tag{6.21}$$

which can be initialized using binned data, i.e., a histogram. In Equation 6.20, the j refers to the bin number with totally m bins, t_j is the center of the jth bin, n_j is the bin content, and the h_j gives the bandwidth of the jth bin. In determining the h_j, the local standard deviation σ_i in Equation 6.18 is chosen to be the bin width Δx, and the parent distribution at $f(t_j)$ is given by $n_j/(N\Delta x)$.

However, Equation 6.20 contains no parameter $\mathrm{M_H}$. If assuming the shape of the distribution does not change when the $\mathrm{M_H}$ changes a small value along the x axis, the $\mathrm{M_H}$ can be added into the equation as a linear shift:

$$F_S(x;\ \mathrm{M_H}) = \frac{1}{N}\sum_{j=1}^{m} n_j G(x - \mathrm{M_H}; t_j, h_j), \tag{6.22}$$

where, the x is replaced by $x - \mathrm{M_H}$.

In practice, to determine the Higgs mass, one may

(1) Initialize the function using the recoil mass histogram of a given Higgs mass, i.e., $\mathrm{M_H} = 120\mathrm{GeV}$;

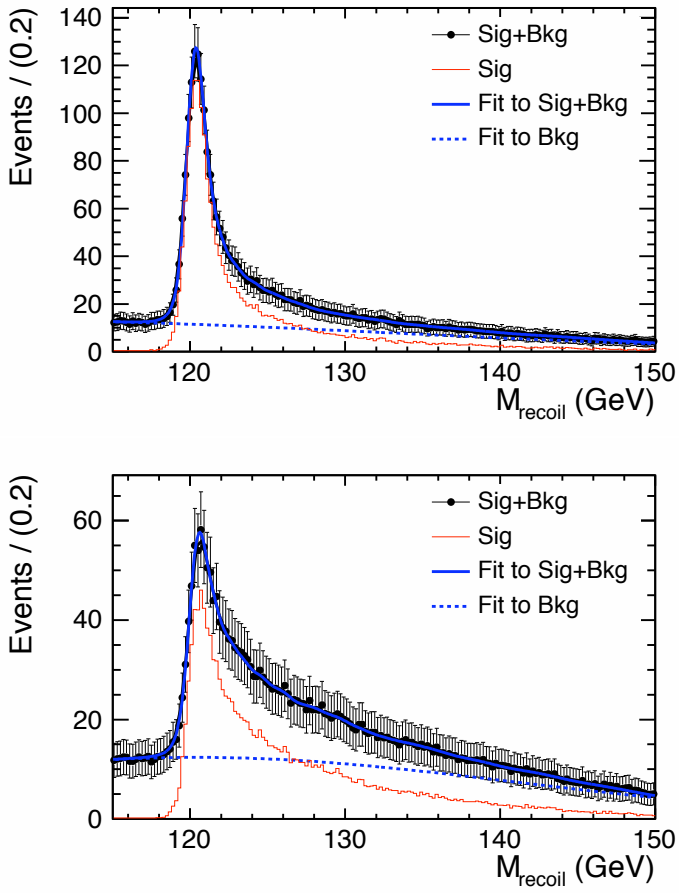

Figure 6.24: Fit to the signal plus background using *Kernel Estimation* of $\mu\mu X$ (top) and eeX (bottom) channels of polarization mode $e^-_L e^+_R$, in MD analysis.

(2) Release the parameter M_H and normalization and fix all the other parameters;

(3) Add it to the composed model $F_M(x)$ and fit to the signal plus background.

Figure 6.23 gives a typical fit to the pure signal using the Kernel Estimation. And, Figure 6.24 shows the fit to the spectrum of signal plus background using the composed model $F_M(x)$ with the Kernel Estimation to describe the signal, for $\mu\mu X$ and eeX channels with polarization mode $e^-_L e^+_R$ in the MD analysis. The statistical errors on the Higgs mass measurement are 31 MeV from $\mu\mu X$-channel and 65 MeV from eeX-channel, while that on the cross section measurement are 2.74% from $\mu\mu X$-channel and 3.66% from eeX-channel. The fit plots of all the other analysis channels are shown in Appendix D, and the results are given in Section 6.6.

6.5.3 Physics Motivated Function

The last function to be introduced for the signal distribution is a physical motivated one[3] . It is derived starting from the Beamstrahlung approximation formula developed by Yokoya and Chen[49, 50, 51, 52], convoluted analytically with the ISR approximation[53], and then numerically convoluted with Gaussian function. This dissertation gives the first development of the Physics Motivated function, and the detailed derivation is given in Appendix C.

The Physics Motivated Function is given by:

$$F_S(x) = f_2(y(x)) \cdot \left|\frac{dy}{dx}\right| \tag{6.23}$$

where,

$$\begin{aligned} y(x) = \frac{1}{2s^2} \cdot \Big[& 2s(x^2 - \mathrm{M_H}^2) + (s + x^2 - \mathrm{M_Z}^2)(s - x^2 + \mathrm{M_Z}^2) - \\ & (s - x^2 + \mathrm{M_Z}^2) \cdot \sqrt{4s(\mathrm{M_H}^2 - \mathrm{M_Z}^2) + (s - x^2 + \mathrm{M_Z}^2)^2} \Big] \ , \end{aligned} \tag{6.24}$$

$$\frac{dy}{dx} = \frac{x}{s^2} \cdot \frac{\left[s - x^2 + \mathrm{M_Z}^2 + \sqrt{4s(\mathrm{M_H}^2 - \mathrm{M_Z}^2) + (s - M^2 + \mathrm{M_Z}^2)^2} \right]^2}{\sqrt{4s(\mathrm{M_H}^2 - \mathrm{M_Z}^2) + (s - x^2 + \mathrm{M_Z}^2)^2}} \ ; \tag{6.25}$$

and,

$$f_2(y) = \sum_{i=0}^{N} p(i) \cdot [g_1(y; i) \otimes G(y; 0, \sigma)] \ , \tag{6.26}$$

with

$$p(i) = \frac{2^i}{i!} \left(\frac{n_\gamma}{2} \right)^i e^{-n_\gamma} \ , \tag{6.27}$$

$$g_1(y; i) = \kappa^{\frac{i}{3}} \cdot y^{(\frac{i}{3}+\beta-1)} \cdot \frac{\Gamma(1+\beta)}{\Gamma(\frac{i}{3}+\beta)} \cdot \ {}_1F_1(\frac{i}{3}, \frac{i}{3} + \beta, -\kappa y) \ . \tag{6.28}$$

In these formulae, ${}_1F_1(a, b, z)$ is the *Confluent Hypergeometric Function*; $\sqrt{\mathrm{s}}$ is centre-of-mass energy; $\mathrm{M_H}$ and $\mathrm{M_Z}$ are the masses of Higgs and Z^0, respectively; y is the fraction of energy loss being a fraction of the beam energy; the $G(y;\ 0, \sigma)$ is a Gaussian

[3]The development of the Physics Motivated Function is inspired and supported by[54].

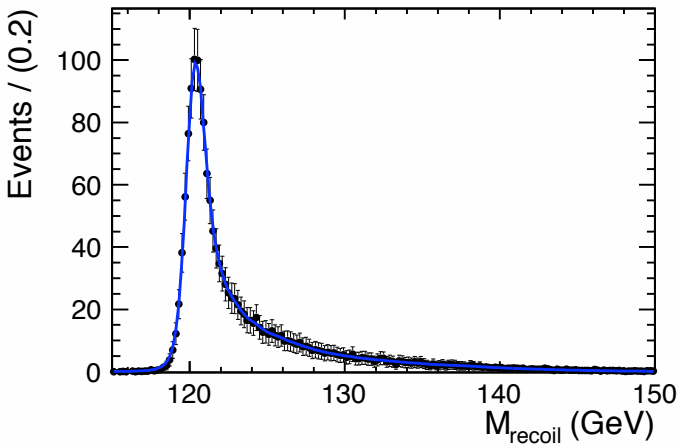

Figure 6.25: Fit to pure signal *after background rejection* using *Corrected Physics Motivated Function*. Illustration using MI analysis, $\mu\mu X$ channel with polarization mode $e^-_L e^+_R$.

function to account for all the smearing effects, with σ defined as a fraction of the beam energy; n_γ is the average number of Beamstrahlung photons; κ is a Beamstrahlung parameter. The last two parameters can be found in Table 3.2. And β comes from the ISR approximation given by

$$\beta = \frac{2\alpha}{\pi}[log(\frac{s}{m_e^2}) - 1] = 0.117 \tag{6.29}$$

for $\sqrt{s} = 250$ GeV.

In Equation 6.26, the $p(i)$ gives the probability for the radiation of i Beamstrahlung photons, which is given by the Poisson statistics taken both beams into account; the $g_1(y;\ i)$ is the normalized y distribution in case of i photons radiation. The $p(i)$ and $g_1(y;\ i)$ are given in Equation 6.27 and 6.28, respectively. In practice, i is limited to 4, since given the beam parameters in Table 3.2, the probability to have more than 4 Beamstrahlung photons is only about 0.2%, which is negligible.

This Physics Motivated Function considers the Beamstrahlung, ISR and the kinematics of Higgs-strahlung process, and the Gaussian smearing, i.e., the beam energy spread and the uncertainty of the detector response. Besides the Gaussian smearing, which is convoluted numerically, all the other effects are included analytically. It can provide a reasonable good approximation of the Higgs recoil mass distribution with all of the parameters known in advance as shown in the Figure C.1 in Appendix C.

However, one may noticed that the FSR and Bremsstrahlung effects are not included in the function. Furthermore, the *Background Rejection Effect* that distorted the signal distribution should also be considered. Therefore, for practical application, a correction is needed.

The correction is applied on $f_2(y)$ by multiplying an Polynomial function and an

Exponential function. Thus, Equation 6.26 becomes

$$f_3(y) = f_2(y) \cdot (1 + p_1 y + p_2 y^2 + p_3 y^3) \cdot e^{-p_0 y} \ . \tag{6.30}$$

And the *Physics Motivated Function* becomes

$$F'_S(x) = f_3(y(x)) \cdot \left| \frac{dy}{dx} \right| \tag{6.31}$$

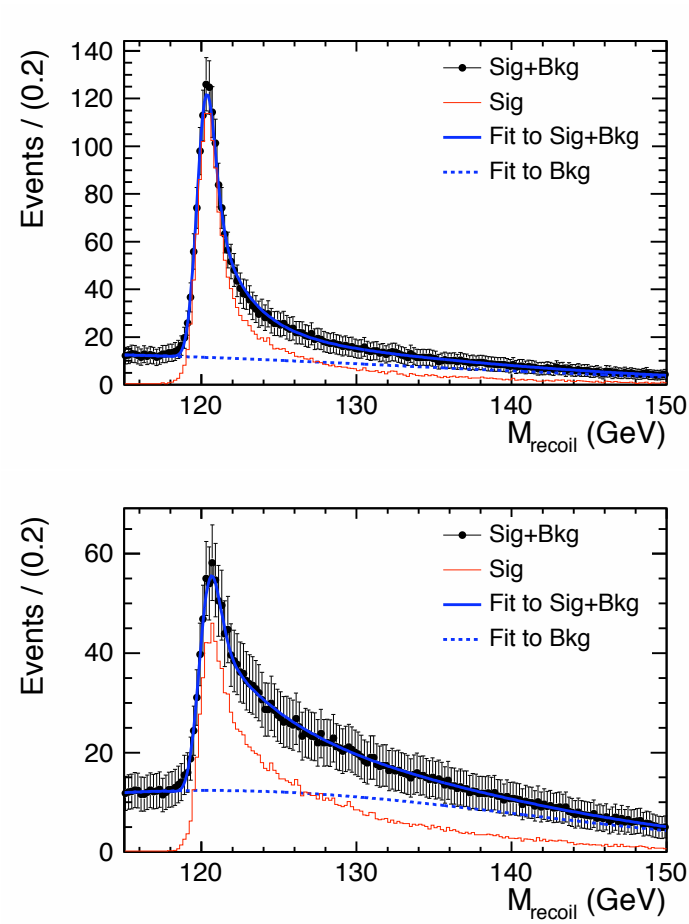

Figure 6.26: Fit to the signal plus background using *Physics Motivated Function* of $\mu\mu X$ (top) and eeX (bottom) channels of polarization mode $e^-_L e^+_R$, in MD analysis.

A typical fit to the pure signal using the *Corrected Physics Motivated Function* is shown in Figure 6.25. And, Figure 6.26 shows the fit to the spectrum of signal plus background using the composed model $F_M(x)$ with the Kernel Estimation to describe the signal, for $\mu\mu X$ and eeX channels with polarization mode $e^-_L e^+_R$ in the MD analysis. The statistical errors on the Higgs mass measurement are 31 MeV from $\mu\mu X$-channel and 66 MeV from eeX-channel, while that on the cross section measurement are 2.76%

from $\mu\mu X$-channel and 3.59% from eeX-channel. The fit plots of all the other analysis channels are shown in Appendix D, and the results are given in Section 6.6.

6.5.4 Comparison of the Three Methods

All these three methods can satisfactorily describe the Higgs recoil mass distribution, with a χ^2/Ndf around 1, while they have their own advantages and weaknesses.

In sense of stability and adaptiveness to the distribution, the Kernel Estimation is the best, because it is an universal method to estimate any distribution. No matter how different is the distribution due to different physics models or other effects, the Kernel Estimation can always provide the best estimation. However, both the GPET Function and the Physics Motivated Function do not have such a flexibility and stability as the Kernel Estimation. For instance, the possible ranges of most of the parameters should be specified in order to assure the fit is convergent. Indeed, to account for the *Background Rejection Effect*, which suppresses the tail of the distribution, some corrections are introduced as discussed before.

In sense of inspirations from physics, the Physics Motivated Function is the best, because all its parameters (excepts those in the correction) have their physical meaning. With the knowledges of these parameters, the distribution can be reasonably described without MC techniques.

In sense of the computing time of the fits, the GPET function is the best. To accomplish a full fitting procedure of an analysis channel, it takes several seconds using the GPET function, one or two minutes using the Kernel Estimation, while several hours using the Physics Motivated function.

6.6 Results

The results of Higgs mass and cross section measurements using *GPET Function*, *Kernel Estimation* and *Physics Motivated Function* are given separately in this section, for $\mu\mu X$ and eeX channels with $e^-_L e^+_R$ and $e^-_R e^+_L$ polarization modes in MI Analysis and MD Analysis. The results are reported assuming $\mathcal{L} = 250\text{fb}^{-1}$, together with the *merged* results combining the two leptonic channels.

Pol.	Ch.	M_H (GeV)	σ (fb)
$e^-_R e^+_L$ $\mathcal{L} = 250$ fb^{-1}	$\mu\mu X$	119.998 ±(0.040)	7.86 ± 0.28 (3.56 %)
	eeX	119.994 ±(0.093)	8.44 ± 0.43 (5.09 %)
	merged	119.997 ±(0.037)	8.03 ± 0.23 (2.92 %)
$e^-_L e^+_R$ $\mathcal{L} = 250$ fb^{-1}	$\mu\mu X$	119.995 ±(0.036)	11.67 ± 0.39 (3.34 %)
	eeX	119.981 ±(0.083)	12.52 ± 0.61 (4.87 %)
	merged	119.993 ±(0.033)	11.92 ± 0.33 (2.76 %)

Table 6.11: Resulting Higgs mass M_H and cross section σ of the *MI Analysis* using *GPET Function*.

Pol.	Ch.	M_H (GeV)	σ (fb)
$e^-_R e^+_L$ $\mathcal{L} = 250$ fb^{-1}	$\mu\mu X$	119.995 ± 0.036	7.84 ± 0.26 (3.32 %)
	eeX	120.004 ± 0.081	8.42 ± 0.38 (4.51 %)
	merged	119.996 ± 0.033	8.02 ± 0.21 (2.67 %)
$e^-_L e^+_R$ $\mathcal{L} = 250$ fb^{-1}	$\mu\mu X$	120.004 ± 0.031	11.64 ± 0.32 (2.75 %)
	eeX	119.997 ± 0.064	12.52 ± 0.45 (3.59 %)
	merged	120.003 ± 0.028	11.94 ± 0.26 (2.18 %)

Table 6.12: Resulting Higgs mass M_H and cross section σ of the *MD Analysis* using *GPET Function*.

Pol.	Ch.	M_H (GeV)	σ (fb)
$e^-_R e^+_L$ $\mathcal{L} = 250$ fb^{-1}	$\mu\mu X$	120.006 ±(0.039)	7.89 ± 0.28 (3.55 %)
	eeX	120.005 ±(0.092)	8.46 ± 0.43 (5.08 %)
	merged	120.006 ±(0.036)	8.06 ± 0.23 (2.91 %)
$e^-_L e^+_R$ $\mathcal{L} = 250$ fb^{-1}	$\mu\mu X$	120.008 ±(0.037)	11.70 ± 0.39 (3.33 %)
	eeX	119.998 ±(0.085)	12.61 ± 0.62 (4.92 %)
	merged	120.006 ±(0.034)	11.96 ± 0.33 (2.76 %)

Table 6.13: Resulting Higgs mass M_H and cross section σ of the *MI Analysis* using *Kernel Estimation*.

Pol.	Ch.	M_H (GeV)	σ (fb)
$e^-_R e^+_L$ $\mathcal{L} = 250$ fb^{-1}	$\mu\mu X$	120.008 ± 0.037	7.88 ± 0.26 (3.30 %)
	eeX	120.001 ± 0.081	8.46 ± 0.38 (4.49 %)
	merged	120.007 ± 0.034	8.06 ± 0.21 (2.66 %)
$e^-_L e^+_R$ $\mathcal{L} = 250$ fb^{-1}	$\mu\mu X$	120.009 ± 0.031	11.68 ± 0.32 (2.74 %)
	eeX	120.007 ± 0.065	12.58 ± 0.46 (3.66 %)
	merged	120.009 ± 0.028	11.97 ± 0.26 (2.19 %)

Table 6.14: Resulting Higgs mass M_H and cross section σ of the *MD Analysis* using *Kernel Estimation*.

Pol.	Ch.	M_H (GeV)	σ (fb)
$e^-_R e^+_L$ $\mathcal{L} = 250$ fb^{-1}	$\mu\mu X$	119.997 ±(0.040)	7.82 ± 0.28 (3.58 %)
	eeX	120.005 ±(0.093)	8.44 ± 0.43 (5.09 %)
	merged	119.998 ±(0.037)	8.00 ± 0.23 (2.93 %)
$e^-_L e^+_R$ $\mathcal{L} = 250$ fb^{-1}	$\mu\mu X$	120.001 ±(0.037)	11.63 ± 0.39 (3.35 %)
	eeX	120.001 ±(0.087)	12.60 ± 0.62 (4.92 %)
	merged	120.001 ±(0.034)	11.90 ± 0.33 (2.77 %)

Table 6.15: Resulting Higgs mass M_H and cross section σ of the *MI Analysis* using *Physics Motivated Function*.

Pol.	Ch.	M_H (GeV)	σ (fb)
$e^-_R e^+_L$	$\mu\mu X$	119.998 ± 0.038	7.82 ± 0.26 (3.32 %)
$\mathcal{L} = 250$ fb^{-1}	eeX	120.010 ± 0.082	8.42 ± 0.38 (4.51 %)
	merged	120.000 ± 0.034	8.01 ± 0.21 (2.68 %)
$e^-_L e^+_R$	$\mu\mu X$	120.000 ± 0.031	11.60 ± 0.32 (2.76 %)
$\mathcal{L} = 250$ fb^{-1}	eeX	120.012 ± 0.066	12.54 ± 0.45 (3.59 %)
	merged	120.002 ± 0.028	11.92 ± 0.26 (2.19 %)

Table 6.16: Resulting Higgs mass M_H and cross section σ of the *MD Analysis* using *Physics Motivated Function.*

6.7 Summary and Discussion

The tables of results in Section 6.6 show that, the best precision achieved is 31 MeV on the Higgs mass measurement and 2.75% on the cross section measurement, from the $\mu\mu X$-channel with polarization mode $e^-_L e^+_R$ in the MD analysis. However, the precisions obtained from the eeX-channel are worse by a factor of two for the Higgs mass, while a factor of 1.5 for the cross section, compared to that of the $\mu\mu X$-channel. This is due to the Bremsstrahlung and much larger background on the eeX-channel analysis. As a result, after the background rejection, the eeX-channel has about 2/3 of the efficiency and about 1.5 times the background of that of the $\mu\mu X$-channel, as given in Table 6.10. At the same time, it also has a much broader mass distribution, as shown in the figures in Appendix D.

The derived results from MD analysis are consistently more precise by about 10% on average. The small difference between the results confirms that the methods employed for the background rejection in the MI analysis are already very efficient.

The results with polarization mode $e^-_L e^+_R$ are better than that of the $e^-_R e^+_L$ by about 10% in the MI analysis and about 20% in the MD analysis. The reason is that, although the polarization mode $e^-_R e^+_L$ suppresses the WW background, the cross sections of the Higgs-strahlung process are smaller by about 20% compared to that of the polarization mode $e^-_L e^+_R$. At the same time, the methods developed are efficient enough for the suppression of the WW background. Hence the polarization mode $e^-_L e^+_R$ gives better results.

6.7.1 Accelerator Effects versus Detector Effects on the Results

As discussed in Section 2.6, the precision of the Higgs recoil mass can be influenced by effects of beam energy spread, uncertainty of detector response, Beamstrahlung, ISR, FSR and Bremsstrahlung. Among them, the beam energy spread and Beamstrahlung are originated from the accelerator, while the uncertainty of detector response and Bremsstrahlung are coming from the detector.

For the Higgs recoil mass measurement, the precision depends on the mass resolution, with major contributions from the beam energy spread and the uncertainty of detector response. The beam energy spread describes the uncertainty on the energy

of the incoming beams. It is imposed by accelerator components such as the initial linac, the damping rings or, in case of electron beams, by an undulator in the electron beam line. The relative beam energy spread for $\sqrt{s} = 250$ GeV are 0.28% for electron beams and 0.18% for positron beams, as given in Table 3.2. The uncertainty of detector response, in this measurement, is mainly the tracking momentum resolution, as given by Equation 3.1 for ILD.

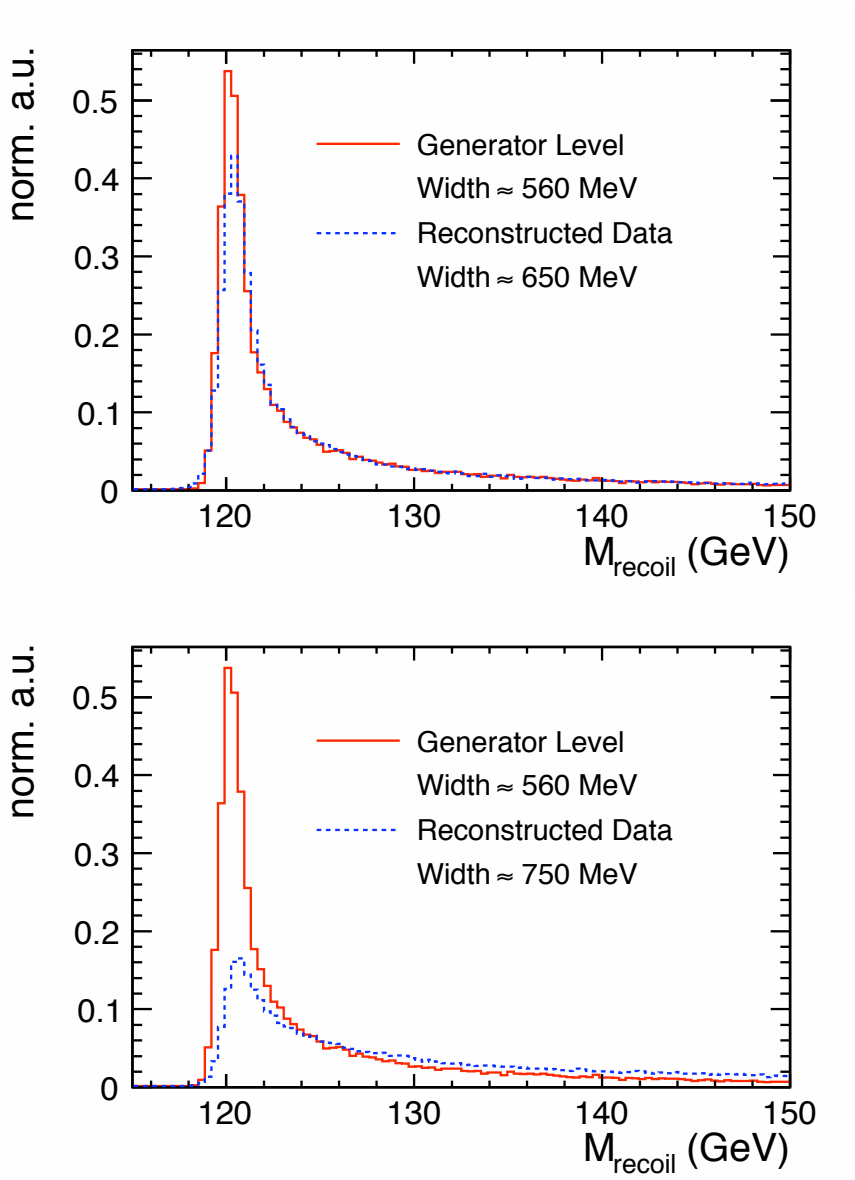

Figure 6.27: The Higgs recoil mass distribution in the $\mu\mu X$- channel (top) and eeX-channel (bottom), comparison of that in generator level and after detector simulation.

Figure 6.27 compares the Higgs recoil mass distribution in the generator level and after full detector simulation and reconstruction for $\mu\mu X$-channel (top) and eeX-channel

(bottom). The distribution in the generator level has the accelerator effects imposed, while that after reconstruction has the detector effects added.

For the recoil mass distributions of $\mu\mu X$-channel, a fit to the left side of the maximum using a Gaussian function gives the mass resolutions to be 560 MeV in the generator level, and 650 MeV after full detector simulation. The detector response leads to a broadening of the recoil mass maximum from 560 MeV to 650 MeV. The contribution from the uncertainty of detector response is therefore estimated to be 330 MeV. This observation indicates that *the dominant contribution to the observed width of the $\mu\mu X$ recoil mass distribution arises from the incoming beams rather than the response of the ILD detector.*

At the same time, a direct measurement of the detector contribution to the mass resolution can be performed by propagating the momentum error matrix to the recoil mass. The propagation function can be obtained by a direct differential of Equation 2.34 as

$$\Delta M_{dec} = \frac{1}{\mathrm{M_H}}\left\{[\sqrt{\mathrm{s}} - P_2(1 - cos(acol))]\Delta P_1 + [\sqrt{\mathrm{s}} - P_1(1 - cos(acol))]\Delta P_2\right\}, \quad (6.32)$$

where, *acol* is the acollinearity between the two leptons, P_1 and P_2 are the momenta of the two leptons, and ΔP_1 and ΔP_2 are the errors on the momenta of the two leptons propagated from their tracking error matrices.

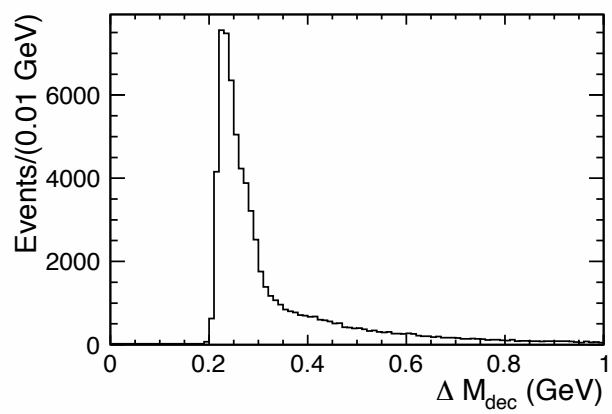

Figure 6.28: Distribution of Higgs recoil mass resolution *solely due to the uncertainty of detector response*, obtained by propagating the momenta matrices of lepton tracks to the recoil mass. Taking the $\mu\mu X$-channel for illustration, the maximum is at around 230 MeV, while the mean is about 330 MeV.

Figure 6.28 gives the resulting *distribution of the mass resolution solely due to the detector response*, using the $\mu\mu X$ Higgs-strahlung data. From the distribution, it can be obtained that the smallest mass resolution due to the detector response is about 230 MeV, while the *average* is about 330 MeV, which confirms the estimation above.

As mentioned in Section 2.6, the radiative effects Beamstrahlung and Bremsstrahlung increase the uncertainty for both the recoil mass and cross section measurements by migrating the signal events off the mass maximum, hence reducing the effective statistics for the measurements.

By comparing the distributions of the $\mu\mu X$-channel and that of the eeX-channel as shown in Figure 6.27, one realizes immediately that the Bremsstrahlung considerably destroys the effective statistics in eeX-channel. The height of maximum after full detector simulation is only 30% of that in the generator level. Together with the fact that eeX-channel suffers from larger background, for the Higgs mass measurement, the two times larger error obtained in the eeX-channel compared with the $\mu\mu X$-channel, can be understood.

6.7.2 Recovery of the Bremsstrahlung Photons

One possible strategy to compensate the loss of effective statistics due to the Bremsstrahlung radiation, is to identify the final state photons and include them into the recoil mass calculation.

Based on a dedicated algorithm[55] to identify the Bremsstrahlung photons, the four momenta of the selected electrons are combined with those of photons which have a small angular difference with the electrons. If these combined objects form a Z mass, they are included in the Z reconstruction.

Figure 6.29 compares the Higgs recoil mass distributions with and without Bremsstrahlung recovery. The inclusion of the Bremsstrahlung photons leads to a degradation of the mass resolution, since low energetic Bremsstrahlung photons are measured by the SiW ECAL. However, this drawback is counterbalanced by the gain in statistics.

With Bremsstrahlung recovery, the resulting number of signal, number of back-

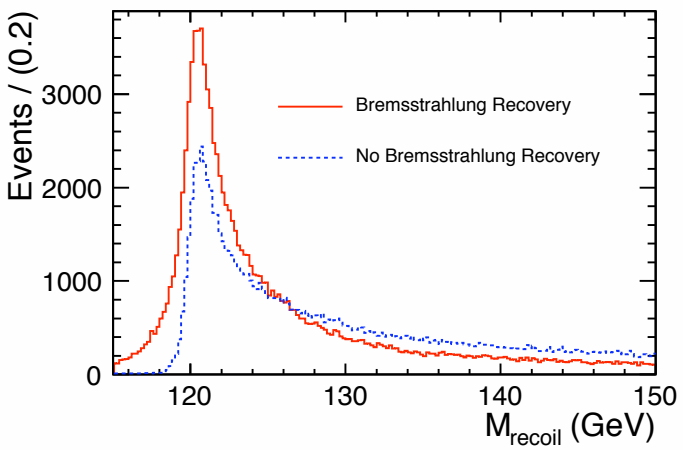

Figure 6.29: Comparison of the Higgs recoil mass distributions of eeX channel with and without the Bremsstrahlung recovery.

Ana.	Pol.	Ch.	S (%)	B
MI	$e_R^- e_L^+$	eeX	1029 (48.84%)	1408
	$e_L^- e_R^+$	eeX	1491 (41.51%)	3394
MD	$e_R^- e_L^+$	eeX	1152 (54.66%)	1114
	$e_L^- e_R^+$	eeX	1724 (54.94%)	1513

Table 6.17: Resulting Number of Signal (S) and Number of Background (B), and the efficiencies of signal selection (in the parentheses) after background rejection, for eeX-channel with Bremsstrahlung recovery

Ana.	Pol.	M_H (GeV)	σ (fb)
MI	$e_R^- e_L^+$	120.003 ± 0.081	8.41 ± 0.36 (4.28 %)
	$e_L^- e_R^+$	119.997 ± 0.073	12.52 ± 0.49 (3.91 %)
MD	$e_R^- e_L^+$	119.999 ± 0.074	8.41 ± 0.31 (3.69 %)
	$e_L^- e_R^+$	120.001 ± 0.060	12.51 ± 0.38 (3.04 %)

Table 6.18: Resulting Higgs mass M_H and cross section σ for the MI Analysis and MD Analysis in the eeX-channel with Bremsstrahlung recovery.

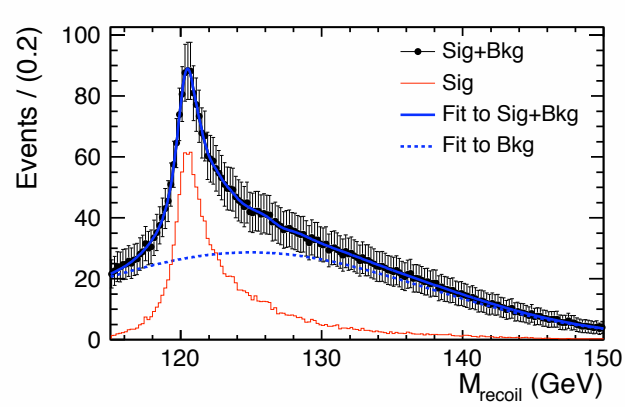

Figure 6.30: Fit to the signal plus background using *Kernel Estimation* for eeX-channel with polarization mode $e_L^- e_R^+$ in MI analysis, with Bremsstrahlung recovery.

Ana.	Pol.	M_H (GeV)	σ (fb)
MI	$e_R^- e_L^+$	120.005 ± 0.035	8.09 ± 0.22 (2.73 %)
	$e_L^- e_R^+$	120.006 ± 0.033	12.02 ± 0.31 (2.54 %)
MD	$e_R^- e_L^+$	120.006 ± 0.033	8.10 ± 0.20 (2.46 %)
	$e_L^- e_R^+$	120.007 ± 0.028	12.02 ± 0.24 (2.04 %)

Table 6.19: Resulting Higgs mass M_H and cross section σ by merging $\mu\mu X$-channel and eeX-channel with Bremsstrahlung recovery, for the MI Analysis and MD Analysis.

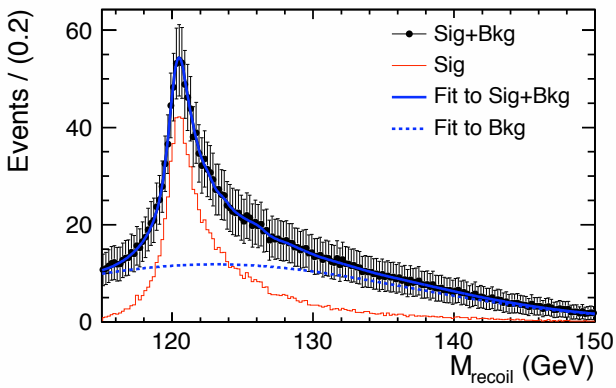

Figure 6.31: Fit to the signal plus background using *Kernel Estimation* for eeX-channel with polarization mode $e^-_R e^+_L$ in MI analysis, with Bremsstrahlung recovery.

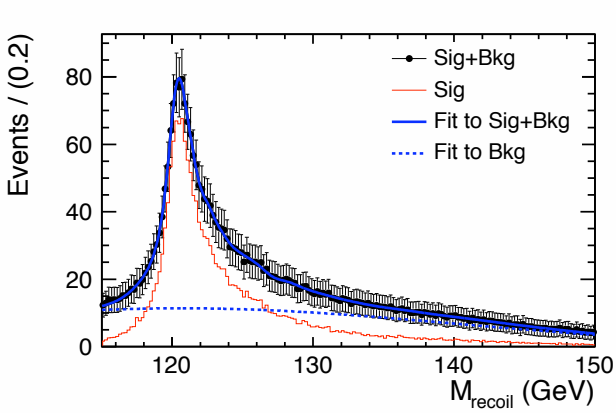

Figure 6.32: Fit to the signal plus background using *Kernel Estimation* for eeX-channel with polarization mode $e^-_L e^+_R$ in MD analysis, with Bremsstrahlung recovery.

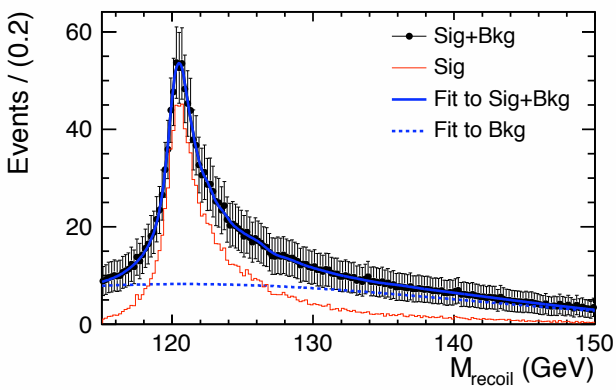

Figure 6.33: Fit to the signal plus background using *Kernel Estimation* for eeX-channel with polarization mode $e^-_R e^+_L$ in MD analysis, with Bremsstrahlung recovery.

ground and the signal selection efficiency are summarized in Table 6.17. Applying *Kernel Estimation* method in the fits, the measured Higgs mass and cross section are given in Table 6.18, and the spectra including the fits are shown in Figure 6.30 to 6.33.

Comparing with the results shown in Section 6.6, it can be concluded that, Bremsstrahlung recovery improves the accuracy of the Higgs mass measurement by about 10% and the cross section measurement by about 20%. The results show that the gain in statistics supersedes the loss in mass resolution. With the Bremsstrahlung recovery, the accuracy of the mass measurement is still worse than that of the $\mu\mu X$-channel by a factor of two. However, the accuracy of the cross section measurement becomes similar to that of the $\mu\mu X$-channel, since it is less sensitive to the mass resolution.

By merging the $\mu\mu X$-channel and eeX-channel with Bremsstrahlung recovery, the best accuracy obtained are 28 MeV for the Higgs mass measurement, and 2.0% for that of the cross section, as shown in Table 6.19.

6.7.3 Discussions of the Systematic Error

This section discusses the potential sources of the systematic error and the possible methods to control them. However, quantitative studies of the systematic error have to be done in future.

In the Higgs Recoil Mass Measurement

In the Higgs recoil mass measurement, the systematic biases appear as the difference between the measured value and the true value. According to Equation 2.34, the observables correlated with the Higgs recoil mass are the center of mass energy and the momenta of the pair of leptons. Uncertainties in these variables propagate into the systematic error of the Higgs recoil mass measurement.

For instance, imperfect knowledges of the tracking system may cause the measured momentum of a track being different from its true value. These imperfect knowledges could be the misalignment of the tracking components, the uncertainty of the drift time in TPC, the imperfect knowledge of the magnetic field, etc.. When this difference propagates to the recoil mass, the measured Higgs mass would be different from its true value.

Other possible sources of systematic error propagated from the track momentum are radiative effects such as Bremsstrahlung in eeX-channel. The Bremsstrahlung depends strongly on the material budget of the detector, all the imperfect knowledges of the detector geometry and material budget could be sources of the systematic error.

Moreover, using the recoil mass method for the mass measurement, the imperfect knowledges of the mean value of the center of mass energy and the Beamstrahlung should be considered as the sources of the systematic error. Incorrect mean value of the center of mass energy may shift the maximum of the recoil mass distribution accordingly. The Beamstrahlung may also shift the recoil mass maximum due to the Convolution Effect according to their intensities, as discussed in Section 6.5. These two

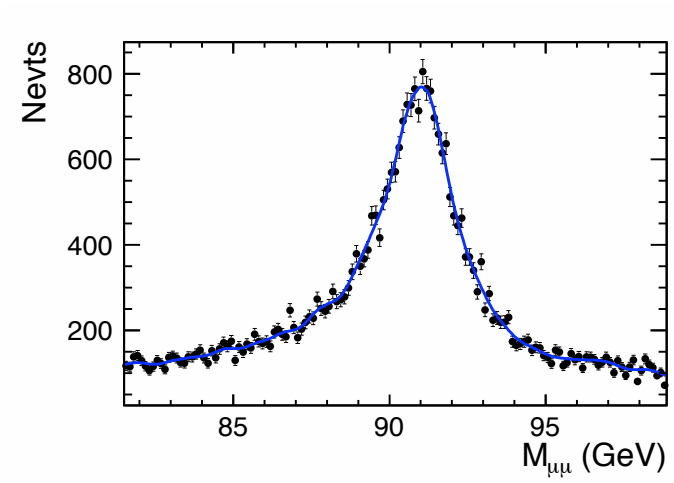

Figure 6.34: Fit of the *Invariant Mass* of the $Z \to \mu^+\mu^-$ in the ZZ process using *Kernel Estimation*, with polarization mode $e^-_L e^+_R$. An accuracy of 13 MeV is obtained for the invariant mass measurement.

effects from the accelerator should be precisely measured.

In conclusion, the major sources of the systematic error of the Higgs recoil mass measurement are imperfect knowledge of the tracking system, the center of mass energy, and the detector material budget. To control them, a well studied reference reaction is needed.

The ZZ process is an excellent choice, with the M_Z precisely known to a precision of 2 MeV[5]. The ZZ process has a similar scenario as the Higgs-strahlung process with the Z decays to a pair of muons or electrons, with the recoil mass of the Higgs replaced by that of the Z. This designated work needs one of the Z decays to a pair of muons or electrons, without constraint on the other Z.

By measurement of the invariant mass of the $Z \to l^+l^-$, the tracking system can be calibrated. At $\sqrt{s} = 250$GeV, assuming $M_H = 120$GeV, the $ZZ \to \mu\mu X/eeX$ has about 40 times larger cross section than that of the $ZH \to \mu\mu X/eeX$. With this much larger statistics the Z mass can be measured to a precision of 13 MeV, using channel $ZZ \to \mu\mu X$, see Figure 6.34 for the fit. Moreover, the $e^+e^- \to Z \to \mu^+\mu^-/e^+e^-$, which has an even larger cross section, can also be employed in this calibration. The resulting systematic error due to the tracking system can be precisely determined and controlled.

The Z recoil mass of the ZZ process can be used to determine and control the center of mass energy and the radiative effects. The Z recoil mass could be determined to a statistical precision of 28 MeV, using channel $ZZ \to \mu\mu X$, see the fit in Figure 6.35. With this small statistical error, the knowledge of the center of mass energy and the radiative effects could be validated precisely.

Other sources of the systematic errors of the Higgs recoil mass measurement could be the methods of background rejection, and the data modeling, i.e., the fit methods. The

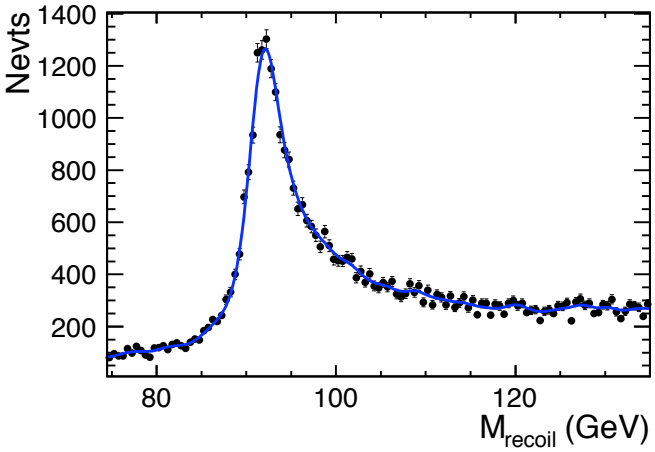

Figure 6.35: Fit of the *Recoil Mass* to the $Z \to \mu^+\mu^-$ in the ZZ process using *Kernel Estimation*, with polarization mode $e^-_L e^+_R$. An accuracy of 28 MeV is obtained for the Z recoil mass measurement.

potential uncertainty due to the data modeling can be measured and corrected using high statistical MC production. For instance, in this study, with 10 ab^{-1} statistics of the Higgs-strahung MC production, three fit methods give nearly identical results. While the methods of the background rejection do not shift the maximum of the recoil mass distribution directly. There are, however, some indirect effects, e.g. the distortion of the tail of the distribution. These are minor effects in the mass measurement and could be corrected by the data modeling.

In the Cross Section Measurement

The error of the cross section can be decomposed as

$$\delta\sigma = \left(\frac{\delta N_{data}}{\epsilon\mathcal{L}}\right)_{stat.} \oplus \left(\frac{\delta N_B}{\epsilon\mathcal{L}} \oplus \frac{N_{data} - N_B}{\epsilon^2\mathcal{L}}\delta\epsilon \oplus \frac{N_{data} - N_B}{\epsilon\mathcal{L}^2}\delta\mathcal{L}\right)_{sys.}, \tag{6.33}$$

where, N_{data} is the total number of events, N_B is the number of background events, ϵ is the efficiency of signal selection, and $\mathcal{L}$ is the luminosity.

The first error term is introduced by the δN_{data}. This is measured by the fit, and treated as the statistical error. The next three error terms are treated as systematic errors, they are the δN_B, $\delta\epsilon$ and the $\delta\mathcal{L}$.

The luminosity will be measured precisely using high statistical calibration processes like the Bhabha scattering. The number of background events could also be estimated precisely, since all the backgrounds related are well studied. With high statistical MC production, the number of background events could be preciously measured process by process.

The most difficult one is the efficiency of the signal selection, whose uncertainty is directly affected by the background rejection methods. This is different from the Higgs recoil mass measurement, where background rejection methods do not affect the observable (M_H) directly.

The procedure to measure the uncertainty of the efficiency is to vary the physics assumptions together with the various background rejection methods to estimate the dependences and covariances between them. Reminding that a very complicated background rejection method is applied in this study, which includes seven to eight cuts together with the Likelihood method, as shown in Section 6.4. The cuts and, especially the Likelihood method, mandatorily introduce more difficulties in the measurement of the uncertainty of the efficiency.

For the cross section measurement, it is found that the statistical error does not request such a high suppression of the background as for the Higgs mass measurement. By removing the Likelihood method and remaining only cuts on some basic variables M_{dl}, P_{Tdl}, and P_{Tdl} (or $N_{add.TK}$), the statistical error on the cross section measurement only increases by about 10% on average. This means a similar statistical error could be obtained with much less sources of systematic error due to the background rejection methods.

Chapter 7

Summary and Outlook

In this dissertation, the strategies for the Higgs recoil mass and the cross section measurements using the Higgs-strahlung process with $Z \to \mu^+\mu^-$ ($\mu\mu X$-channel) and e^+e^- (eeX-channel), are developed. The results obtained in this study are included in the *ILD Letter of Intent*. In a second study, the MIP calibration of the SiW ECAL prototype developed by the CALICE Collaboration is performed for the 2008 FNAL beam test.

Higgs recoil mass and Higgs-strahlung cross section measurement

The study of the Higgs recoil mass and the Higgs-strahlung cross section measurements is based on the full simulation of the ILD detector, assuming a Higgs mass of 120 GeV at center of mass energy $\sqrt{s} = 250$ GeV with an integrated luminorsity of 250 fb^{-1}.

Two beam polarization modes are studied, they are ($e^- : +80\%,\ e^+ : -30\%$) and ($e^- : -80\%,\ e^+ : +30\%$), referred as $e^-_L e^+_R$ and $e^-_R e^+_L$, respectively. At the same time, two parallel analyses are performed. One is called Model Independent (MI) analysis, where no assumption on the Higgs decay mode is made. The second one is named Model Dependent (MD) analysis, which assumes that the Higgs decay leads to at least two charged particles. Accompany with these two analyses, different variables are selected to distinguish the signal and backgrounds. The resulting efficiency of signal selection is around 60% in the $\mu\mu X$-channel and 40% in the eeX-channel. The signal over background ratios are all greater than 0.4, with the best one of 1.5 for the $\mu\mu X$-channel with polarization mode $e^-_R e^+_L$ in the MD analysis.

In the extraction of the Higgs mass and the cross section, three fit functions are studied. These functions lead to nearly identical results.

The results show that, the best precision achieved is 31 MeV on the Higgs mass measurement and 2.75% on the cross section measurement, from the $\mu\mu X$-channel with polarization mode $e^-_L e^+_R$ in the MD analysis. However, the precisions obtained from the eeX-channel are worse by a factor of two for the Higgs mass, while a factor of 1.5 for the cross section, compared to that of the $\mu\mu X$-channel. This is due to the Bremsstrahlung and much larger background on the eeX-channel analysis.

The derived results from MD analysis are consistently more precise by about 10% on average. The small difference between the results confirms that the methods employed for the background rejection in the MI analysis are already very efficient.

The results with polarization mode $e^-_L e^+_R$ are better than that of the $e^-_R e^+_L$ by about 10% in the MI analysis and about 20% in the MD analysis. The reason is that, although polarization mode $e^-_R e^+_L$ suppresses the WW background, the cross sections of the Higgs-strahlung process are smaller by about 20% compared to that of the polarization mode $e^-_L e^+_R$. At the same time, the methods developed are efficient enough for the suppression of the WW background.

Moreover, a possible improvement on the eeX-channel by recovering the Brems-strahlung photons is examined. The resulting accuracy improves by about 10% for the Higgs mass measurement and 20% for the cross section measurement.

Therefore, by merging the $\mu\mu X$-channel and eeX-channel, the best accuracy obtained is 28 MeV for the Higgs mass measurement and 2.0% for that of the cross section, which is from the $\mu\mu X$-channel with polarization mode $e^-_L e^+_R$ in the MD analysis.

It is also studied that the potential systematic error on the Higgs recoil mass can be controlled using the well known ZZ process ($e^+e^- \to ZZ \to l^+l^-X$). From which, the invariant mass of $Z \to \mu^+\mu^-$ can be measured to a precision of 13 MeV, while the Z recoil mass can be measured to a precision of 28 MeV. However, quantitative studies of the systematic error are needed in future.

The analysis has proven that the results are sensitive to the details of accelerator configuration. Based on the current best knowledge of the beam parameters, approximately half the statistical error is generated by uncertainties caused by Beamstrahlung and the energy spread of the incoming beams.

For future studies, the precision of the measurement can be improved by a better muon recognition by including a muon system in the analysis. The precision obtained in the eeX-channel might gain considerably from a revision of the amount of passive material in the detector. It is estimated that the photon-photon background has a minor effect on this study[56], however, systematic studies based on high statistical MC production are required.

MIP calibration of the SiW ECAL prototype

The calibration constants of the SiW ECAL prototype are extracted for each pad for the beam test in 2008 at FNAL. The average of the calibration constants over all pads is 47.61±0.02 ADC counts, and that of the statistical error is 0.516±0.002 ADC counts (1.08% of a MIP). The measured electronic noise is 5.930±0.003 ADC counts on average of all pads, thus a ratio about 7.95 is obtained between the calibration constant and the noise.

The total systematic error is 0.37 ADC counts (0.78% of a MIP) when they are applied to the data using the same trigger, while 1.04 ADC counts (2.18% of a MIP) when they are applied to the data with the other trigger.

The stability of the calibration constants are checked by comparing with those obtained for the beam test at CERN in 2006. The correlation coefficient is 83.76% between the calibration constants obtained at FNAL in 2008 and at CERN in 2006. Considering that plenty of operations like mounting, un-mounting, and shipment were applied on it between 2006 and 2008, this high correlation coefficient demonstrates the stability with time of the SiW ECAL prototype. The difference between the two sets of calibration constants can be understood from the difference of the timing offsets of employed triggers as required by different experimental conditions.

The result gives evidence that the calibration can also be well controlled for a full SiW ECAL in a detector at the ILC.

Appendix A

Figures for Likelihood Further Rejection

The figures in this appendix show the optimization procedure to decide the cut on f_L, for all the eight analysis channels, i.e, for $\mu\mu X$ and eeX channels with $e_L^- e_R^+$ and $e_R^- e_L^+$ polarization modes in MI and SM analyses. See Section 6.4.3 for details.

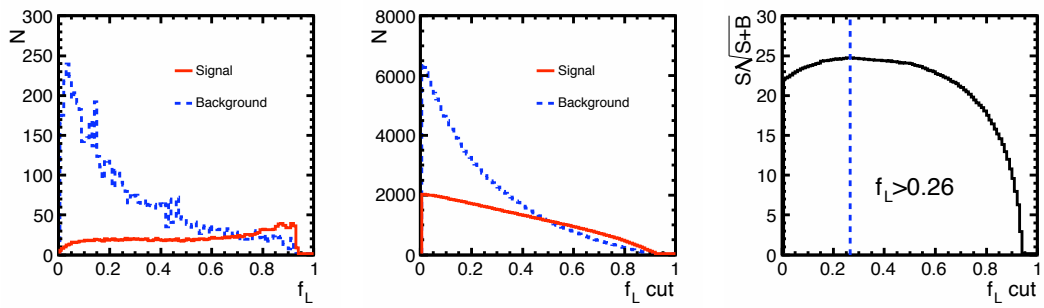

Figure A.1: The distributions of the Likelihood Fraction f_L (left), the number of remaining events versus the cut on f_L (middle), and the significance versus f_L cuts (right). The distributions are shown for the $\mu\mu X$-channel with polarization mode $e_L^- e_R^+$ in the MI Analysis.

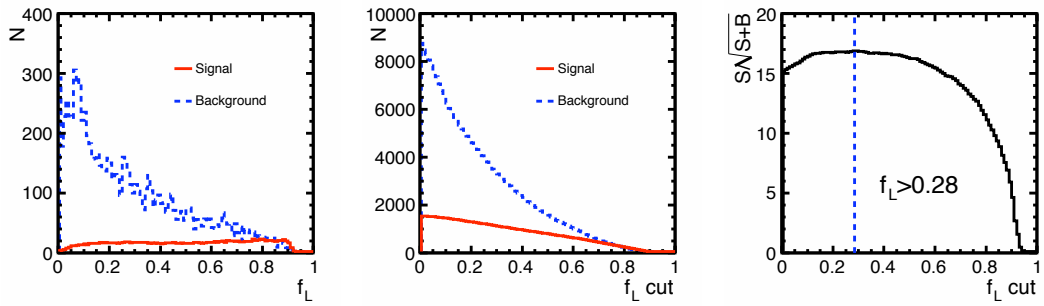

Figure A.2: Same as Figure A.1, but for the eeX-channel with polarization mode $e_L^- e_R^+$ in the MI Analysis.

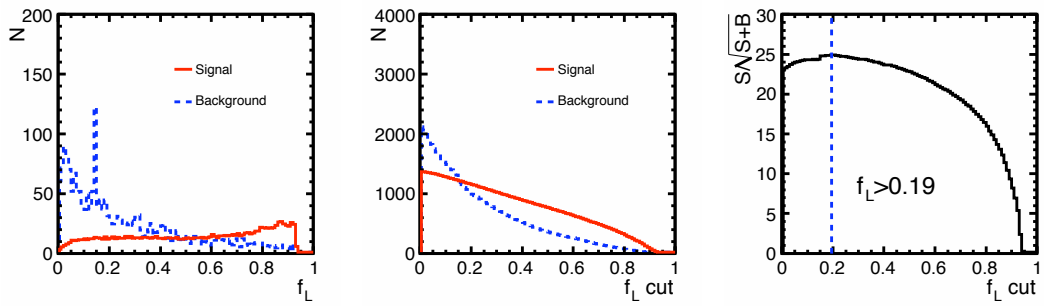

Figure A.3: Same as Figure A.1, but for the $\mu\mu X$-channel with polarization mode $e_R^- e_L^+$ in the MI Analysis.

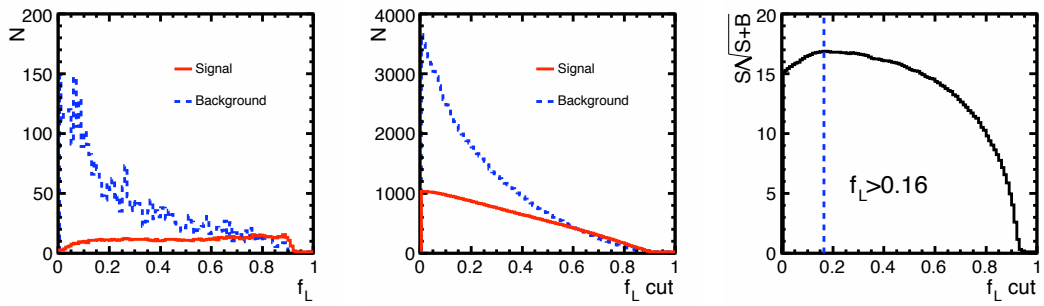

Figure A.4: Same as Figure A.1, but for the eeX-channel with polarization mode $e_R^- e_L^+$ in the MI Analysis.

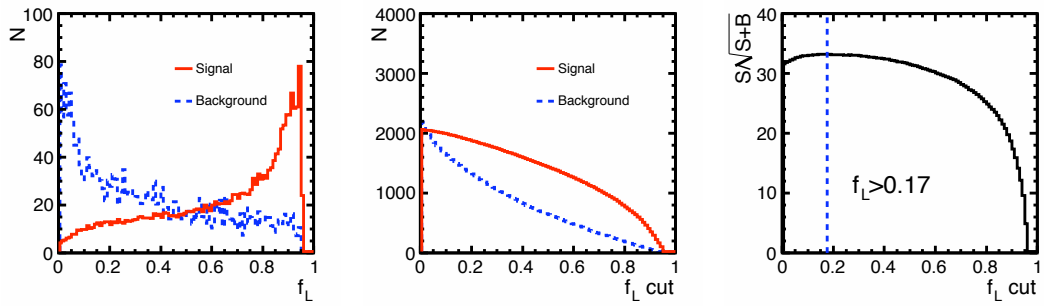

Figure A.5: Same as Figure A.1, but for the $\mu\mu X$-channel with polarization mode $e_L^- e_R^+$ in the MD Analysis.

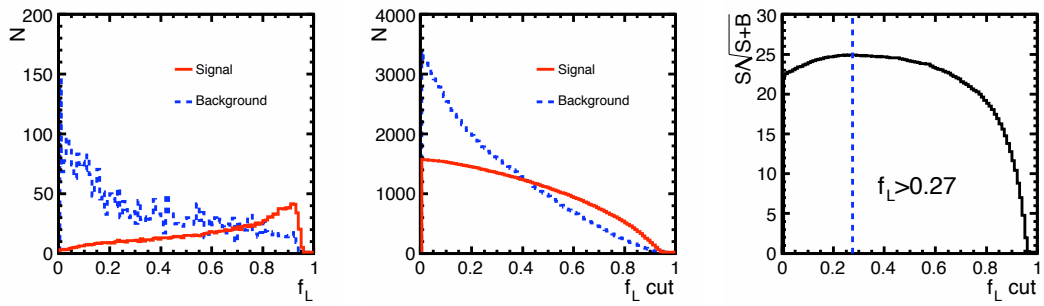

Figure A.6: Same as Figure A.1, but for the eeX-channel with polarization mode $e_L^- e_R^+$ in the MD Analysis.

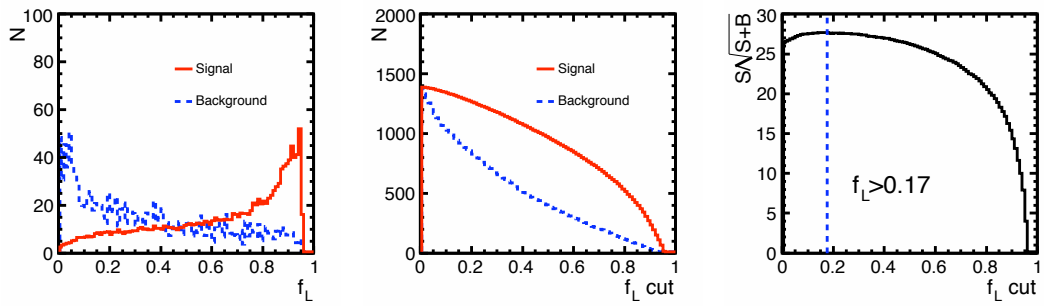

Figure A.7: Same as Figure A.1, but for the $\mu\mu X$-channel with polarization mode $e_R^- e_L^+$ in the MD Analysis.

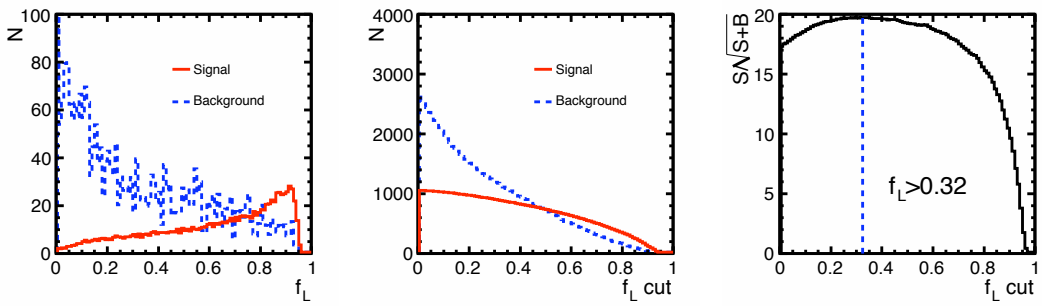

Figure A.8: Same as Figure A.1, but for the eeX-channel with polarization mode $e^-_R e^+_L$ in the MD Analysis.

Appendix B

Tables of Background Rejection

The tables in this appendix give the remaining number of events of signal and background processes after each cuts, for all the eight analysis channels, i.e, for $\mu\mu X$ and eeX channels with $e^-_L e^+_R$ and $e^-_R e^+_L$ polarization modes in MI and SM analyses. See Section 6.4 for details.

MI, $\mu\mu$X, $e^-_L e^+_R$					
N_{evts} Remained	$\mu\mu X$	$\mu^+\mu^-$	$\tau^+\tau^-$	$\mu^+\mu^-\nu\nu$	$\mu^+\mu^- ff$
Before any restriction	2918 (100.0%)	2.6M	1.6M	111k	317k
+ Lepton ID + Tightened Pre-Cuts	2472 (84.72%)	9742	4582	9268	8175
+ $P_{Tdl} > 20$GeV	2408 (82.50%)	7862	3986	8462	7222
+ $M_{dl} \in (80, 100)$GeV	2292 (78.54%)	6299	2679	5493	5658
+ $acop \in (0.2, 3.0)$	2148 (73.61%)	5182	112	5179	5083
+ $\Delta P_{Tbal.} > 10$GeV	2107 (72.20%)	335	80	4705	4706
+ $\lvert\Delta\theta_{2tk}\rvert > 0.01$	2104 (72.11%)	149	80	4647	4676
+ $\lvert\cos\theta_{missing}\rvert < 0.99$	2046 (70.09%)	82	80	4647	3614
+ $M_{recoil} \in (115, 150)$GeV	2028 (69.48%)	75	80	3642	2640
+ $f_L > 0.26$	1596 (54.68%)	41	0	1397	1125

Table B.1: Number of events remaining after each cut for the $\mu\mu X$-channel with polarization mode $e^-_L e^+_R$ in the MI analysis. Efficiencies of signal selection are given inside parentheses.

MI, eeX, $e^-_L e^+_R$					
N_{evts} Remained	eeX	e^+e^-	$\tau^+\tau^-$	$e^+e^-\nu\nu$	e^+e^-ff
Before any restriction	3138 (100.0%)	4.3G	1.6M	147k	110k
+ Lepton ID + Tightened Pre-Cuts	2019 (64.33%)	43607	6422	13196	12548
+ $P_{Tdl} > 20$GeV	1962 (62.50%)	39152	5551	12054	10583
+ $M_{dl} \in (80, 100)$GeV	1755 (55.93%)	25501	3806	7786	7509
+ $acop \in (0.2, 3.0)$	1645 (52.41%)	23228	245	7239	6739
+ $\Delta P_{Tbal.} > 10$GeV	1606 (51.16%)	1725	157	6286	5904
+ $\lvert\Delta\theta_{2tk}\rvert > 0.01$	1603 (51.09%)	990	157	6150	5844
+ $\lvert\cos\theta_{missing}\rvert < 0.99$	1564 (49.83%)	679	157	6149	4643
+ $M_{recoil} \in (115, 150)$GeV	1539 (49.04%)	576	41	4824	3335
+ $f_L > 0.28$	1153 (36.74%)	243	29	2019	1217

Table B.2: Number of events remaining after each cut for the eeX-channel with polarization mode $e^-_L e^+_R$ in the MI analysis. Efficiencies of signal selection are given inside parentheses.

MI, $\mu\mu$**X,** $e^-_R e^+_L$					
N_{evts} Remained	$\mu\mu X$	$\mu^+\mu^-$	$\tau^+\tau^-$	$\mu^+\mu^-\nu\nu$	$\mu^+\mu^-ff$
Before any restriction	1967 (100.0%)	2.0M	1.2M	9k	291k
+ Lepton ID + Tightened Pre-Cuts	1667 (84.73%)	6696	3471	1048	5324
+ $P_{Tdl} > 20$GeV	1623 (82.48%)	5419	3037	957	4600
+ $M_{dl} \in (80, 100)$GeV	1544 (78.47%)	4347	2092	702	3530
+ $acop \in (0.2, 3.0)$	1448 (73.60%)	3592	113	656	3169
+ $\Delta P_{Tbal.} > 10$GeV	1421 (72.21%)	229	81	632	2873
+ $\lvert\Delta\theta_{2tk}\rvert > 0.01$	1419 (72.10%)	101	81	625	2851
+ $\lvert\cos\theta_{missing}\rvert < 0.99$	1379 (70.10%)	54	81	625	2065
+ $M_{recoil} \in (115, 150)$GeV	1367 (69.49%)	50	81	487	1506
+ $f_L > 0.19$	1165 (59.20%)	28	0	243	752

Table B.3: Number of events remaining after each cut for the $\mu\mu X$-channel with polarization mode $e^-_R e^+_L$ in the MI analysis. Efficiencies of signal selection are given inside parentheses.

MI, eeX, $e^-_R e^+_L$					
N_{evts} Remained	eeX	e^+e^-	$\tau^+\tau^-$	$e^+e^-\nu\nu$	e^+e^-ff
Before any restriction	2107 (100.0%)	4.3G	1.2M	17k	1.1M
+ Lepton ID + Tightened Pre-Cuts	1352 (64.16%)	40896	5257	1469	10198
+ $P_{Tdl} > 20$GeV	1313 (62.33%)	36742	4546	1351	8430
+ $M_{dl} \in (80, 100)$GeV	1177 (55.88%)	23993	3051	943	5909
+ $acop \in (0.2, 3.0)$	1103 (52.36%)	21846	107	881	5266
+ $\Delta P_{Tbal.} > 10$GeV	1077 (51.11%)	1612	92	805	4517
+ $\lvert\Delta\theta_{2tk}\rvert > 0.01$	1076 (51.05%)	927	92	799	4465
+ $\lvert\cos\theta_{missing}\rvert < 0.99$	1050 (49.82%)	638	92	799	3484
+ $M_{recoil} \in (115, 150)$GeV	1033 (49.04%)	539	12	586	2521
+ $f_L > 0.16$	909 (43.14%)	326	4	368	1294

Table B.4: Number of events remaining after each cut for the eeX-channel with polarization mode $e^-_R e^+_L$ in the MI analysis. Efficiencies of signal selection are given inside parentheses.

MD, $\mu\mu$**X,** $e^-_L e^+_R$					
N_{evts} Remained	$\mu\mu X$	$\mu^+\mu^-$	$\tau^+\tau^-$	$\mu^+\mu^-\nu\nu$	$\mu^+\mu^-ff$
Before any restriction	2918 (100.0%)	2.6M	1.6M	111k	317k
+ Lepton ID + Tightened Pre-Cuts	2472 (84.72%)	9742	4582	9268	8175
+ $N_{add.TK} > 1$	2453 (84.05%)	604	842	145	6321
+ $\lvert\Delta\theta_{2tk}\rvert > 0.01$	2449 (83.91%)	63	816	14	6254
+ $\lvert\Delta\theta_{min}\rvert > 0.01$	2417 (82.81%)	38	261	1	5711
+ $acop \in (0.2, 3.0)$	2256 (77.29%)	32	0	1	5051
+ $\lvert\cos\theta_{missing}\rvert < 0.99$	2189 (75.00%)	16	0	1	3843
+ $M_{recoil} \in (115, 150)$GeV	2154 (73.81%)	15	0	1	2830
+ $f_L > 0.17$	1911 (65.49%)	11	0	0	1387

Table B.5: Number of events remaining after each cut for the $\mu\mu X$-channel with polarization mode $e^-_L e^+_R$ in the MD analysis. Efficiencies of signal selection are given inside parentheses.

MD, eeX, $e^-_L e^+_R$					
N_{evts} Remained	eeX	e^+e^-	$\tau^+\tau^-$	$e^+e^-\nu\nu$	e^+e^-ff
Before any restriction	3138 (100.0%)	4.3G	1.6M	147k	110k
+ Lepton ID + Tightened Pre-Cuts	2019 (64.33%)	43607	6422	13196	12548
+ $N_{add.TK} > 1$	2004 (63.87%)	3136	1740	374	10202
+ $\lvert\Delta\theta_{2tk}\rvert > 0.01$	2001 (63.77%)	655	1073	79	10095
+ $\lvert\Delta\theta_{min}\rvert > 0.01$	1969 (62.75%)	155	128	6	9271
+ $acop \in (0.2, 3.0)$	1840 (58.62%)	134	0	6	8366
+ $\lvert\cos\theta_{missing}\rvert < 0.99$	1792 (57.11%)	91	0	6	6696
+ $M_{recoil} \in (115, 150)$GeV	1731 (55.16%)	73	0	1	4950
+ $f_L > 0.27$	1378 (43.90%)	27	0	0	1652

Table B.6: Number of events remaining after each cut for the eeX-channel with polarization mode $e^-_L e^+_R$ in the MD analysis. Efficiencies of signal selection are given inside parentheses.

MD, $\mu\mu$**X,** $e^-_R e^+_L$					
N_{evts} Remained	$\mu\mu X$	$\mu^+\mu^-$	$\tau^+\tau^-$	$\mu^+\mu^-\nu\nu$	$\mu^+\mu^-ff$
Before any restriction	1967 (100.0%)	2.0M	1.2M	9k	291k
+ Lepton ID + Tightened Pre-Cuts	1667 (84.73%)	6696	3471	1048	5324
+ $N_{add.TK} > 1$	1654 (84.07%)	415	391	9	4160
+ $\lvert\Delta\theta_{2tk}\rvert > 0.01$	1651 (83.93%)	41	379	0	4108
+ $\lvert\Delta\theta_{min}\rvert > 0.01$	1629 (82.81%)	22	105	0	3739
+ $acop \in (0.2, 3.0)$	1522 (77.34%)	20	0	0	3312
+ $\lvert\cos\theta_{missing}\rvert < 0.99$	1476 (75.03%)	11	0	0	2438
+ $M_{recoil} \in (115, 150)$GeV	1453 (73.85%)	10	0	0	1803
+ $f_L > 0.17$	1289 (65.53%)	8	0	0	875

Table B.7: Number of events remaining after each cut for the $\mu\mu X$-channel with polarization mode $e^-_R e^+_L$ in the MD analysis. Efficiencies of signal selection are given inside parentheses.

MD, eeX, $e^-_R e^+_L$					
N_{evts} Remained	eeX	e^+e^-	$\tau^+\tau^-$	$e^+e^-\nu\nu$	e^+e^-ff
Before any restriction	2107 (100.0%)	4.3G	1.2M	17k	1.1M
+ Lepton ID + Tightened Pre-Cuts	1352 (64.16%)	40896	5257	1469	10198
+ $N_{add.TK} > 1$	1342 (63.69%)	2935	1500	22	8227
+ $\lvert\Delta\theta_{2tk}\rvert > 0.01$	1340 (63.60%)	617	859	4	8133
+ $\lvert\Delta\theta_{min}\rvert > 0.01$	1319 (62.59%)	146	57	0	7388
+ $acop \in (0.2, 3.0)$	1232 (58.47%)	125	0	0	6651
+ $\lvert\cos\theta_{missing}\rvert < 0.99$	1201 (57.00%)	84	0	0	5265
+ $M_{recoil} \in (115, 150)$GeV	1161 (55.10%)	67	0	0	3886
+ $f_L > 0.32$	889 (42.20%)	20	0	0	1119

Table B.8: Number of events remaining after each cut for the eeX-channel with polarization mode $e^-_R e^+_L$ in the MD analysis. Efficiencies of signal selection are given inside parentheses.

Appendix C

The Development Physics Motivated Function for Higgs Recoil Mass Distribution

The Physics Motivated Function to describe the Higgs recoil mass distribution is developed in this appendix. The development starts from the Beamstrahlung approximation formula developed by Yokoya and Chen. It is thereafter convoluted analytically with the ISR formula, and then convoluted numerically with the Gaussian function. The application in the measurements of the Higgs recoil mass and Higgs-Strahlung cross-section is discussed in Section 6.5.

C.1 Beamstrahlung Photon Distribution for Both Beams

The development starts from the Yokoya-Chen Beamstrahlung approximation[49, 50, 51, 52] for the photon distribution of one beam with one photon :

$$f(y) = e^{-N}\delta(y) + e^{-N}N\frac{\kappa^{\frac{1}{3}}}{\Gamma(\frac{1}{3})}e^{-\kappa y}y^{-\frac{2}{3}} \ , \tag{C.1}$$

where, N is the average number of emitted photons before an interaction, which is is about one half of the average number of emitted photons after a full bunch crossing n_γ, i.e. $N = n_\gamma/2$; $\kappa = 2/(3\Upsilon)$ with Υ being the quantum parameter of synchrotron radiation; and $y = k/E_{beam}$ with k being the energy of emitted photon.

For $\sqrt{s} = 250$ GeV, $N_\gamma = 0.89$ and $\Upsilon = 0.016$, $N = 0.445$ and $\kappa = 41.67$, see Table 3.2 in Section 3.1. These numbers are taken for all the numerical calculations in the following.

Equation C.1 can be decomposed as:

$$f(y) = p(0) \cdot g(y;\ 0) + p(1) \cdot g(y;\ 1) \tag{C.2}$$

where,

$$
\begin{aligned}
p(0) = e^{-N}, \qquad & g(y;\ 0) = \delta(y) \qquad && : \ 0\ photon \\
p(1) = e^{-N}N, \quad & g(y;\ 1) = \frac{\kappa^{\frac{1}{3}}}{\Gamma(\frac{1}{3})} e^{-\kappa y} y^{-\frac{2}{3}} && : \ 1\ photon
\end{aligned}
$$

It can be found that the $p(i)$ is essentially the Poisson distribution,

$$
p(i) = \frac{e^N N^i}{i!} \ , \tag{C.3}
$$

where, i is the number of photons.

Therefore, the $p(i)$ gives the probability of i photons radiation, and $g(y;\ i)$ gives the photon energy distribution with i photons radiation.

Above showed is for one beam. For two beams, the probability of i photons radiation can be given by

$$
p(i) = \frac{2^i}{i!} \left(\frac{n_\gamma}{2} \right)^i e^{-n_\gamma} \ , \tag{C.4}
$$

Taken the $n_\gamma = 0.89$ given before, the probabilities can be listed as:

$$
\begin{aligned}
&0\ photon\ : && P(0) = && e^{-2N} = 41.58\% && \\
&1\ photon\ : && P(1) = 2 && Ne^{-2N} = 36.49\%; && \sum_{i=0}^{1} P(i) = 78.07\% \\
&2\ photons : && P(2) = 2 && N^2 e^{-2N} = 16.01\%; && \sum_{i=0}^{2} P(i) = 94.08\% \\
&3\ photons : && P(3) = \tfrac{4}{3} && N^3 e^{-2N} = 4.68\%; && \sum_{i=0}^{3} P(i) = 98.76\% \\
&4\ photons : && P(4) = \tfrac{2}{3} && N^4 e^{-2N} = 1.03\%; && \sum_{i=0}^{4} P(i) = 99.79\% \\
&5\ photons : && P(5) = \tfrac{4}{15} && N^5 e^{-2N} = 0.18\%; && \sum_{i=0}^{5} P(i) = 99.97\%
\end{aligned} \tag{C.5}
$$

Therefore, an approximation with up to 4 photons is enough, which can already account for 99.79% of the probability.

At the same time, the photon energy distributions $g_i(y)$ can be derived by analytical convolutions, given by:

$$
\begin{aligned}
g(y;\ 0) &= \delta(y) && : \ 0\ photon \\
g(y;\ 1) = g(y;\ 1) \otimes g(y;\ 0) &= \frac{\kappa^{\frac{1}{3}}}{\Gamma(\frac{1}{3})} \cdot e^{-\kappa y} \cdot y^{\frac{1}{3}-1} && : \ 1\ photon \\
g(y;\ 2) = g(y;\ 1) \otimes g(y;\ 1) &= \frac{\kappa^{\frac{2}{3}}}{\Gamma(\frac{2}{3})} \cdot e^{-\kappa y} \cdot y^{\frac{2}{3}-1} && : \ 2\ photons \\
g(y;\ 3) = g(y;\ 2) \otimes g(y;\ 1) &= \frac{\kappa^{\frac{3}{3}}}{\Gamma(\frac{3}{3})} \cdot e^{-\kappa y} \cdot y^{\frac{3}{3}-1} && : \ 3\ photons \\
g(y;\ 4) = g(y;\ 3) \otimes g(y;\ 1) &= \frac{\kappa^{\frac{4}{3}}}{\Gamma(\frac{4}{3})} \cdot e^{-\kappa y} \cdot y^{\frac{4}{3}-1} && : \ 4\ photons
\end{aligned}
\tag{C.6}
$$

It can be proved that all the $g(y;\ i)$ are normalized, i.e.

$$
\begin{aligned}
\int_0^1 G_1(y)dy &= 1 - \frac{\Gamma(\frac{1}{3}, \kappa)}{\Gamma(\frac{1}{3})} && = 1 \ : \ 1\ photon \\
\int_0^1 G_2(y)dy &= 1 - \frac{\Gamma(\frac{2}{3}, \kappa)}{\Gamma(\frac{2}{3})} && = 1 \ : \ 2\ photons \\
\int_0^1 G_3(y)dy &= 1 - e^{-\kappa} && = 1 \ : \ 3\ photons \\
\int_0^1 G_4(y)dy &= 1 - \frac{\Gamma(\frac{1}{3}, \kappa)}{\Gamma(\frac{1}{3})} - \frac{3e^{-\kappa}\kappa^{\frac{1}{3}}}{\Gamma(\frac{1}{3})} && = 1 \ : \ 4\ photons
\end{aligned}
\tag{C.7}
$$

Thus, the Beamstrahlung distribution for two beams can be given as Equation C.8, which is also a normalized PDF.

$$
f(y) = \sum_{i=0}^{4} p(i) g(y;\ i) \tag{C.8}
$$

C.2 ISR

The ISR approximation[53] is given as:

$$
r(y) = \beta y^{\beta-1}\ , \tag{C.9}
$$

where,

$$\beta = \frac{2\alpha}{\pi}[log(\frac{s}{m_e^2}) - 1] = 0.117$$

for $\sqrt{\mathrm{s}} = 250$ GeV.

To account for the ISR into the radiative effects, one need to do the convolution of Beamstrahlung Distribution Equation C.8 with the ISR Distribution Equation C.9:

$$f_1(y) = f(y) \otimes r(y) = \sum_{i=0}^{4} p(i) \cdot [g(y;\ i) \otimes r(y)] = \sum_{i=0}^{4} p(i) \cdot g_1(y;\ i) \tag{C.10}$$

The analytical convolutions of $g(y;\ i)$ with $r(y)$ give:

$$\begin{aligned}
g_1(y;\ 0) &= g(y;\ 0) \otimes r(y) = \beta \cdot y^{\beta-1} && :\ 0\ photon \\
g_1(y;\ 1) &= g(y;\ 1) \otimes r(y) = \kappa^{\frac{1}{3}} \cdot y^{(\frac{1}{3}+\beta-1)} \cdot \frac{\Gamma(1+\beta)}{\Gamma(\frac{1}{3}+\beta)} \cdot\ {}_1F_1(\frac{1}{3}, \frac{1}{3}+\beta, -\kappa y) && :\ 1\ photon \\
g_1(y;\ 2) &= g(y;\ 2) \otimes r(y) = \kappa^{\frac{2}{3}} \cdot y^{(\frac{2}{3}+\beta-1)} \cdot \frac{\Gamma(1+\beta)}{\Gamma(\frac{2}{3}+\beta)} \cdot\ {}_1F_1(\frac{2}{3}, \frac{2}{3}+\beta, -\kappa y) && :\ 2\ photons \\
g_1(y;\ 3) &= g(y;\ 3) \otimes r(y) = \kappa^{\frac{3}{3}} \cdot y^{(\frac{3}{3}+\beta-1)} \cdot \frac{\Gamma(1+\beta)}{\Gamma(\frac{3}{3}+\beta)} \cdot\ {}_1F_1(\frac{3}{3}, \frac{3}{3}+\beta, -\kappa y) && :\ 3\ photons \\
g_1(y;\ 4) &= g(y;\ 4) \otimes r(y) = \kappa^{\frac{4}{3}} \cdot y^{(\frac{4}{3}+\beta-1)} \cdot \frac{\Gamma(1+\beta)}{\Gamma(\frac{4}{3}+\beta)} \cdot\ {}_1F_1(\frac{4}{3}, \frac{4}{3}+\beta, -\kappa y) && :\ 4\ photons
\end{aligned} \tag{C.11}$$

where ${}_1F_1(a, b, z)$ is the *Confluent Hypergeometric Function*. They can be simply written as

$$g_1(y; i) = \kappa^{\frac{i}{3}} \cdot y^{(\frac{i}{3}+\beta-1)} \cdot \frac{\Gamma(1+\beta)}{\Gamma(\frac{i}{3}+\beta)} \cdot\ {}_1F_1(\frac{i}{3}, \frac{i}{3}+\beta, -\kappa y)\ . \tag{C.12}$$

It can also be proved that $g_1(y;\ i)$ are normalized PDFs.

Therefore, the distribution of radiative effects including Beamstrahlung and ISR can then be expressed as:

$$f_1(y) = \sum_{i=0}^{4} p(i) g_1(y;\ i) \tag{C.13}$$

C.3 Gaussian Spread

It is assumed that the beam energy spread and the uncertainty of detector response can be represented as a Gaussian function:

$$G(y;\ 0,\sigma) = \frac{1}{\sqrt{2\pi}\ \sigma}\ e^{-\frac{y^2}{2\sigma^2}} \tag{C.14}$$

where, σ in Gaussian function represents the beam energy spread and uncertainty of detector response, which is defined as a fraction of the beam energy.

To include the Gaussian Spread into the expression, the convolution of $f_1(y)$ in Equation C.13 with the Gaussian function $G(y;\ 0,\sigma)$ in Equation C.14 numerically.

$$f_2(y) = f_1(y) \otimes G(y;\ 0,\sigma) = \sum_{i=0}^{4} p(i) \cdot [g_1(y;\ i) \otimes G(y;\ 0,\sigma)] \tag{C.15}$$

For example, at $\sqrt{s} = 250$ GeV, the beam energy spread is 0.28% for electron beam and 0.18% for positron beam. Therefore, the over all beam energy spread is give as:

$$\sigma = \sqrt{(0.28\%)^2 + (0.18\%)^2} = 0.33\% \tag{C.16}$$

C.4 Projection to Recoil Mass Distribution

The center of mass energy after radiation can be expressed as

$$s = (\sqrt{s_0} - k)^2 - k^2\ , \tag{C.17}$$

where, $\sqrt{s_0}$ is the designed center of mass energy, i.e. 250 GeV.

Replacing k by $y = k/(\sqrt{s_0}/2)$, Equation C.17 becomes

$$s = s_0(1 - y)\ . \tag{C.18}$$

The recoil mass (denoted by x for convenient) can be derived starting from

$$x^2 = E_H^2 - P_H^2 = (\sqrt{s_0} - E_Z)^2 - P_H^2 \tag{C.19}$$

From kinematics of two body decay, we have

$$E_Z = \frac{s - M_H^2 - M_Z^2}{2\sqrt{s}} \qquad (a)$$

$$|P_H| = |P_Z| = \frac{\sqrt{[s-(M_H+M_Z)^2][s-(M_H-M_Z)^2]}}{2\sqrt{s}} \qquad (b) \qquad \text{(C.20)}$$

$$M_Z^2 = E_Z^2 - P_Z^2 \qquad (c)$$

Using Equation C.20, Equation C.19 becomes

$$x^2 = s_0 + M_Z^2 - \frac{\sqrt{s_0}}{\sqrt{s}} \cdot (s - M_H^2 + M_Z^2) \qquad \text{(C.21)}$$

Taking Equation C.18 to replace $\sqrt{s}$ by y, Equation C.21 becomes

$$x^2 = s_0 + M_Z^2 - \frac{s_0(1-y) - M_H^2 + M_Z^2}{\sqrt{1-y}} \qquad \text{(C.22)}$$

At the same time, y can be expressed in terms of x,

$$\begin{aligned} y(x) = \frac{1}{2s_0^2} \cdot \Big[& 2s_0(x^2 - M_H^2) + (s_0 + x^2 - M_Z^2)(s_0 - x^2 + M_Z^2) - \\ & (s_0 - M^2 + M_Z^2) \cdot \sqrt{4s_0(M_H^2 - M_Z^2) + (s_0 - x^2 + M_Z^2)^2} \Big] \end{aligned} \qquad \text{(C.23)}$$

And, dy/dx is given by,

$$\frac{dy}{dx} = \frac{x}{s_0^2} \cdot \frac{\left[s_0 - x^2 + M_Z^2 + \sqrt{4s_0(M_H^2 - M_Z^2) + (s_0 - x^2 + M_Z^2)^2} \right]^2}{\sqrt{4s_0(M_H^2 - M_Z^2) + (s_0 - x^2 + M_Z^2)^2}} \qquad \text{(C.24)}$$

Now, the Higgs recoil mass function $F(x)$ can be given as,

$$F(x) = f_2(y(x)) \cdot \left| \frac{dy}{dx} \right| \qquad \text{(C.25)}$$

The function $F(x)$ with all the parameters given in advance is compared with the distribution using Monte Carlo event generation. As shown in Figure C.1, it provide a reasonably good approximation of the HIggs recoil mass distribution.

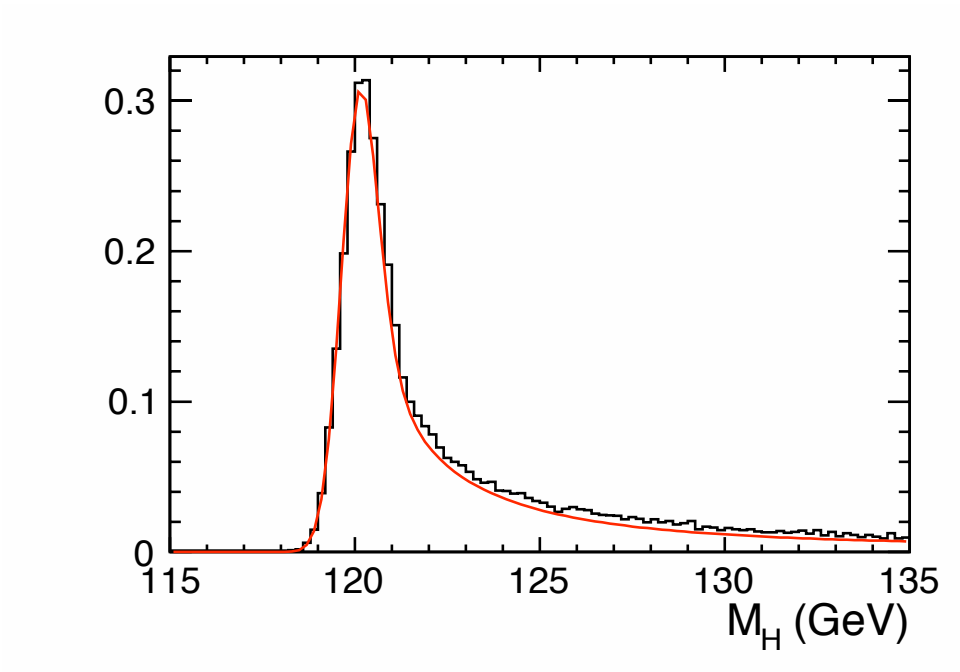

Figure C.1: Comparison of $F(x)$ with the higgs recoil mass distribution using Monte Carlo event generation.

Appendix D

Fit Plots

The fit plots to the signal plus background to extracting the Higgs mass and Higgs-Strahlung cross-section are shown in this appendix. Three functions are employed to describe the signal distribution, they are *GPET Function*, *Kernel Estimation*, and *Physics Motivated Function*, see Section 6.5 for details. The fits are performed for signal plus background for all the eight analysis channels, i.e., for $\mu\mu X$ and eeX channels with $\mathrm{e}^-_\mathrm{L}\mathrm{e}^+_\mathrm{R}$ and $\mathrm{e}^-_\mathrm{R}\mathrm{e}^+_\mathrm{L}$ polarization modes in MI Analysis and MD Analysis. The extracted results of Higgs mass and Higgs-Strahlung cross-section are shown in Section 6.6.

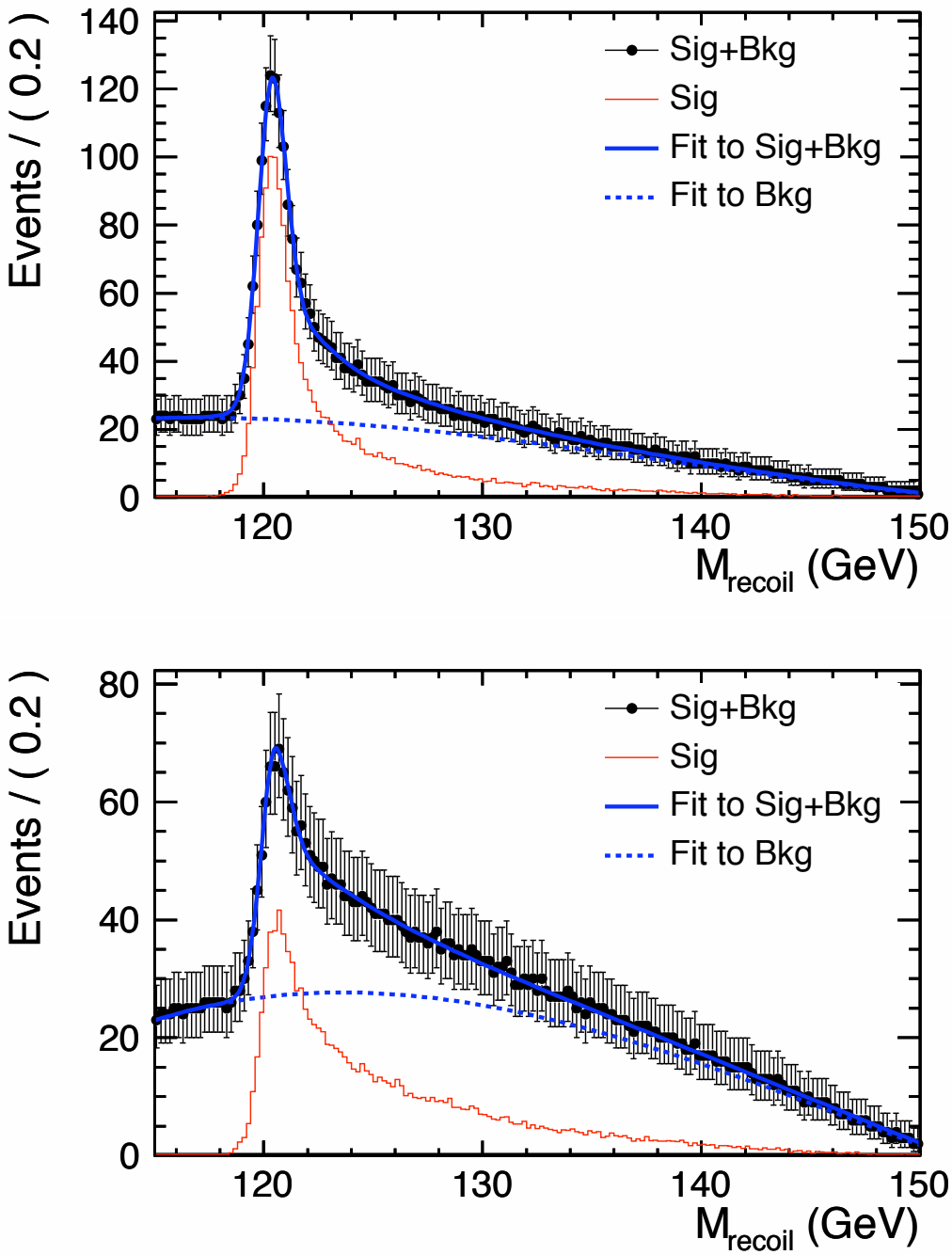

Figure D.1: Fit to the signal plus background using *GPET Function* of $\mu\mu X$ (top) and eeX (bottom) channels with polarization mode $e^-_L e^+_R$, in MI analysis.

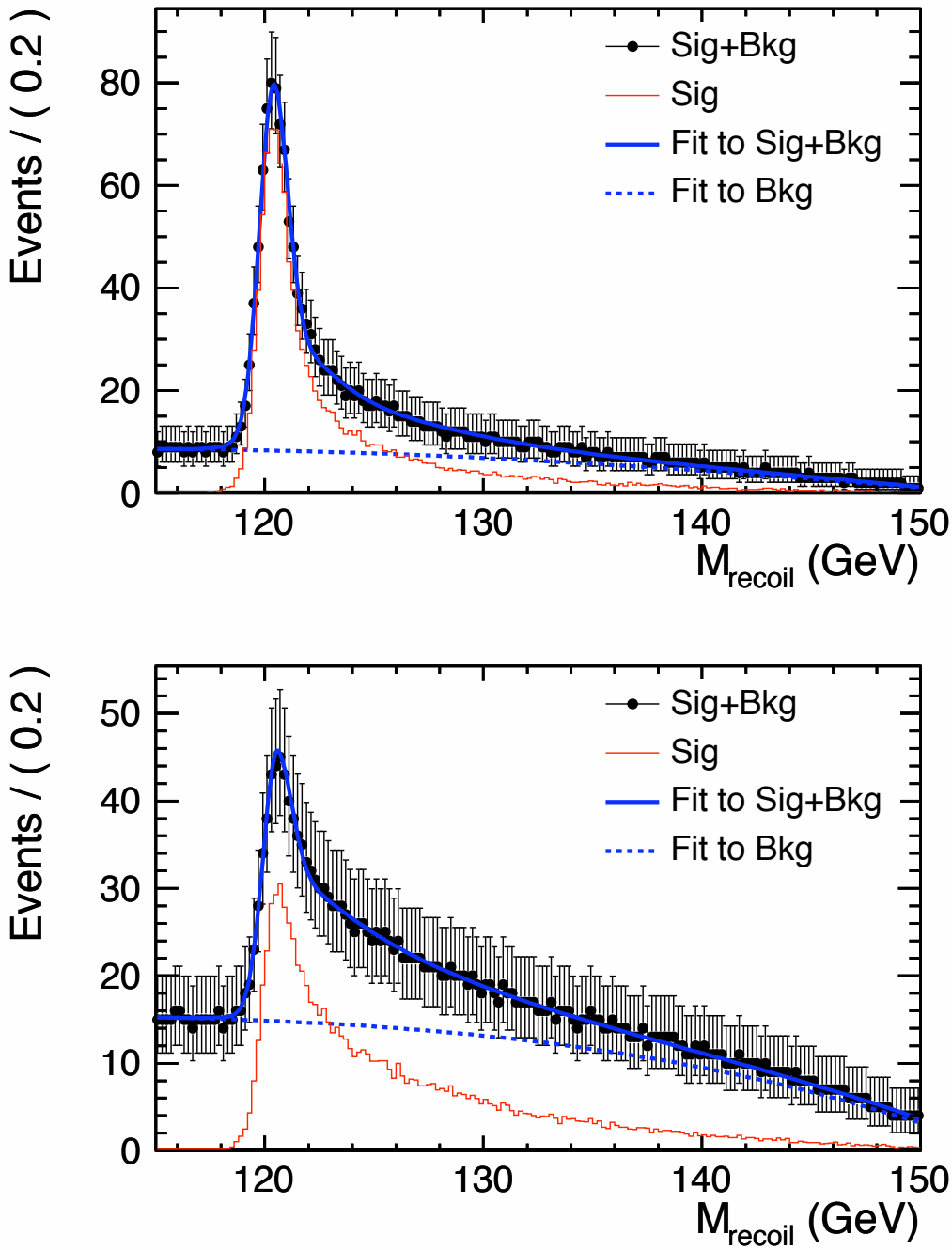

Figure D.2: Fit to the signal plus background using *GPET Function* of $\mu\mu X$ (top) and eeX (bottom) channels with polarization mode $e^-_R e^+_L$, in MI analysis.

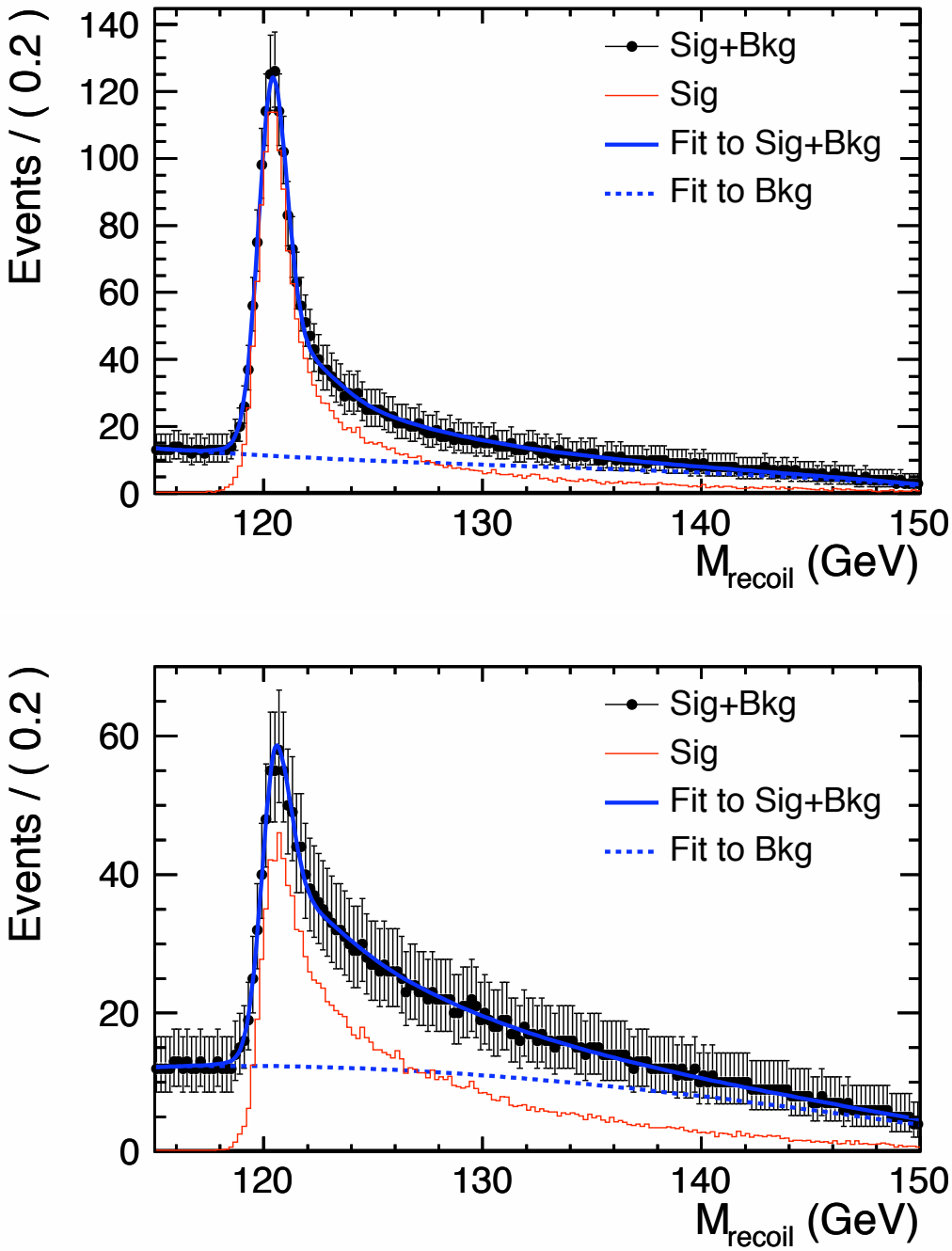

Figure D.3: Fit to the signal plus background using *GPET Function* of $\mu\mu X$ (top) and eeX (bottom) channels with polarization mode $e^-_L e^+_R$, in MD analysis.

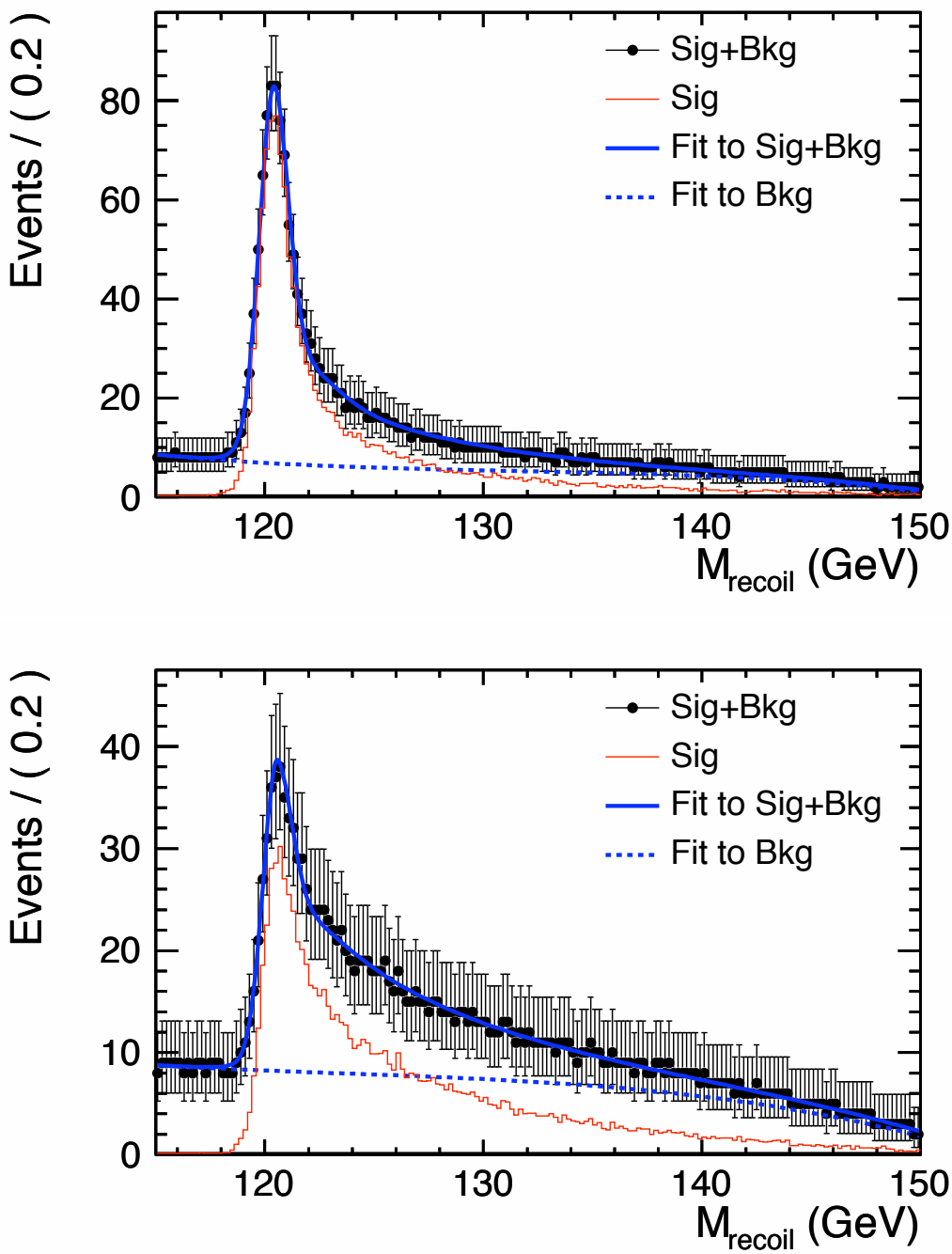

Figure D.4: Fit to the signal plus background using *GPET Function* of $\mu\mu X$ (top) and eeX (bottom) channels with polarization mode $e^-_R e^+_L$, in MD analysis.

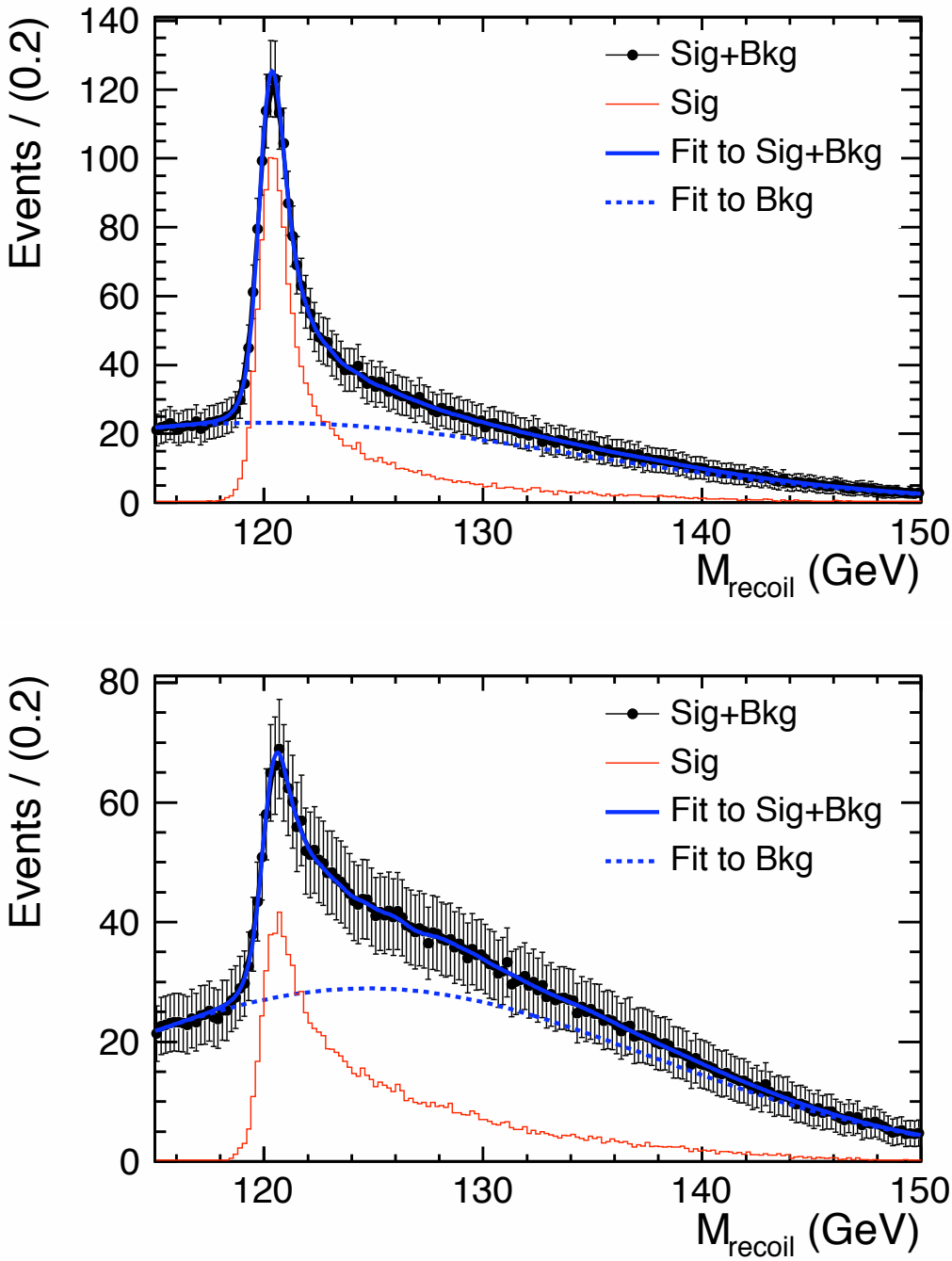

Figure D.5: Fit to the signal plus background using *Kernel Estimation* of $\mu\mu X$ (top) and eeX (bottom) channels with polarization mode $e^-_L e^+_R$, in MI analysis.

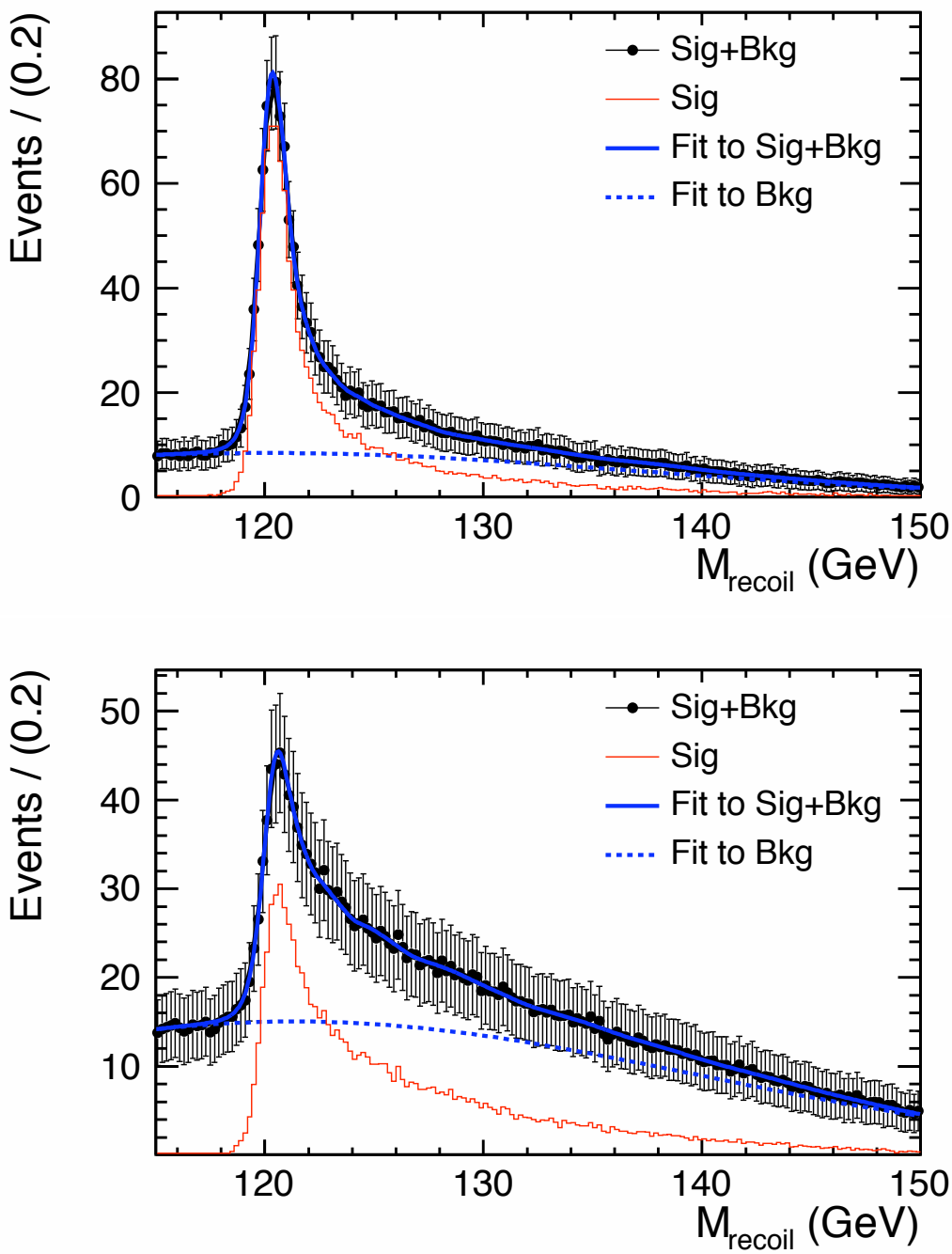

Figure D.6: Fit to the signal plus background using *Kernel Estimation* of $\mu\mu X$ (top) and eeX (bottom) channels with polarization mode $e^-_R e^+_L$, in MI analysis.

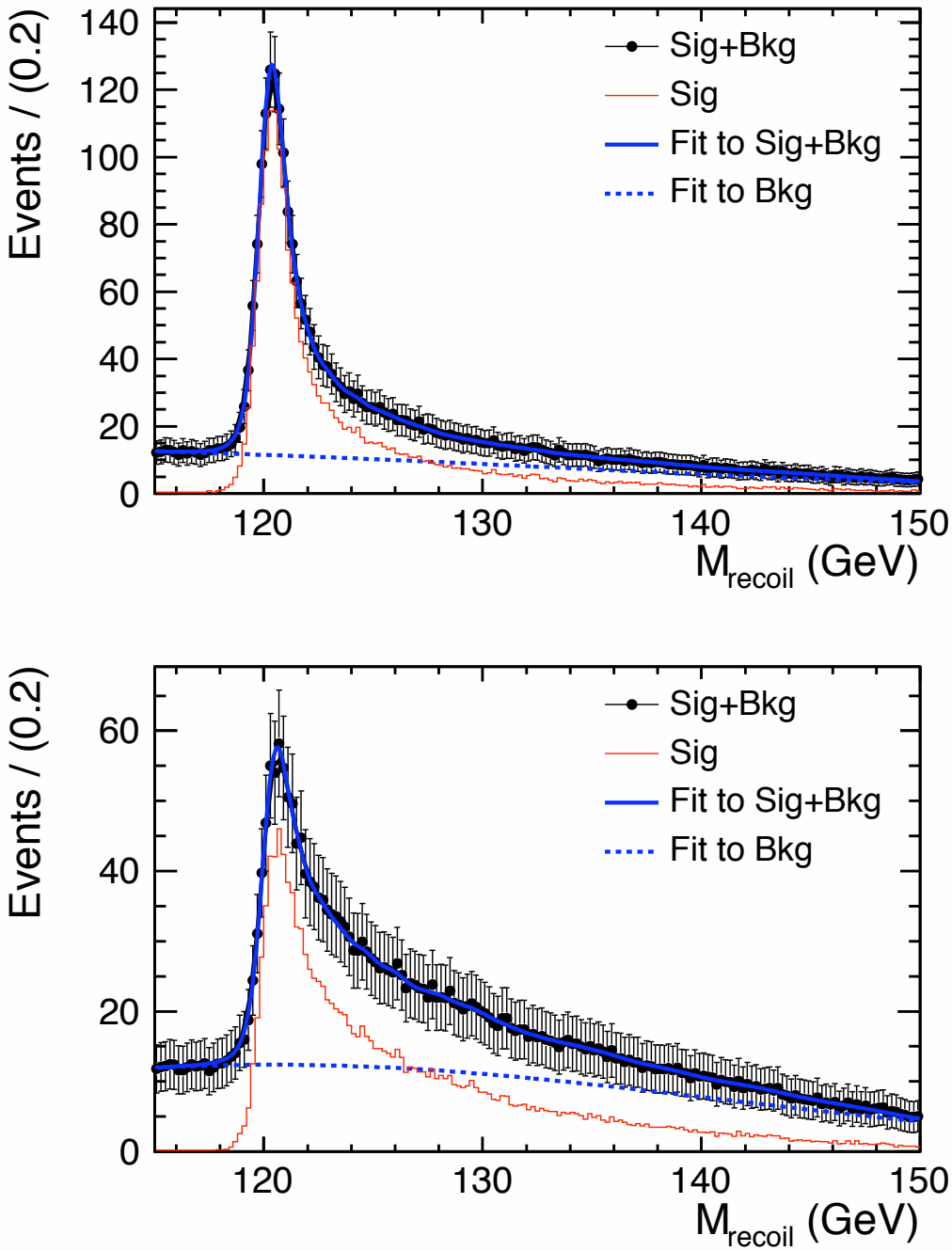

Figure D.7: Fit to the signal plus background using *Kernel Estimation* of $\mu\mu X$ (top) and eeX (bottom) channels with polarization mode $e^-_L e^+_R$, in MD analysis.

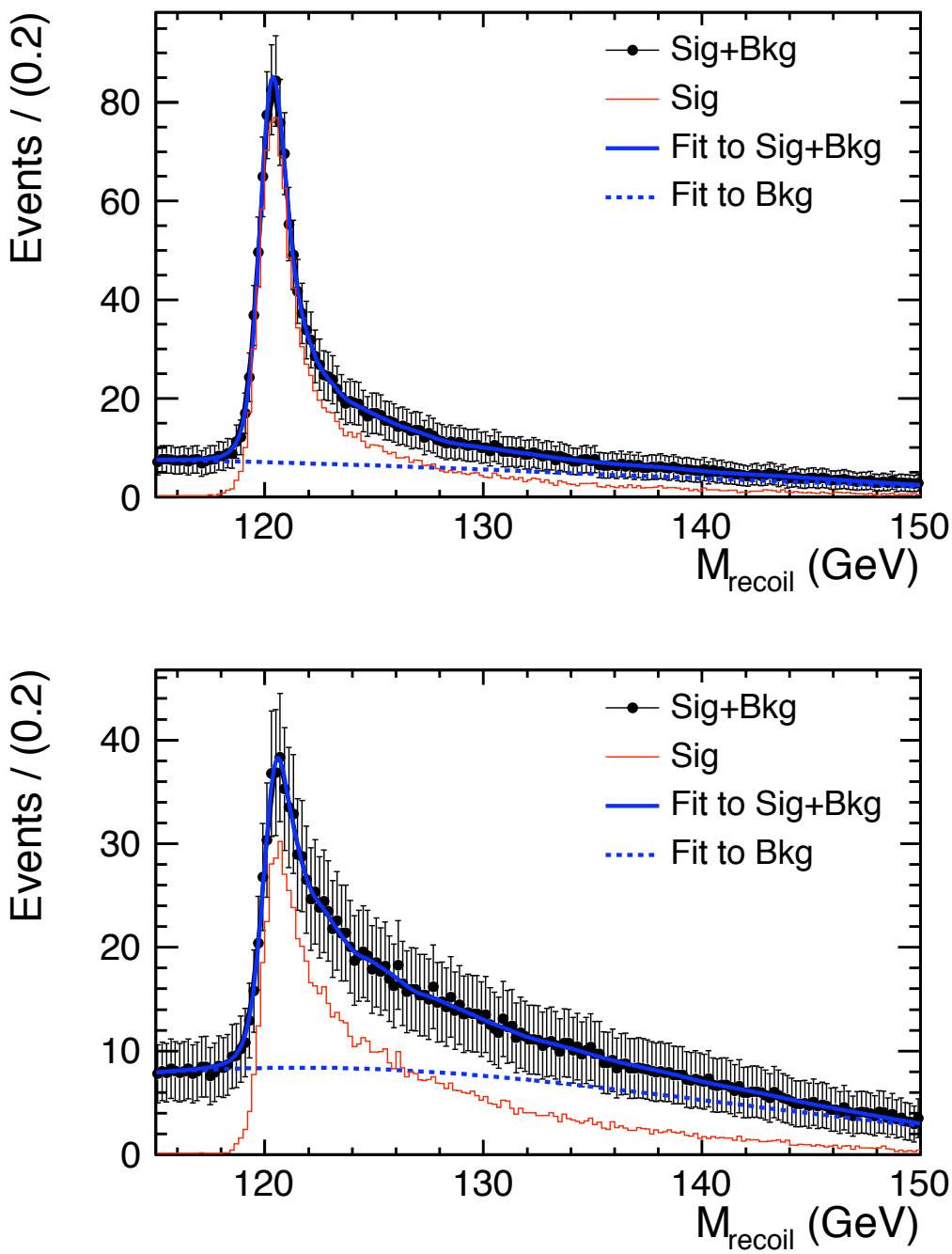

Figure D.8: Fit to the signal plus background using *Kernel Estimation* of $\mu\mu X$ (top) and eeX (bottom) channels with polarization mode $e^-_R e^+_L$, in MD analysis.

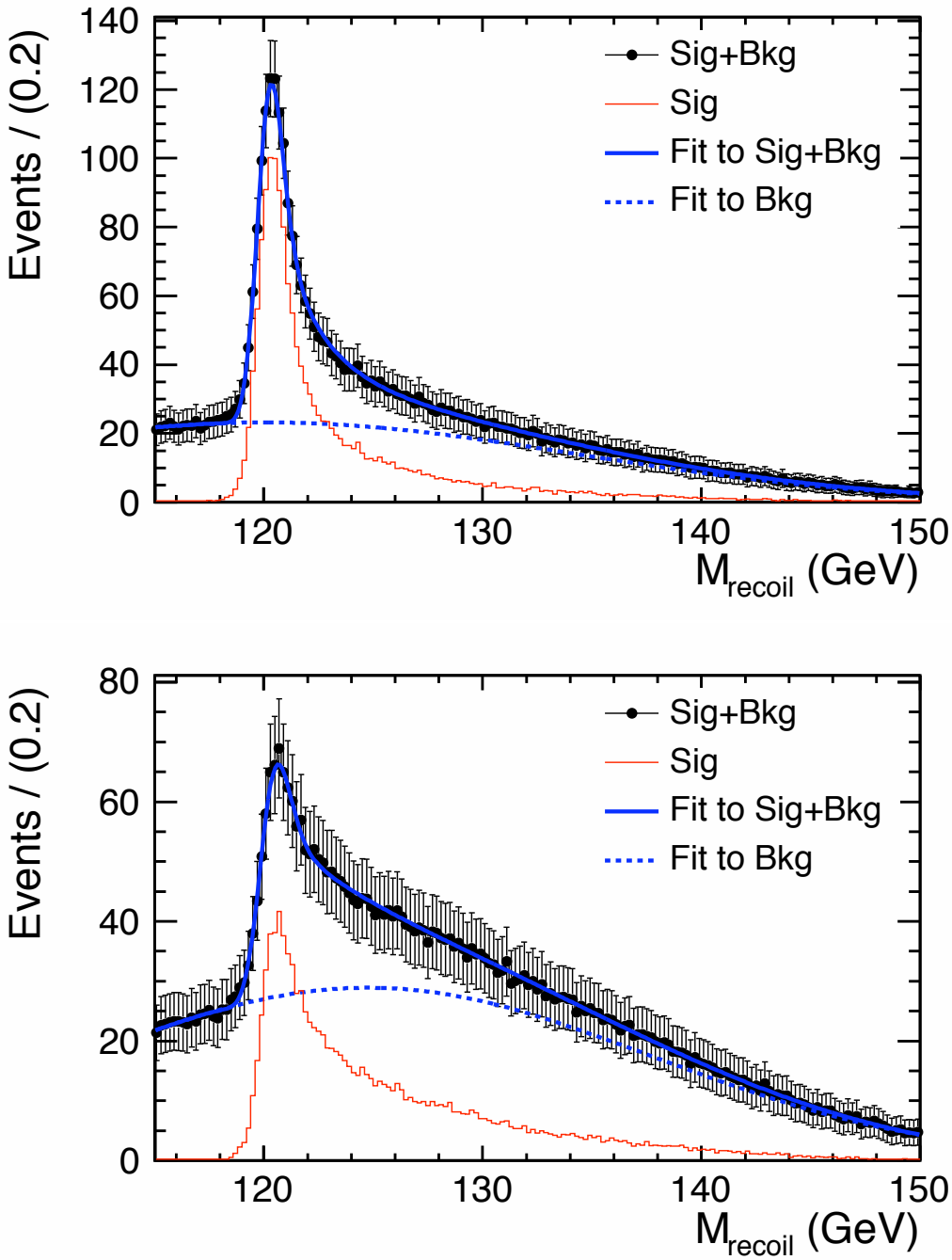

Figure D.9: Fit to the signal plus background using *Physics Motivated Function* of $\mu\mu X$ (top) and eeX (bottom) channels with polarization mode $e^-_L e^+_R$, in MI analysis.

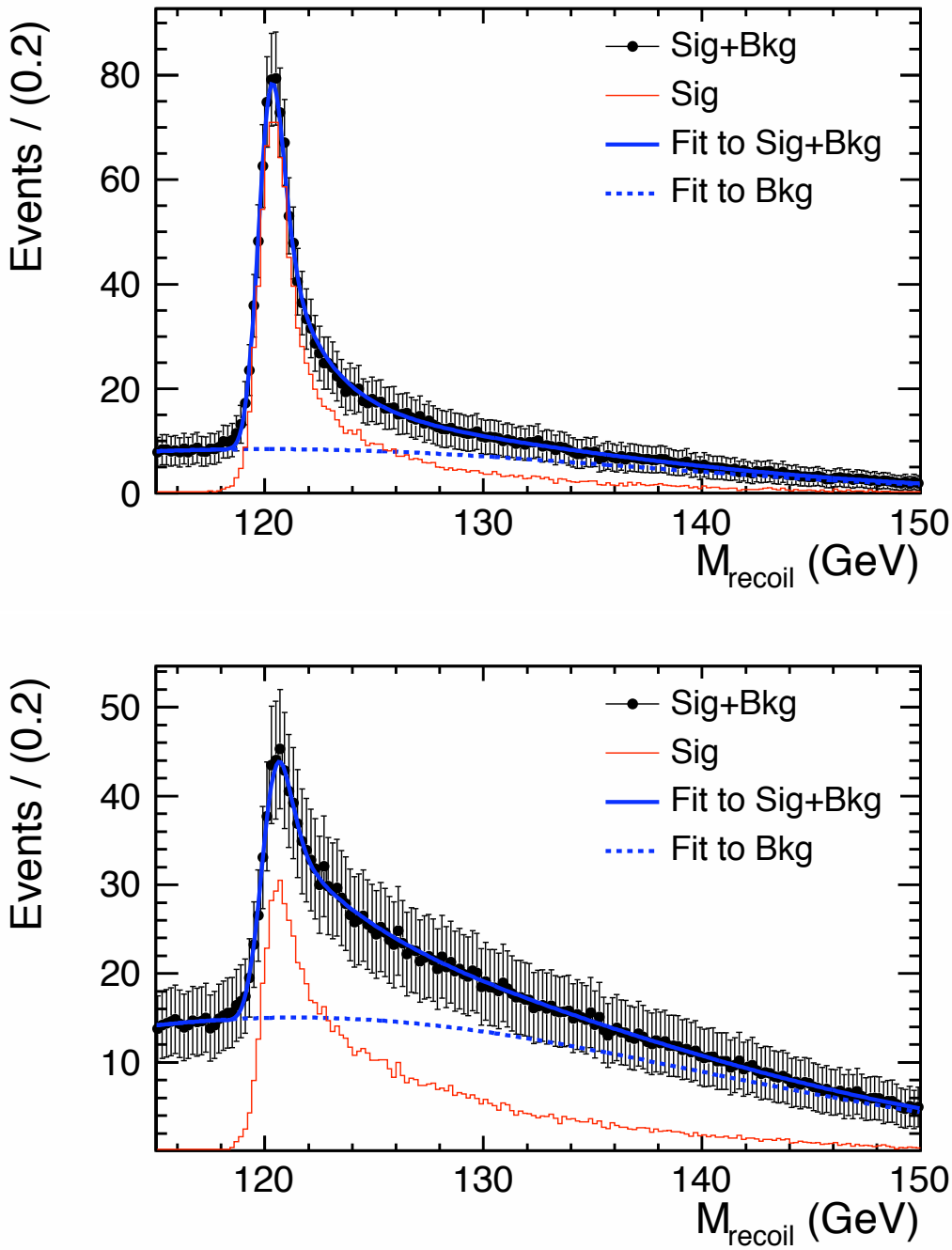

Figure D.10: Fit to the signal plus background using *Physics Motivated Function* of $\mu\mu X$ (top) and eeX (bottom) channels with polarization mode $e^-_R e^+_L$, in MI analysis.

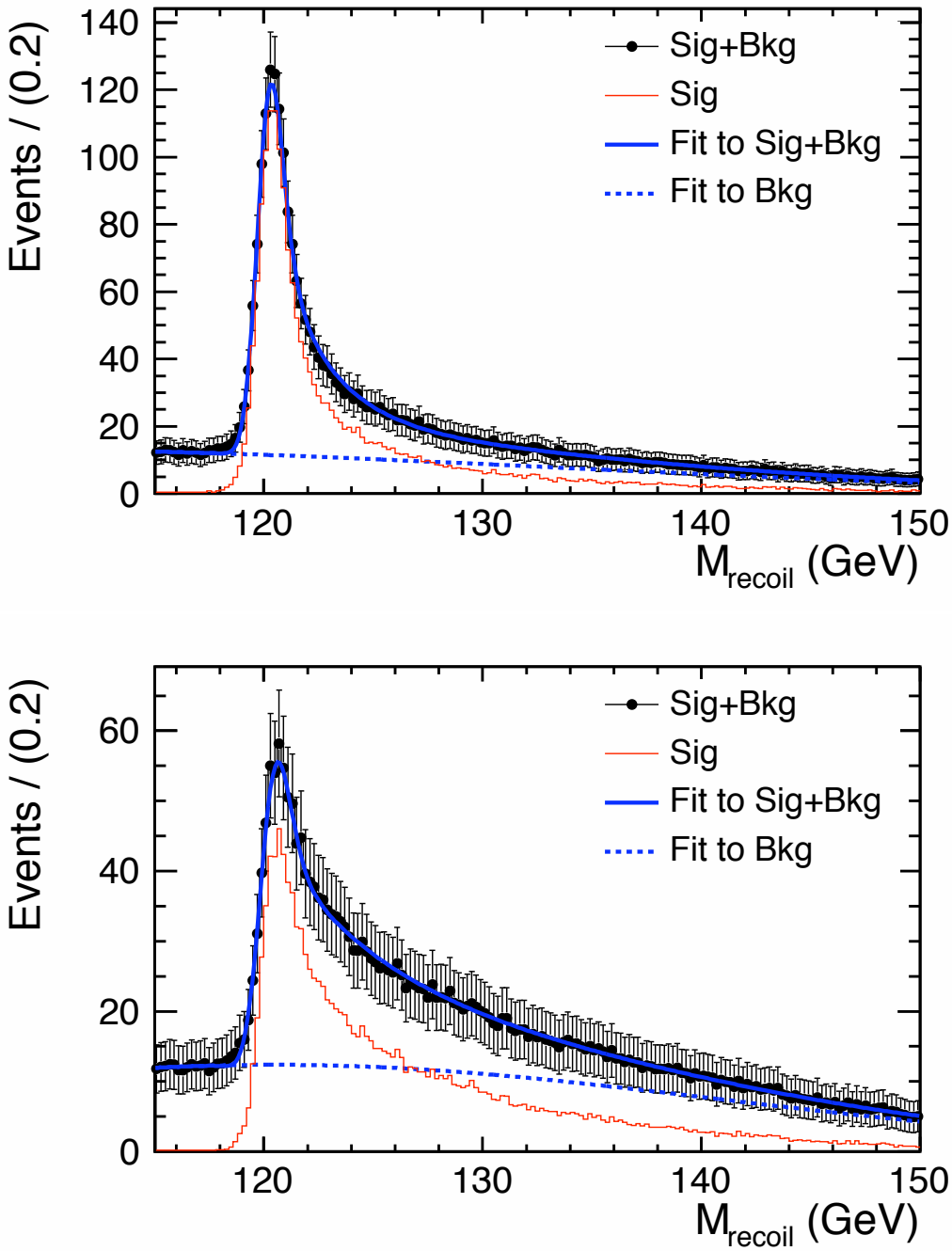

Figure D.11: Fit to the signal plus background using *Physics Motivated Function* of $\mu\mu X$ (top) and eeX (bottom) channels with polarization mode $e^-_L e^+_R$, in MD analysis.

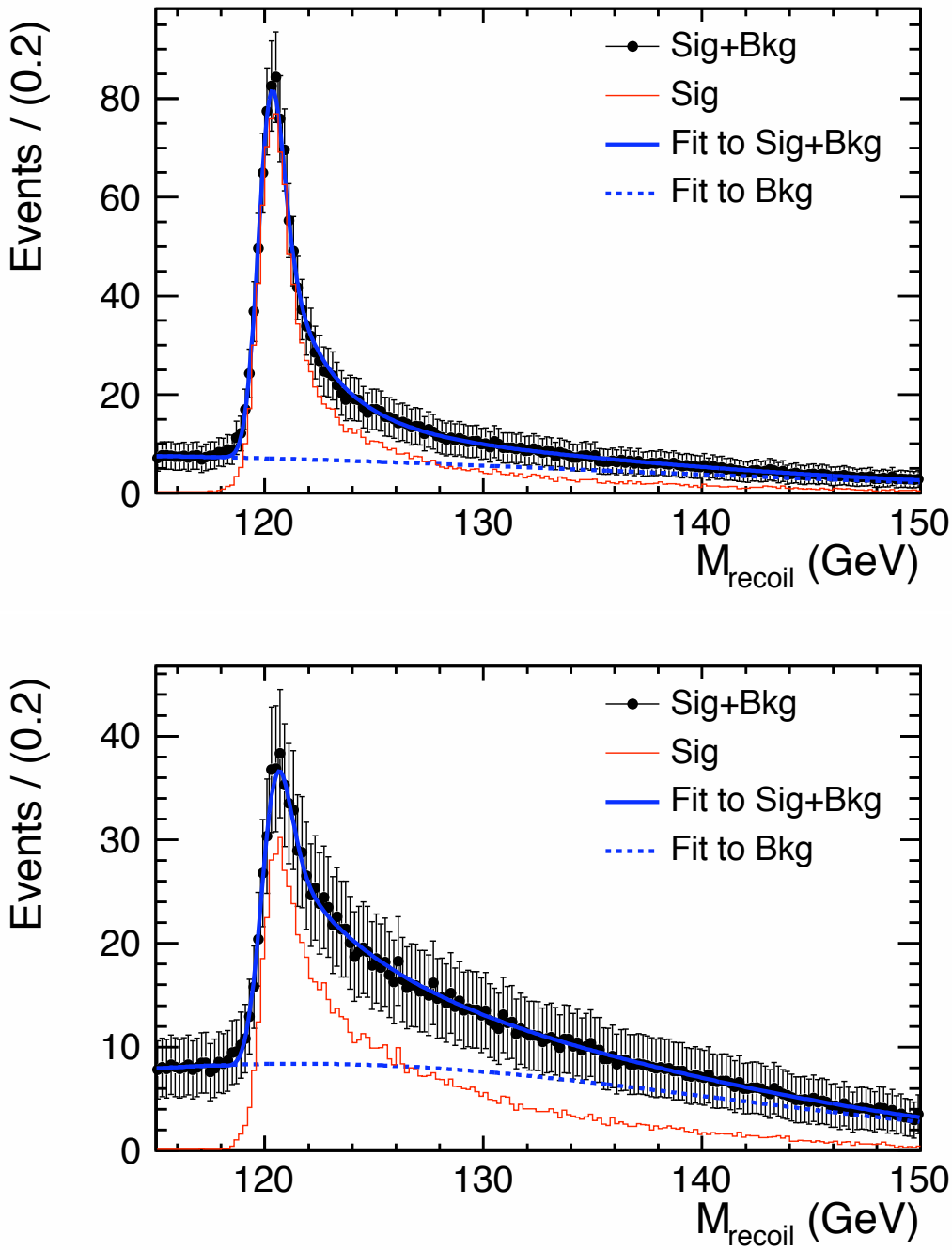

Figure D.12: Fit to the signal plus background using *Physics Motivated Function* of $\mu\mu X$ (top) and eeX (bottom) channels with polarization mode $e^-_R e^+_L$, in MD analysis.

Bibliography

[1] A. Djouadi, *The Anatomy of Electroweak Sysmmetry Breaking, Tome I: The Higgs Boson in The Standard Model*, Physics Reports 457 (2008) 1-216, Elsevier

[2] F. Halzen and A. Martin, *Quarks and Leptons: An Introductory Course in Modern Particle Physics*, John Wiley & Sons (1984)

[3] M. Peskin and D. Schroeder, *An Introduction to Quantum Field Theory*, Addison-Wesley (1995)

[4] C. Quigg, *Gauge Theories of The Strong, Weak, and Electromagnetic Interactions*, Westview (1997)

[5] Particle Data Group, *Review of Particle Physics*, Physics Letters **B667**, 1 (2008)

[6] R. Wigmans, *Calorimetry – Energy Measurement in Particle Physics*, Clarendon Press, Oxford (2000)

[7] R. Barate *et al.*, LEP WG for Higgs boson searches, Phys. Lett. **B565**, 61 (2003)

[8] Tevatron New Phenomena, Higgs Working Group, FERMILAB-PUB-09-060-E, CDF-NOTE-9713, DØ-NOTE-5889, arXiv:0903.4001 (2009)

[9] The LEP collaborations and the LEP electroweak working group (http://lepewwg.web.cern.ch/), CERN-PH-EP/2008-020, arXiv:0811.4682, (2008)

[10] J. Ellis, J.R. Espinosa, G.F. Giudice, A. Hoecker, A. Riotto, CERN-PH-TH/2009-058, arXiv:0906.0954 (2009)

[11] F. Richard and P. Bambade, CARE/ELAN Document-2007-001 (2007)

[12] A. Djouadi, *The Anatomy of Electroweak Sysmmetry Breaking, Tome II: The Higgs Boson in The Minimal Supersymmetric Model*, Physics Reports 459 (2008) 1-241, Elsevier

[13] S. Schael *et al.,* LEP Collaborations, Eur. Phys. J. C **47** 547 (2006)

[14] A. Djouadi, U. Ellwanger and A.M. Teixeira, JHEP **04** 031 (2009)

[15] C.G. Giudice, C. Grojean, A. Pomarol, R. Rattazzi, CERN-PH-TH/2007-47, JHEP 0706:045 (2007)

[16] J-C. Brient, LC-PHSM-2000-049 (2000)

[17] P. Garcia-Abia, W. Lohmann, A. Raspereza, LC-PHSM-2000-062 (2000)

[18] P. Garcia-Abia, W. Lohmann, Eur. Phys. J. direct C2:2 (2000)

[19] M. Ohlerich, W. Lohmann, A. Raspereza, A. Schälicke, LCWS07 Proc. Vol. 1, p. 159-165 (2007)

[20] M. Ruan, Y. Gao, F. Richard, Z. Zhang, ELAN Document-2008-010 (2008)

[21] H. Li, F. Richard, R. Pöschl, Z. Zhang, LCWS08 Proceeding, (2008), arXiv:0901.4893

[22] International Linear Collider, http://www.linearcollider.org/ (2009)

[23] Large Hadron Collider, http://lhc.web.cern.ch/ (2009)

[24] ILC Reference Design Report (2007)

[25] M. Davier, *et. al.,* International Detector Advisory Group, http://www.linearcollider.org/cms/?pid=1000471

[26] International Large Detector concept, http://www.ilcild.org/ , (2009)

[27] Silicon Detector concept, http://www.silicondetector.org/ , (2009)

[28] *Silicon Detector Letter of Intent*, http://silicondetector.org/display/SiD/LOI , (2009)

[29] *ILD Letter of Intent*, http://www.ilcild.org/documents/ild-letter-of-intent , (2009)

[30] The CALICE collaboration, https://twiki.cern.ch/twiki/bin/view/CALICE/WebHome

[31] M.A. Thomson, *PandoraPFA: A particle flow algorithm for the ILC*, CU-HEP-09/11, (2009), arXiv:0907.3577

[32] The CALICE collaboration, J. Repond *et al*, JINST **3** P08001 (2008)

[33] The CALICE collaboration, D. Boumediene *et al*, J. Phys.: Conf. Ser. **160** 012065 (2009)

[34] M. F. Giannelli, PhD. Thesis, Royal Holloway University of London, (2008)

[35] P. Dauncey, private communication.

[36] W. Kilian, T. Ohl, and J. Reuter, *The WHIZARD Event Generator*, http://whizard.event-generator.org/ , (2009)

[37] D. Schulte, GUINEA-PIG, *an e^+e^- beam beam simulation program*, developed in Ph.D. Thesis, University of Hamburg, (1996)

[38] M. Bttaglia *et al.,* arXiv:hep-ex/060310 (2006)

[39] M. Berggren, Beam Spectrum Weighter: A dedicated algorithm for beam spectrum correction in Marlin Framework., (2009)

[40] P. Moras de Freitas, *MOKKA: A detailed Geant4 simulation for the International Linear Collider detectors*, http://mokka.in2p3.fr/ , LC-TOOL-2003-010, (2003)

[41] The GEANT4 Collaboration, http://www.geant4.org/ , NIM **A** 506 (2003) 250-303

[42] O. Wendt, F. Gaed, T. Krämer, Marlin: Modular Analysis and Reconstruction for the LINear collider, LC-DET-2007-001, (2007)

[43] A. Raspereza, X. Chen, A. Frey, *LDC Tracking Package*, proceedings for LCWS/ILC 2007, (2007)

[44] ILC Software, http://ilcsoft.desy.de/, (2009)

[45] K. S. Cranmer, *Kernel estimation in High-energy physics*, Comput. Phys. Commun. **136** (2001) 198, hep-ph/0005309

[46] K. S. Cranmer, *Kernel Estimation for Parametrization of Discriminant Variable Distributions*, ALEPH 99-144, PHYSIC 99-05 (1999)

[47] The OPAL Collaboration, *Search for Neutral Higgs Bosons in e^+e^- Collisions at $\sqrt{s} \approx$ 192–202 GeV*, OPAL PHYSICS NOTE PN426 (2000)

[48] M.A. Thomson, private communication.

[49] Y. Yokoya and P. Chen, Frontiers of Particle Beams: Intensity imitations, Springer-Verlag, (1992)

[50] P. Chen, Phys. Rev. D **46**, 1186 (1992)

[51] P. Chen, T.L. Barklow and M.E. Peskin, Phys. Rev. D **49**, 3209 (1994)

[52] M.E. Peskin, SLAC-TN-04-032, LCC-0010 (1999)

[53] F.A. Berends, R. Kleiss and S. Jadach, Nucl. Phys. **B202** (1982) 63; Computer Physics Commun. **29** (1983) 185

[54] F. Richard, Private Communication.

[55] M.A. Thomson, *ZFinder: A Marlin processor for Bremsstrahlung recovery.*, (2009)

[56] T.L. Barklow, K. Ito, private communication.

Acknowledgements

First of all, I would like to thank my supervisor R. Pöschl. Thanks to him providing me the scholarship supporting my three years of PhD studies. I greatly appreciate his supports and helps for my daily and academic life, especially the important discussion and supervision concerning all my studies during the three years, and his serious corrections for this thesis.

I would like to give my great acknowledgements to F. Richard, for his guidance and supervision during the three years, especially for the Higgs recoil mass study of the *ILD Letter of Intent*, his close directions made the work to be finished in such a condensed time without loss of conscientious and depth. Working together with him, I learned many valuable tactics of independent scientific research, which are the essence of his scientific experiences. Also thanks to him for the daily discussions during lunch and coffee, which expended my knowledge in various fields.

Thanks to all my colleagues at LAL who have ever worked with me for their helps and supports of my studies. In particular I would like to thank: Z. Zhang for the various precious advises in my researches and daily life; M. F. Giannelli for the valuable discussions and corrections of this thesis; P. Bambade, C. Rimbault, and J. Brossard for their helps in accelerator physics; and O. Dadoun and P. Doublet for their helps in daily life and discussions in physics.

I am grateful for all the people who contributed to this work for their supports, ideas, suggestions, and valuable discussions. Special thanks to: M. Thomson from Cambridge University for his Bremsstrahlung recovery, his encouragements in my works and refereeing of this thesis; J. List, M. Berggren, F. Gaede, and S. Aplin from DESY for the beam spectrum re-weighting algorithm, the software developments and the intense MC production efforts at ILD, and their precious supports; A. Miyamoto from KEK for his essential helps on the MC production; K. Ito, Y. Takubo and H. Yamamoto from Tohoku University for their support of the Higgs recoil mass analysis; M. Reinhard from LLR for his precious helps and supports on the calibration work of the SiW ECAL; and T. Barklow from SLAC for his great contribution to the event generation for the LOIs, and thanks to all

Finally, I would like to express my special thanks to my beloved wife Xiaoying, whose strong support to my scientific career and great contribution to my little family are indispensable to this thesis.

List of Figures

2.1 The potential V of the scalar field Φ in the cases of $\mu^2 > 0$ (left) and $\mu^2 < 0$ (right)[1]. 6

2.2 Left: The $\Delta\chi^2$ of the fit to the electroweak precision data as a function of M_H, with excluded ranges by direct searches[9]. Right: Theoretical upper and lower bounds on M_H from the assumption that Standard Model is valid up to the cut-off scale Λ[10]. 9

2.3 The branching ratios (left) and the total decay width (right) of SM Higgs boson as a function of its mass[1]. 10

2.4 Feynman diagram of Higgs-strahlung process. 10

2.5 Cross-setion (σ) of Higgs-strahlung process, as a function of center of mass energy ($\sqrt{s}$) (left) and as a function of Higgs mass (M_H) (right). 11

2.6 Angular distribution of Higgs-strahlung as a function of $cos\theta$ for M_H = 120 GeV. 12

2.7 Normalized Higgs recoil mass distributions of M_H = 120 GeV at $\sqrt{s}$ = 250 GeV with $Z \to \mu^+\mu^-$ and e^+e^-. 15

3.1 Schematic layout of the ILC complex for 500 GeV center of mass energy[24]. 20

3.2 Differential beam energy spectra at IP simulated using GUINEA-PIG with IP parameters of Nom.250. 21

3.3 View of the ILD detector concept[29]. 23

3.4 Left: Average number of hits for simulated charged particle tracks as a function of polar angle[29]. Right: Average total radiation length of the material in the tracking detectors as a function of polar angle[29]. 25

3.5 Left: Transverse momentum resolution for muons plotted versus polar angle for four different simulated muon momenta. The lines show $\sigma_{1/p_T} = 2 \times 10^{-5} \oplus 1 \times 10^{-3}/(p_T \sin\theta)$ for $\theta = 30°$ (green) and $\theta = 85°$ (blue)[29]. Right: Impact parameter resolution for muons versus polar angle for four different simulated muon momenta[29]. 26

3.6 Tracking Efficiency as a function for $t\bar{t} \rightarrow 6$ jets at 500GeV plotted against momentum (left) and $\cos\theta$ (right). Efficiencies are plotted with respect to MC tracks which leave at least 4 hits in the tracking detectors including decays and V^0s[29]. 27

3.7 $\Delta P/P^2$ as a function of track momentum of muon (top) and electron (bottom) candidates decayed from Z of Higgs-strahlung process, in the barrel region of the ILD. 28

3.8 Distributions of the fraction of Bremsstrahlung energy loss for electrons and muons before entering TPC, using the Higgs-strahlung samples with $Z \rightarrow \mathrm{e}^+\mathrm{e}^-$ and $Z \rightarrow \mu^+\mu^-$, respectively. 29

3.9 Distributions of the ratio between reconstructed momentum and Monte-Carlo truth for electrons and muons, using the Higgs-strahlung samples with $Z \rightarrow \mathrm{e}^+\mathrm{e}^-$ and $Z \rightarrow \mu^+\mu^-$, respectively. 29

3.10 Vertices of Bremsstrahlung photons. The accumulation of vertices corresponds to the passive material of detector components as labeled. Figure is drawn using the Higgs-strahlung sample with $Z \rightarrow \mathrm{e}^+\mathrm{e}^-$. 30

3.11 Mean Bremsstrahlung energy loss as a function of the Bremsstrahlung photon vertex in the barrel region of the ILD detector, for electrons in the Higgs-strahlung sample with $Z \rightarrow \mathrm{e}^+\mathrm{e}^-$. The vertices correspond to the positions of the detector components as labeled, with the mean energy loss proportional to the amount of material. 31

4.1 Left: Schematic view of the SiW prototype. Right: Schematic diagram showing the components of a detector slab[32]. 34

4.2 Left: Details of the matrix dimensions in a module (wafer). Right: Details of passive area and layer offsets. Offsets are indicated by single-headed arrows. All distances are in mm[32]. 34

4.3 Picture of the very from end PCB, and description of its elements[32]. . 36

4.4 Distribution and Gaussian fit of E_{rec} for 20 GeV electrons, together with that of the Monte Carlo simulation. The range of the fit is $[-\sigma, +2\sigma]$[33]. 38

4.5 Energy responses of the prototype as a function of the beam energy[33]. 38

4.6 The linearity of the response, $(E_{meas} - E_{mean})/E_{meas}$, as a function of the beam energy[33]. 39

4.7 Relative energy resolution $\delta(E_{meas})/E_{meas}$ as a function of $1/\sqrt{E_{beam}}$, and the fit with parameterization $s/\sqrt{E} \oplus c$[33]. 40

4.8 Position and angular resolutions as a function of beam energy of DESY beam test data at low energies. The data are shown as points with error bars, while the Monte Carlo simulations are shown by the continuous lines[33]. 41

4.9 Position and angular resolutions as a function of beam energy of CERN beam test data at high energies. The data are shown as points with error bars, with resolution along x axis in blue, and y axis in red[34]. 41

4.10 Left: Longitudinal shower profile for the data (points) and Monte Carlo simulation (histogram)[33]. Right: Evolution of the shower maximum as a function of the beam energy[33]. 42

4.11 Radii for 90% and 95% containment of electrons as a function of the beam energy, with center slabs employed only[33]. 43

5.1 Mean energy loss rate as a function of the momenta of muon, pion and proton in liquid (bubble chamber) hydrogen, gaseous helium, carbon, aluminum, iron, tin, and lead[5]. 45

5.2 Beam line setup of the beam test at FNAL in 2008. The Čerenkov detector in the up stream, which is not drawn in this figure. All distances and dimensions are in mm. 45

5.3 Left: Residual pedestal as a function of the pad index (defined in Equation 5.1) for the muon calibration data. Right: Distribution of residual pedestal with each entry representing a pad, with a mean of -0.058 ± 0.003 ADC counts and a RMS of 0.281 ± 0.002 ADC counts. 46

5.4 Left: Pedestal noise as a function of the pad index (defined in Equation 5.1) for the muon calibration data. Right: Distribution of pedestal noise with each entry representing a pad, with a mean of 5.930 ± 0.003 ADC counts and a RMS of 0.330 ± 0.002 ADC counts. 46

5.5 Distribution of number of hits for each pad, each entry represents a pad. 47

5.6 A typical fitting of the hit energy distribution of a pad to extract the calibration constant. The fit function is a convolution of Landau with Gaussian. The resulting calibration constant for this particular pad is 46.57 ± 0.04 ADC counts given by the Landau MPV, while the signal induced noise is 7.26 ± 0.73 ADC counts given by the Gaussian sigma. . 48

5.7 Left: Distribution of the statistical error of fitted Landau MPV for each pad, with a mean of 0.516 ± 0.002 ADC counts and a RMS of 0.173 ± 0.001 ADC counts. Right: Distribution of χ^2/Ndf for each pad of the fit to the hit energy spectrum, with a mean of 1.139 ± 0.004, with a RMS of 0.394 ± 0.003. 48

5.8 Map of the dead pads of all the 30 layers. Layer numbering is starting from left to right and then from top to bottom. Dead pads are marked by color. 49

5.9 Left: Distribution of Landau MPV (calibration constant) with each entry representing a pad, with a mean of 47.61 ± 0.02 ADC counts and a RMS of 2.06 ± 0.01 ADC counts. Right: Distribution of signal induced noise with each entry representing a pad, with a mean of 7.22 ± 0.01 ADC counts and a RMS of 1.00 ± 0.01 ADC counts. 50

5.10 Analogue signal curve obtained by the chip scan for the VFE of the ECAL prototype[35]. The hold value, the time of trigger arrival and signal read out are labeled for illustration. 52

5.11 Differences of the calibration constants for each pad, between that obtained from muons with 20×20 trigger and from pions with 10×10&Čerenkov, with a mean of 0.97 ± 0.02 ADC counts and a RMS of 1.19 ± 0.02 ADC counts. 53

5.12 Landau MPV (calibration constants) with errors as a function of pad index (defined in Equation 5.1). 54

5.13 Correlation of calibration constants obtained from August (left plot) and October (right plot) 2006 CERN muon runs with those obtained from 2008 FNAL muon runs. A correlation coefficient of 80.30% is found when comparing with August 2006 CERN, while 83.76% is found when comparing with October 2006 CERN. 54

5.14 Left: Difference of the calibration constants between August 2006 CERN runs and 2008 FNAL runs as a function of pad index (defined in Equation 5.2). Right: Distribution of the difference of each pad, with a mean of 0.67 ± 0.02 ADC counts and a RMS of 1.21 ± 0.01 ADC counts. 55

5.15 Left: Difference of the calibration constants between October 2006 CERN runs and 2008 FNAL runs as a function of pad index (defined in Equation 5.2). Right: Distribution of the difference of each pad, with a mean of 1.42 ± 0.01 ADC counts and a RMS of 1.08 ± 0.01 ADC counts. . . . 55

6.1 Distributions of the variables for Lepton-ID of lepton candidates and other particles with $P > 15\,\mathrm{GeV}$. 61

6.2 2D $\Delta P/P^2$ distribution vs. $cos\theta$ (left) and $\Delta P/P^2$ distribution vs. track momentum (right) of muon candidates decayed from Z^0 of Higgs-strahlung process. 62

6.3 2D $\Delta P/P^2$ distribution vs. $cos\theta$ (left) and $\Delta P/P^2$ distribution vs. track momentum (right) of electron candidates decayed from Z^0 of Higgs-strahlung process. 63

6.4 P_{Tdl} distributions of $\mu\mu X$ (left) and eeX (right), and of their corresponding backgrounds. 65

6.5 $\cos\theta_{dl}$ distributions of $\mu\mu X$ (left) and eeX (right), and of their corresponding backgrounds. 66

6.6 *acol* distributions of $\mu\mu X$ (left) and eeX (right), and of their corresponding backgrounds. 68

6.7 *acop* distributions of $\mu\mu X$ (left) and eeX (right), and of their corresponding backgrounds. 69

6.8 M_{dl} distributions of $\mu\mu X$ (top) and eeX (bottom), and of their corresponding backgrounds. 70

6.9 M_{recoil} distributions of $\mu\mu X$ (top) and eeX (bottom), and of their corresponding backgrounds. 71

6.10 Correlation between P_{Tdl} and $P_{T\gamma}$ for the $\mu\mu$ process (top) and for the Higgs-strahlung $\mu\mu X$ process (bottom). 72

6.11 $\Delta P_{Tbal.}$ distributions of Higgs-strahlung and $\mu\mu/ee$ backgrounds for the $\mu\mu X$-channel (top) and eeX-channel (bottom). 73

6.12 $N_{add.TK}$ distributions for signal and background in the $\mu\mu X$-channel. . 74

6.13 $N_{add.TK}$ distributions for signal and background in the eeX-channel. . . 75

6.14 $|\Delta\theta_{2tk}|$ distributions of Higgs-strahlung and $\mu\mu/ee$ backgrounds for the $\mu\mu X$-channel (top) and eeX-channel (bottom). 76

6.15 $|\Delta\theta_{min}|$ distributions of Higgs-strahlung and $\mu\mu/ee$ backgrounds for the $\mu\mu X$-channel (top) and eeX-channel (bottom). 77

6.16 $|\cos\theta_{missing}|$ distributions of $\mu\mu X$ (top) and eeX (bottom), and of their corresponding backgrounds. 79

6.17 The distributions of the Likelihood Fraction f_L (left), the number of remaining events versus the cut on f_L (middle), and the significance versus f_L cuts (right). The distributions are shown for the $\mu\mu X$-channel with polarization mode $e^-_L e^+_R$ in the MI Analysis. 82

6.18 Recoil mass distributions after background rejection, of signal, background, and signal plus background. Illustration using MI analysis, $\mu\mu X$ channel with polarization mode $e^-_L e^+_R$. 84

6.19 Fit to pure signal *after background rejection* using GPET formula. Illustration using MI analysis, $\mu\mu X$ channel with polarization mode $e^-_L e^+_R$. . 85

6.20 M_{recoil} distribution of Signal *before and after background rejection.* Maximum of the distributions are normalized to be *one.* Illustration using MI analysis, $\mu\mu X$ channel with polarization mode $e^-_L e^+_R$. 86

6.21 Fit to pure signal *after background rejection* using *Corrected GPET formula.* Illustration using MI analysis, $\mu\mu X$ channel with polarization mode $e^-_L e^+_R$. 86

6.22 Fit to the signal plus background using *GPET Function* of $\mu\mu X$ (top) and eeX (bottom) channels with polarization mode $e^-_L e^+_R$ in MD analysis. 87

6.23 Fit to pure signal *after background rejection* using *Kernel Estimation.* Illustration using MI analysis, $\mu\mu X$ channel with polarization mode $e^-_L e^+_R$. 89

6.24 Fit to the signal plus background using *Kernel Estimation* of $\mu\mu X$ (top) and eeX (bottom) channels of polarization mode $e^-_L e^+_R$, in MD analysis. 90

6.25 Fit to pure signal *after background rejection* using *Corrected Physics Motivated Function.* Illustration using MI analysis, $\mu\mu X$ channel with polarization mode $e^-_L e^+_R$. 92

6.26 Fit to the signal plus background using *Physics Motivated Function* of $\mu\mu X$ (top) and eeX (bottom) channels of polarization mode $e^-_L e^+_R$, in MD analysis. 93

6.27 The Higgs recoil mass distribution in the $\mu\mu X$- channel (top) and eeX-channel (bottom), comparison of that in generator level and after detector simulation. 97

6.28 Distribution of Higgs recoil mass resolution *solely due to the uncertainty of detector response*, obtained by propagating the momenta matrices of lepton tracks to the recoil mass. Taking the $\mu\mu X$-channel for illustration, the maximum is at around 230 MeV, while the mean is about 330 MeV. 98

6.29 Comparison of the Higgs recoil mass distributions of eeX channel with and without the Bremsstrahlung recovery. 99

6.30 Fit to the signal plus background using *Kernel Estimation* for eeX-channel with polarization mode $e^-_L e^+_R$ in MI analysis, with Bremsstrahlung recovery. 100

6.31 Fit to the signal plus background using *Kernel Estimation* for eeX-channel with polarization mode $e^-_R e^+_L$ in MI analysis, with Bremsstrahlung recovery. 101

6.32 Fit to the signal plus background using *Kernel Estimation* for eeX-channel with polarization mode $e^-_L e^+_R$ in MD analysis, with Bremsstrahlung recovery. 101

6.33 Fit to the signal plus background using *Kernel Estimation* for eeX-channel with polarization mode $e^-_R e^+_L$ in MD analysis, with Bremsstrahlung recovery. 101

6.34 Fit of the *Invariant Mass* of the $Z \to \mu^+\mu^-$ in the ZZ process using *Kernel Estimation*, with polarization mode $e^-_L e^+_R$. An accuracy of 13 MeV is obtained for the invariant mass measurement. 103

6.35 Fit of the *Recoil Mass* to the $Z \to \mu^+\mu^-$ in the ZZ process using *Kernel Estimation*, with polarization mode $e^-_L e^+_R$. An accuracy of 28 MeV is obtained for the Z recoil mass measurement. 104

A.1 The distributions of the Likelihood Fraction f_L (left), the number of remaining events versus the cut on f_L (middle), and the significance versus f_L cuts (right). The distributions are shown for the $\mu\mu X$-channel with polarization mode $e^-_L e^+_R$ in the MI Analysis. 109

A.2 Same as Figure A.1, but for the eeX-channel with polarization mode $e^-_L e^+_R$ in the MI Analysis. 110

A.3 Same as Figure A.1, but for the $\mu\mu X$-channel with polarization mode $e^-_R e^+_L$ in the MI Analysis. 110

A.4 Same as Figure A.1, but for the eeX-channel with polarization mode $e^-_R e^+_L$ in the MI Analysis. 110

A.5 Same as Figure A.1, but for the $\mu\mu X$-channel with polarization mode $e_L^- e_R^+$ in the MD Analysis. 111

A.6 Same as Figure A.1, but for the eeX-channel with polarization mode $e_L^- e_R^+$ in the MD Analysis. 111

A.7 Same as Figure A.1, but for the $\mu\mu X$-channel with polarization mode $e_R^- e_L^+$ in the MD Analysis. 111

A.8 Same as Figure A.1, but for the eeX-channel with polarization mode $e_R^- e_L^+$ in the MD Analysis. 112

C.1 Comparison of $F(x)$ with the higgs recoil mass distribution using Monte Carlo event generation. 124

D.1 Fit to the signal plus background using *GPET Function* of $\mu\mu X$ (top) and eeX (bottom) channels with polarization mode $e_L^- e_R^+$, in MI analysis. 126

D.2 Fit to the signal plus background using *GPET Function* of $\mu\mu X$ (top) and eeX (bottom) channels with polarization mode $e_R^- e_L^+$, in MI analysis. 127

D.3 Fit to the signal plus background using *GPET Function* of $\mu\mu X$ (top) and eeX (bottom) channels with polarization mode $e_L^- e_R^+$, in MD analysis. 128

D.4 Fit to the signal plus background using *GPET Function* of $\mu\mu X$ (top) and eeX (bottom) channels with polarization mode $e_R^- e_L^+$, in MD analysis. 129

D.5 Fit to the signal plus background using *Kernel Estimation* of $\mu\mu X$ (top) and eeX (bottom) channels with polarization mode $e_L^- e_R^+$, in MI analysis. 130

D.6 Fit to the signal plus background using *Kernel Estimation* of $\mu\mu X$ (top) and eeX (bottom) channels with polarization mode $e_R^- e_L^+$, in MI analysis. 131

D.7 Fit to the signal plus background using *Kernel Estimation* of $\mu\mu X$ (top) and eeX (bottom) channels with polarization mode $e_L^- e_R^+$, in MD analysis. 132

D.8 Fit to the signal plus background using *Kernel Estimation* of $\mu\mu X$ (top) and eeX (bottom) channels with polarization mode $e_R^- e_L^+$, in MD analysis. 133

D.9 Fit to the signal plus background using *Physics Motivated Function* of $\mu\mu X$ (top) and eeX (bottom) channels with polarization mode $e_L^- e_R^+$, in MI analysis. 134

D.10 Fit to the signal plus background using *Physics Motivated Function* of $\mu\mu X$ (top) and eeX (bottom) channels with polarization mode $e_R^- e_L^+$, in MI analysis. 135

D.11 Fit to the signal plus background using *Physics Motivated Function* of $\mu\mu X$ (top) and eeX (bottom) channels with polarization mode $e_L^- e_R^+$, in MD analysis. 136

D.12 Fit to the signal plus background using *Physics Motivated Function* of $\mu\mu X$ (top) and eeX (bottom) channels with polarization mode $e_R^- e_L^+$, in MD analysis. 137

List of Tables

3.1 Global accelerator parameters for 500 GeV center of mass energy[24]. . . 21

3.2 Beam parameters at interaction point (IP)[24]. 22

3.3 Parameters of the ILD baseline detector concept. Unless otherwise specified, values are shown in units of mm[29]. 24

3.4 Transverse passive material budget of the ILD baseline design. 30

6.1 Processes and cross sections for polarization mode $e^-_L e^+_R$. The signal is indicated by bold face letters; the cross section in the parentheses of e^+e^- and $\mu^+\mu^-$ are that after Pre-Cuts, see Table 6.3 for the Pre-Cuts definition. 58

6.2 Processes and cross sections for polarization mode $e^-_R e^+_L$. The signal is indicated by bold face letters; the cross section in the parentheses of e^+e^- and $\mu^+\mu^-$ are that after Pre-Cuts, see Table 6.3 for the Pre-Cuts definition. 59

6.3 Pre-Cuts for $e^+e^- \to e^+e^-$ and $e^+e^- \to \mu^+\mu^-$ production. 60

6.4 Variables and cut values for the Lepton-ID. 60

6.5 Lepton-ID Efficiency and Purity for reconstructed particles with $P > 15\,\mathrm{GeV}$, where *Efficiency* and *Purity* are defined in Equation 6.2. 62

6.6 Model Independent (MI) and Model Dependent (MD) Cut-Chain. The *Tightened Pre-Cuts* are listed in Table 6.7, and the Likelihood further rejection is introduced in Section 6.4.3. 80

6.7 Tightened Pre-Cuts for all the reactions. 80

6.8 Resulting number of signal (S) and background (B), and the efficiency of signal selection (in the parentheses) after *Cut-Based* background rejection. 80

6.9 The background processes of which the PDFs are employed in the Likelihood calculation, for different analysis channels. 82

6.10 The final number of signal (S) and number of background (B) after background rejection, and the corresponding efficiencies of signal selection (in the parentheses). 83

6.11 Resulting Higgs mass M_H and cross section σ of the *MI Analysis* using *GPET Function*. 94

6.12 Resulting Higgs mass M_H and cross section σ of the *MD Analysis* using *GPET Function*. 95

6.13 Resulting Higgs mass M_H and cross section σ of the *MI Analysis* using *Kernel Estimation*. 95

6.14 Resulting Higgs mass M_H and cross section σ of the *MD Analysis* using *Kernel Estimation*. 95

6.15 Resulting Higgs mass M_H and cross section σ of the *MI Analysis* using *Physics Motivated Function*. 95

6.16 Resulting Higgs mass M_H and cross section σ of the *MD Analysis* using *Physics Motivated Function*. 96

6.17 Resulting Number of Signal (S) and Number of Background (B), and the efficiencies of signal selection (in the parentheses) after background rejection, for eeX-channel with Bremsstrahlung recovery 100

6.18 Resulting Higgs mass M_H and cross section σ for the MI Analysis and MD Analysis in the eeX-channel with Bremsstrahlung recovery. 100

6.19 Resulting Higgs mass M_H and cross section σ by merging $\mu\mu X$-channel and eeX-channel with Bremsstrahlung recovery, for the MI Analysis and MD Analysis. 100

B.1 Number of events remaining after each cut for the $\mu\mu X$-channel with polarization mode $e^-_L e^+_R$ in the MI analysis. Efficiencies of signal selection are given inside parentheses. 113

B.2 Number of events remaining after each cut for the eeX-channel with polarization mode $e^-_L e^+_R$ in the MI analysis. Efficiencies of signal selection are given inside parentheses. 114

B.3 Number of events remaining after each cut for the $\mu\mu X$-channel with polarization mode $e^-_R e^+_L$ in the MI analysis. Efficiencies of signal selection are given inside parentheses. 114

B.4 Number of events remaining after each cut for the eeX-channel with polarization mode $e^-_R e^+_L$ in the MI analysis. Efficiencies of signal selection are given inside parentheses. 115

B.5 Number of events remaining after each cut for the $\mu\mu X$-channel with polarization mode $e^-_L e^+_R$ in the MD analysis. Efficiencies of signal selection are given inside parentheses. 115

B.6 Number of events remaining after each cut for the eeX-channel with polarization mode $e^-_L e^+_R$ in the MD analysis. Efficiencies of signal selection are given inside parentheses. 116

B.7 Number of events remaining after each cut for the $\mu\mu X$-channel with polarization mode $e^-_R e^+_L$ in the MD analysis. Efficiencies of signal selection are given inside parentheses. 116

B.8 Number of events remaining after each cut for the eeX-channel with polarization mode $e^-_R e^+_L$ in the MD analysis. Efficiencies of signal selection are given inside parentheses. 117